DESIGN, MODELING, AND TESTING OF A HYBRID SOLAR/AUTOTHERMAL STEAM GASIFICATION PROCESS

A Dissertation
Presented to
The Academic Faculty

by

Alexander P. Muroyama

In Partial Fulfillment
of the Requirements for the Degree
Doctor of Philosophy in the
G. W. Woodruff School of Mechanical Engineering

Georgia Institute of Technology
August 2017

DESIGN, MODELING, AND TESTING OF A HYBRID SOLAR/AUTOTHERMAL STEAM GASIFICATION PROCESS

Approved by:

Dr. Peter Loutzenhiser, Advisor (ME)
G. W. Woodruff School of Mechanical Engineering
Georgia Institute of Technology

Dr. Carsten Sievers (ChBE)
School of Chemical & Biomolecular Engineering
Georgia Institute of Technology

Dr. Sheldon Jeter (ME)
G. W. Woodruff School of Mechanical Engineering
Georgia Institute of Technology

Dr. Alan Weimer (ChBE)
School of Chemical & Biological Engineering
University of Colorado at Boulder

Dr. Devesh Ranjan (ME)
G. W. Woodruff School of Mechanical Engineering
Georgia Institute of Technology

Date Approved: May 3, 2017

ACKNOWLEDGEMENTS

I would like to acknowledge the contributions and support of a number of people, without whom I would not have been able to complete this dissertation. I would first like to thank my advisor, Dr. Peter Loutzenhiser, for his indispensable guidance and support in my research, and for continuously pushing me to become a better researcher. I am also grateful for my committee members: Dr. Sheldon Jeter, Dr. Devesh Ranjan, Dr. Carsten Sievers, and Dr. Alan Weimer, whose inputs have greatly improved this work. I would also like to thank my colleagues: Robby Gill, Evan Bush, Andrew Schrader, and Garrett Schieber. I also thank the international master's students: Iacopo Guschetti, Gianmarco De Dominicis, and Karl-Philipp Schlichting. It has been a challenging and rewarding experience building the Solar Fuels and Technologies Laboratory, and I feel fortunate to have to have worked alongside such motivated and encouraging people. Their inputs and assistance were instrumental in the completion of this work. I thank Tyler Shinn and Dr. Roger Fales for their work on the controls aspects of this research, and my undergraduate research advisor, Dr. Gary Felton, for providing biomass samples. I also thank Jungseob So for performing BET analyses. I am also grateful for the assistance from Colby Jarrett in setting up the TGA, as well as my other friends who have been there for me throughout graduate school. Finally, I would like to thank my parents and my brother, Andrew, for their love and support over all the years, and particularly over the last five years. Their encouragement has really helped me through the inevitable setbacks of research.

This material is based upon work supported by the National Science Foundation Graduate Research Fellowship Program under Grant No. DGE-1650044. Any opinions, findings, and conclusions or recommendations expressed in this material are those of the author and do not necessarily reflect the views of the National Science Foundation.

TABLE OF CONTENTS

LIST OF TABLES

LIST OF FIGURES

LIST OF SYMBOLS AND ABBREVIATIONS

A	area, low frequency error specification
c_p	specific heat
c_0	speed of light in a vacuum
d	disturbance input due to solar irradiation
d_p	particle diameter
D	distance traveled by ray
$\hat{e}$	unit vector
E_a	apparent activation energy
E_b	Planck's total blackbody emissive power
$E_{b\lambda}$	Planck's spectral blackbody emissive power
f	fractional function
F	view factor, generic function of measured properties
g	gravitational constant
h	Planck's constant, height
$\overline{h}$	molar specific enthalpy
H_o	external contribution to irradiation
$I_{b\lambda}$	spectral blackbody intensity
I_{DN}	direct-normal irradiance
k	thermal conductivity, rate constant
k_B	Boltzmann's constant
k_0	apparent pre-exponential factor
K	controller
L^2-*norm*	Euclidean norm
m	mass
M	high frequency error specification
n	molar amount
$\dot{n}$	molar flow rate
p	normalized partial pressure

P	probability density function
q	net radiative flux, measurand
$\dot{Q}$	power (heat)
r	distance (radial), reaction rate
$\vec{r}$	vector to surface
R	cold gas ratio, cumulative distribution function
Re_{mf}	Reynolds number at minimum fluidization
R_{N}	random number from a uniform distribution
R_{u}	universal gas constant
s	Laplace operator
$\hat{s}$	ray direction unit vector
$\overline{s_i s_j}$, $\overline{s_i g_k}$	direct exchange areas
S_{BET}	specific surface area from BET
t	time
$\hat{t}$	unit tangent vector
T	temperature
u	control effort, velocity
$\dot{V}$	volumetric flow rate
V_0	specific pore volume from BET
W	work, control effort weight
$\dot{W}$	power (work)
$W_{\mathrm{i}}\Delta$	uncertainty model
x	distance (Cartesian)
X	carbon conversion
y	mole fraction, distance (Cartesian)
z	weighted control effort, distance (Cartesian)

Greek Symbols

α	conversion
β	fitting parameter
δ_{ij}	Kronecker delta
ε	emissivity
$\varepsilon_{\mathrm{mf}}$	void fraction at minimum fluidization
η	efficiency
θ	zenith angle
θ_{O}	fraction of active sites covered with oxygen
ΔH	enthalpy change of reaction
κ	absorption coefficient
λ	wavelength
λ_{c}	cutoff wavelength
μ	dynamic viscosity
ξ	variable of integration
ρ	density, reflectivity
σ	Stefan-Boltzmann constant, experimental uncertainty
τ	time (transport) delay
υ	surface parameter
ϕ	azimuthal angle
χ^2	estimation
ψ	particle sphericity
ω	frequency

SUMMARY

Transitioning from a fossil-fuel-based energy infrastructure to a fully-renewable energy infrastructure requires intermediate solutions that can bridge the gap between existing practices and more sustainable methods. A novel hybrid solar/autothermal steam gasification process is examined for the purpose of continuously producing H_2- and CO-rich synthesis gas. Such a process would address the problem of intermittency in a solar-only operation while still having the benefit of producing a solar-upgraded fuel product. The resulting synthesis gas could be converted to liquid fuels for the transportation sector via Fischer-Tropsch or other catalytic processes.

This study builds off of previous research into solar-driven gasification that has demonstrated the ability of concentrated sunlight to drive endothermic gasification reactions using coal, coke, biomass, or waste materials. The goal of this study was to model and experimentally prove the concept of hybrid solar/autothermal gasification. To this end, a transient finite-volume model was built to evaluate benefits of hybridization over multiple days of operation, kinetic parameters were determined for gasification and combustion of various feedstocks using thermogravimetric analysis, radiation modeling was performed on a bench-scale reactor, and a prototype fluidized-bed reactor was designed and tested in a high-flux solar simulator under various experimental conditions.

Steam gasification of carbonaceous materials was examined in a transient finite-volume model of a hybrid solar/autothermal steam gasification reactor concept. Equilibrium was assumed for the chemical products based on Gibbs free energy minimization. Direct normal irradiance and temperature data inputs were gathered from

typical meteorological year data for Albuquerque, NM. A dynamic feed-forward control system was implemented, varying O_2 and feedstock levels to maintain reaction zone temperature as well as synthesis gas production rate regardless of solar disturbances. Results were compared between autothermal-only operation and hybrid operation over four days. Evaluated model outputs included cold gas (upgrade) ratios, CO_2 generated, O_2 consumed, and associated power consumption for gas separation.

Kinetic analyses were performed for gasification and combustion reactions of various carbonaceous feedstocks using thermogravimetric analysis. The feedstocks examined were activated charcoal derived from wood, bituminous coal char, and miscanthus char. Langmuir-Hinshelwood type reaction mechanisms were developed for temperature ranges of 550-960 and 1120-1270 K and concentrations of 10–40% O_2–Ar and 20–100% H_2O–CO_2 were evaluated for combustion and gasification, respectively. Carbonaceous feedstock microstructures were examined using scanning electron microscopy. Surface area and porosity were characterized using Brunauer–Emmett–Teller analysis.

Monte Carlo ray tracing was used to analyze potential prototype geometries for use in a high-flux solar simulator. Grid and ray independence studies were performed and heat flux distributions were presented for an opaque tube (fluidized bed) within a blackbody cavity receiver. Parametric studies were performed to examine the effects of aperture shape, tube placement within the cavity, and number and position of lamps. A configuration was selected with the goal of maximizing the capture of radiation without creating strongly localized heat fluxes.

A prototype fluidized-bed hybrid solar/autothermal steam gasification reactor was designed, fabricated, and tested in a high-flux solar simulator. The fluidized bed allowed for continuous operation, with sufficient residence times to allow for high carbon conversions. Four inlet flow conditions were tested at various levels of O_2 and H_2O while keeping total flow rate, lamp power, and feedstock mass flow rate constant. Results were statistically analyzed using analysis of variance, and effects were examined using interaction plots. O_2 level was seen to have significant effects on temperature, H_2:CO ratio, carbon conversion, cold gas ratio, solar-to-fuel efficiency, and CO_2 production, while H_2O level significantly affected H_2:CO ratio, CO_2 production, and, to a lesser degree, cold gas ratio. Implications of the results are discussed, and possible areas for future work are presented.

CHAPTER 1. INTRODUCTION

1.1 Introduction

Growing concerns about climate change in addition to rising worldwide demand for energy have motivated the development of renewable, more environmentally-benign sources of energy. Liquid fuels accounted for 33% of the world's energy consumption in 2012, the largest single source [1]. With continued growth of the transportation sector, particularly in developing countries, fossil-derived liquid fuels will remain a significant source of energy for the coming decades [1]. Meeting this growing demand in a way that mitigates anthropogenic CO_2 emissions will be critical. Solar energy is an abundant renewable resource that can be captured via concentrated solar thermochemical processes, effectively storing sunlight in a transportable, chemical form. Steam gasification of carbonaceous materials to produce H_2- and CO-rich synthesis gas (syngas) is a well-known approach for transforming solid fuels to a more viable fuel for a wider range of more efficient applications (*e.g.*, an integrated gasification combined cycle) [2, 3]. The resulting syngas can be further synthesized into chemicals or liquid fuel needed for the transportation sector via known catalytic processes (*e.g.*, Fischer-Tropsch (F-T) synthesis) [4-6]. Gasification methods include autothermal [7-9] and allothermal [10-15] gasification.

Conventional autothermal gasification has been implemented at scale in a number of places as a method of producing gaseous or liquid fuels from more abundant solid fuels like coal. In an autothermal gasification processes, a portion of the feedstock is partially combusted (oxy-combustion) to provide process heat to drive the reaction. The

resulting syngas often contains contaminates (*e.g.*, NO_x and SO_x) which need to be removed prior to use or synthesis. Contamination is reduced for allothermal gasification as a separate process, typically combustion, provides the process heat for the reaction. However, this is coupled to additional exergy losses associated with the irreversibility of moving the heat to the reaction.

Concentrated solar irradiation is an effective source of high quality process heat for allothermal gasification [13-15] most often deployed using one of two solar thermochemical reactor configurations: 1) direct irradiation with reactants directly exposed to the concentrated solar irradiation that simultaneously function as reactants and radiant absorbers, and 2) indirect irradiation with an emitter plate or opaque tubes absorbing solar irradiation and thermally transporting it to the reactants. While an indirectly-irradiated design avoids issues with window fouling and material failure under pressure, there is an associated loss in efficiency from transporting heat to reactants via conduction. Solar gasification processes do not require O_2, allowing a larger portion of the feedstock to be directly converted to syngas while reducing contaminants (*e.g.*, tars) and reducing CO_2 emissions. Furthermore, part of the solar energy is stored through calorific upgrade of the feedstock material by up to 33%, as indicated by thermodynamic analysis of the gasification products [13].

Few solar gasification studies have addressed the challenge of maintaining operations in spite of solar transients. One of the fundamental hindrances of solar thermochemical processes is the inability to run them at all hours of the day, negatively impacting downstream processes (*e.g.*, F-T synthesis) and overall economic feasibility. Syngas is difficult to store [16], and large changes in reaction rate and product selectivity

have been observed during F-T synthesis start-up. [17] The hybrid solar/autothermal reactor would operate in three general modes, shown in Figure 1.1: 1) solar gasification for periods of abundant solar irradiation, 2) autothermal gasification for nighttime operation, and 3) a combined system during periods of insufficient solar irradiation. While similar hybrid concepts have been evaluated from a systems and techno-economic perspective, to the author's knowledge an experimental evaluation remains absent from literature. Demonstrating the hybrid concept through modeling and small-scale testing lays the groundwork for further exploratory studies into system control and scale-up, with the ultimate goal of more efficiently transforming solid fuels such as biomass and coal into useful, high-energy products.

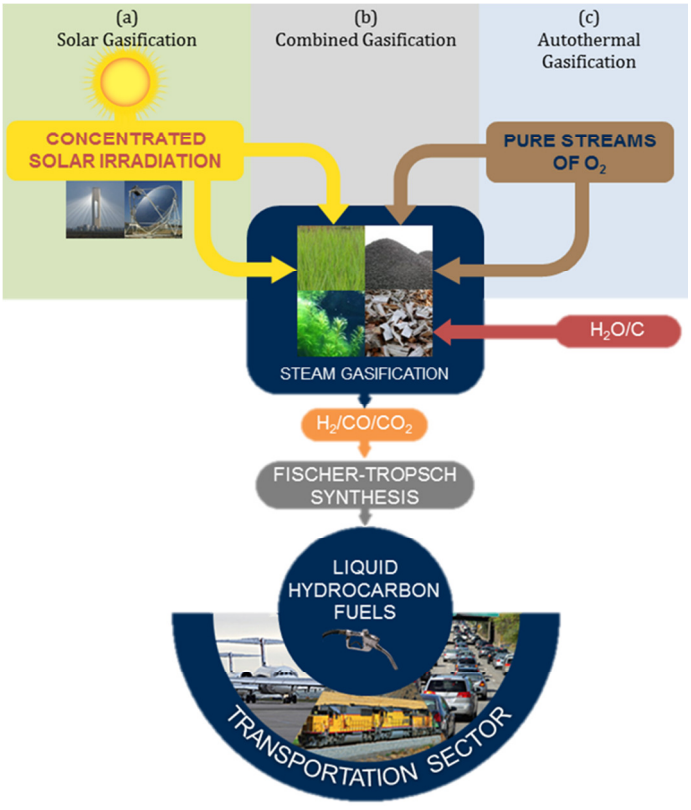

Figure 1.1: Diagram of the hybrid solar/autothermal gasification process concept.

1.2 Research Objectives

This study aims to develop a coupled autothermal and solar gasification process within a hybrid reactor. Such a technology could allow for the continuous production of syngas for further processing to liquid fuels via F-T synthesis while utilizing a renewable resource to upgrade syngas quality. The described research introduces a means of bridging the gap between novel renewable energy technologies and practical application that has been demonstrated using more conventional methods. The guiding hypothesis is that incorporating O_2 flow in the reacting gases will allow for reactor temperature control in response to solar transients and continuous operation. Specific objectives include the following:

1. Develop a simplified heat and mass transfer model to demonstrate controllability and evaluate reactor performance across different times of the day and periods of the year.
2. Perform thermogravimetric analysis of gasification and combustion reaction kinetics for several applicable carbonaceous feedstocks.
3. Model the radiative heat transport in a prototype reactor in order to predict heat fluxes and optimize reactor geometry.
4. Design and prototype a bench-scale reactor to allow for testing in a high-flux solar simulator (HFSS).
5. Experimentally validate the concept by testing the solar/autothermal gasification process under several different inlet conditions.

1.3 Thesis Organization

A combination of modeling and experimental work was performed to achieve the goal of developing the fundamentals of a novel solar/autothermal gasification process concept. Chapter 2 introduces the reactor concept and evaluates its performance through finite-volume modeling. Equilibrium compositions for various reactant mixtures are presented for relevant temperature ranges. The methodology for transient heat and mass transfer modeling is developed for a 5 MW_{th}-scale reactor. A feed-forward control scheme to maintain reaction zone temperature in response to solar disturbances is described. Model results are presented for four days of operation, comparing hybrid operation to a baseline autothermal case using outputs including cold gas (upgrade) ratios, CO_2 emissions, O_2 consumed, and associated power consumption for gas separation.

Chapter 3 presents the kinetic analyses of gasification and combustion reactions for three carbonaceous feedstocks: activated charcoal, bituminous coal char, and miscanthus char. Langmuir-Hinshelwood-type reaction mechanisms were developed, and experimentation was carried out using a thermogravimetric analyzer. Kinetic parameters were fitted using non-linear least squares regression, and error analysis was performed using chi-squared boundaries. In addition, surface characterizations were performed using scanning electron microscopy (SEM) and Brunauer–Emmett–Teller (BET) analysis.

Chapter 4 describes further radiation modeling work on a bench-scale prototype reactor, performed using Monte Carlo ray tracing. For ray tracing purposes, the reactor consisted of a cylindrical tube situated in box with an aperture. The reactor geometry and

materials are specified, as well as the associated radiative surface properties. The ray tracing methodology, as well as ray and grid independence study results are presented. Incident heat flux distributions are provided for a series of lamp configurations, tube positions, and aperture shapes. Modeling results are discussed in terms of optima for a prototype reactor.

Chapter 5 presents the detailed design and fabrication of a novel, bench-scale prototype reactor. Previous, relevant reactor concepts are discussed and design goals are outlined. An indirectly-irradiated fluidized bed reactor was fabricated using a combination of off-the-shelf and custom parts. Instruments to monitor temperatures and provide consistent mass flow rates were installed in the system. Gas analysis at the outlet allowed for temporal monitoring of chemical conversion and selectivity. The HFSS is described, including flux calibrations.

Chapter 6 presents the experimental methodology and procedures for "on-sun" testing. Steady-state system response was examined for four gas inlet conditions. Experimental results were statistically analyzed using analysis of variance (ANOVA) in terms of temperatures, H_2:CO ratio, carbon conversion, solar-to-fuel efficiency, cold gas ratio, and CO_2 production. Implications of the results are discussed and compared with previous literature.

The study conclusions and contributions to the field are presented in Chapter 7. Research contributions from previous sections are restated, and recommendations for future work are given.

CHAPTER 2. REACTOR CONCEPT MODELING

2.1 Introduction

This chapter presents a novel hybrid solar/autothermal gasification process concept and evaluates it through a transient finite-volume model. A review of relevant studies on autothermal and solar gasification is provided. Equilibrium compositions were analyzed across a range of temperatures and pressures to determine expected chemical products. Enthalpy change calculations allowed for the prediction of when the overall reaction would be endothermic/exothermic. Model inputs and methodology behind the heat and mass transfer modeling are presented. The model was built to examine the performance a 5-MW_{th}-scale hybrid reactor across multiple days of operation. A control system was implemented to vary the incoming reactants and adjust the temperature of the reaction zone. The results from four days of operation were compared to a baseline case with no solar irradiation (autothermal-only) to examine process benefits. In addition, simulations were run at different times of the year to examine the effect of seasonal changes. Implications of the modeling results are discussed.

2.2 Relevant Literature

2.2.1 Autothermal Gasification

Autothermal gasification is a process that has been commercially implemented for decades, but has experienced fluctuating levels of interest and investment due to the varying prices of oil and gas. In countries with abundant coal resources, it has been developed as a viable path to liquid hydrocarbons. As such, there is a wealth of literature

on autothermal gasification and more recent studies are the focus of this review. A modeling study by Botero *et al.* [18] examined the high-pressure autothermal gasification of a coal-CO_2 slurry at 30 bar and found that it achieved 7% lower carbon conversion than a coal-H_2O slurry. In addition, CO-inhibition led to a drop 60% in kinetics compared to coal-H_2O that resulted in reduced O_2 savings.

Yoon *et al.* [8] examined the non-catalytic autothermal gasification of woody biomass. The study analyzed the effects of varying the equivalence ratio and steam-to-biomass ratio on gasification efficiency and carbon conversion. Thermodynamic equilibrium predictions deviated from experimental tests due to non-uniform mixing of reactants, non-uniform temperatures, heat losses, slow reaction rates, and the formation of longer hydrocarbons. Temperatures exceeding 837 K were reached without an external heat source once ignition took place. The study concluded that increasing the equivalence ratio and the steam-to-biomass ratio was found to increase carbon conversion and gasification efficiency. However, steam-to-biomass ratio needs to be monitored in order to keep tar formation low. The use of secondary equipment to clean the gas contributes to a significant portion of biofuel production costs [19].

Kihedu *et al.* [20] examined the gasification of biomass pellets in an updraft packed-bed reactor. Cold gas ratios of about 0.91 were achieved for both air-only and air-H_2O gasification, and air-H_2O gasification achieved carbon conversion of about 0.91 as compared to 0.84 for air-only gasification. Cold gas ratio is a measure of the energy content of the product gas as compared to the feedstock, and is developed further in a subsequent section. Wang and Chen [21] examined the co-gasification of biomass and coal using an autothermal fluidized-bed gasifier. The coal combustion and biomass steam

gasification processes were time-segregated to reduce N_2 in the product stream. Reaction temperatures reached between 1148 and 1248 K and higher temperatures led to higher H_2 and CO concentrations as well as higher energy and exergy efficiencies for the product gas.

Sandeep and Dasappa [22] performed and energy and exergy analysis of oxy-H_2O and air gasification of woody biomass using a scaled-down downdraft gasifier. The study found oxy-steam gasification to have lower energy and exergy losses than air gasification due to lack of N_2. Maximum efficiencies were achieved at a molar steam-to-biomass ratio of 0.75, and higher steam-to-biomass ratios were found to favor higher H_2 production at the expense of efficiency. Kruesi *et al.* [23] compared a solar and autothermal gasification system in terms of efficiencies and gas compositions using a thermodynamic model. There were clear benefits to running a solar process compared to an autothermal process with theoretical cold gas ratios of 1.26 and 0.95, respectively.

2.2.2 Solar Gasification

2.2.2.1 Fossil Fuels

The solar gasification of fossil fuels has been heavily researched as a means of producing high-quality syngas and was demonstrated in early studies by Gregg *et al.*, [24] Taylor *et al.*, [14] and Mathur *et al*. [25]. Ng and Lipiński [26] performed a thermodynamic analysis of solar gasification on anthracite, bituminous, lignite, and peat coal. The study found that using a solar gasification process to produce liquid fuels reduced the specific CO_2 emissions by at least 39% compared to conventional autothermal coal gasification. Trommer and Steinfeld [27] determined the kinetic rate constants for steam gasification

of petroleum coke (petcoke) in the temperature range of 500 – 1520 K using a thermogravimetric analyzer (TGA). Trials were performed in the absence of O_2 to simulate solar-driven allothermal gasification.

Trommer *et al.* [28] experimentally analyzed the thermodynamics and kinetics of solar gasification of petcoke in a fluidized bed and found that syngas containing an equimolar mixture of H_2 and CO was produced at temperatures greater than 1350 K. Z'Graggen *et al.* [29] continued this work and developed and tested a prototype vortex-flow solar reactor. The reactor yielded conversions of up to 87% for petcoke and 9% solar-to-chemical energy conversion efficiency. The experimental data were used to validate the kinetic model, and predicted efficiencies of scaled-up reactors increased markedly with power output. A later study evaluated the solar gasification of a petcoke-water slurry and varied parameters such as particle size and slurry stoichiometry [30]. In general, smaller particles led to faster apparent reaction kinetics and higher chemical conversion. Lower water-to-petcoke stoichiometric ratios led to lower mass flow rates and, consequently, higher residence times and increased petcoke conversion.

Von Zedtwitz *et al.* [31] developed a numerical model to characterize the gasification of coal in a fluidized bed reactor. The model was based on the Monte Carlo ray tracing method and experimentally validated using temperature profiles and gas composition data collected from a fluidized bed of coal particles under direct solar irradiation. A similar approach was used by Z'Graggen *et al.* [32] with the Monte Carlo ray tracing method generalized to other types of carbonaceous feedstocks in a two-phase flow with coupled radiative, convective, and conductive heat transfer. The numerical

model agreed well with experimental data obtained from gasification in a prototype solar reactor.

Maag *et al.* [33] developed a numerical model for a CH_4 flow laden with C particles under direct solar irradiation and experimentally validated it using a prototype solar reactor. Maximum CH_4 conversion was 46.5%, and the chemical reaction had a relatively low contribution to the energy balance (<1%). Melchior *et al.* [34] modeled and examined the solar gasification of beech charcoal particles in a tubular reactor, with the reaction rate determined using a TGA. In the overall energy balance, reradiation and conduction losses accounted for over 80% of heat losses. The study found that conductive losses were significantly reduced and chemical energy conversion efficiencies improved in a scaled-up reactor model due to a larger volume-to-surface ratio. Piatkowski *et al.* [35-38] completed modeling and experimental testing of solar gasification in a packed-bed reactor with a wide range of feedstock materials, including beech charcoal and South African coal, along with several waste materials with low fixed carbon contents.

Gokon *et al.* [39] designed and tested an internally circulating fluidized-bed solar gasification reactor and reacted coal coke particles and CO_2 to create syngas. The study achieved peak solar-to-chemical conversion efficiencies of 12% and carbon conversions of 73%. As the experiments progressed, a deposition of ash particles reduced the amount of solar energy incident on the bed. This was followed by further studies into steam gasification using an internally-circulating fluidized bed, reaching carbon conversions of up to 88% and solar-to-chemical conversion efficiencies of up to 13% [40, 41].

Martinek *et al.* [42, 43] performed comprehensive modeling of a multi-tube solar reactor with specularly-reflective walls for steam gasification. Experimental validation agreed well with theoretically-predicted temperatures. Temperatures reached up to 1813 K, corresponding with a maximum conversion of 40%. The greatest losses occurred through conduction along the tube to the cooler walls. Temperatures were also highly non-uniform between tubes. Further modeling found insulated, absorbing cavity walls to produce higher, more uniform temperatures with longer heated tube lengths than reflective cavity walls [44]. As a result, absorbing walls allow for higher carbon conversions and solar-to-fuel efficiencies.

2.2.2.2 Biomass

Using biomass (*e.g.*, energy crops, agricultural residues, organic factory waste, etc.) as a feedstock for solar gasification has the added benefit of being carbon-neutral. That is, any carbon released to the atmosphere during biomass consumption as a fuel is directly offset by atmospheric carbon that the plant fixes during photosynthesis. This excludes carbon emissions that are generated by using fossil fuels for harvest, transportation, and processing of the feedstock material. There has been a recent push to research the utility of biomass in a solar gasification process. Lédé [15] discussed the possible application of solar energy to thermochemically convert biomass composed of cellulose, hemicellulose, and lignin to syngas. Solar gasification may alleviate a number of issues with conventional autothermal biomass gasification, potentially giving it an economic advantage. These issues include tar formation, biomass moisture, and the costliness of secondary equipment for biomass pretreatment and gas cleaning [19, 45-47].

A study by Murray and Fletcher [48] examined the solar gasification of cellulose in both directly and indirectly-irradiated fluidized bed reactors in the temperature range of 1050-1600 K. No char accumulation was seen at temperatures above 1300 K. The indirectly-irradiated designs using steel took several times longer to reach steady state than the quartz fluidized bed, indicating a heat transfer limitation with an indirectly-irradiated design.

Perkins *et al.* [49] experimentally investigated the high-temperature gasification of corn stover in a particle flow reactor. Experiments did not use a solar simulator, but a high temperature furnace was designed to mimic solar thermal conditions. The study examined the effects of particle size, reactor temperature, steam concentration, and residence time on carbon conversion. Higher conversion and lower tar formation were achieved at higher temperatures (1429 K), and selectivity of CO over CO_2 increased with decreasing steam concentration. This indicated that concentrated solar energy could be a viable path towards conversion of high fixed-carbon biomass into syngas.

Lichy *et al.* [50] tested the gasification of cellulose, lignin, and *Poa Pratensis* ("Kentucky Bluegrass") in a high temperature furnace reactor and corn stover and sorghum in a solar reactor. An entrained-flow reactor consisting of multiple tubes within a highly reflective cavity was tested in a parabolic mirror setup. Ray trace modeling was used to optimize the absorber tube arrangement, though further optimization studies were deemed necessary to increase efficiencies. At 1273 K tar formation occurred, but was significantly reduced at temperatures of above 1473 K. Conversions of corn stover and sorghum reached 62.8% and 53.9%, respectively.

Hertwich and Zhang [51] modeled three scenarios comparing the solar gasification of biomass with biomass-fired gasification and coal gasification. The efficiencies, CO_2 emissions, and capital costs were estimated for each process. Solar gasification did not require CO_2 sequestration due to the low emissions during the conversion process but did have higher land use requirements and higher capital costs than coal gasification. It was expected that the high capital costs would be more than offset by lower fuel costs in a commercial setting. In addition, solar gasification had a significantly lower land use requirement than biomass-fired gasification and had the highest energy conversion efficiency of all three scenarios.

Hathaway *et al.* [52] examined biomass pyrolysis and steam gasification using molten ternary eutectic alkali carbonate salt blend as a heat transfer medium. Cellulose was gasified between 1124 K and 1235 K in a reactor containing a liquid salt. The molten salt also acted as a catalyst and increased the rate of pyrolysis by 74% and gasification rate by over an order of magnitude as compared to gasification without the salt. A further benefit of using the molten salt was its ability to smooth out thermal transients, which frequently occur in solar applications.

Kruesi *et al.* [23, 53] modeled and experimentally validated a combined drop-tube and fixed-bed solar gasification reactor using sugarcane bagasse. The concept utilized a drop-tube to provide an initial zone where the feedstock could undergo fast pyrolysis and fixed bed with a porous ceramic where the char could undergo a slower gasification process at longer residence times. Using an electric furnace that reached temperatures between 1073 and 1573 K, product gases were analyzed gases from the biomass gasification, and cold gas ratios of 1.12 were achieved. The two-zone design was further

tested in a high-flux solar simulator, and it was able to better decompose CH_4 and C_2 hydrocarbons as compared to a drop-tube reactor. Maximum energy conversion efficiencies reached 21%. A method of quickly removing the ash from the porous ceramic to improve throughput was identified as a potential area for further research.

2.2.3 Additional Studies

Kaniyal *et al.* [54-56] evaluated combined solar/autothermal gasification concepts from a systems and techno-economic perspective. Sudiro and Bertucco [57] modeled a combined coal gasification and methane steam-reforming system that utilized solar energy during the day. The authors employed average daily solar irradiation data and noted the necessity of using methane to provide the process heat at night. However, such efforts have not addressed the need to precisely control input flows based on reactor conditions, critical due to the transient nature of solar disturbances. Very few previous works have focused on the control of solar-thermal reactors through manipulation of inlet flows. Petrasch *et al.* [58] developed a linear feedback controller to adjust steam inlet flow rate for solar disturbances in a continuous petcoke gasification reactor and found improvements in efficiency over an uncontrolled system. Saade *et al.* [59] used a model predictive control system to manipulate steam and inert gas flows in a solar gasification reactor to minimize the effect of disturbances and found that it outperformed a more conventional multi-loop feedback system.

2.3 Equilibrium Compositions

Equilibrium compositions were determined via Gibbs free energy minimization over a range of temperatures and pressures. Thermophysical properties were extracted from

literature [60] and implemented in the model with a constrained minimization function [61].

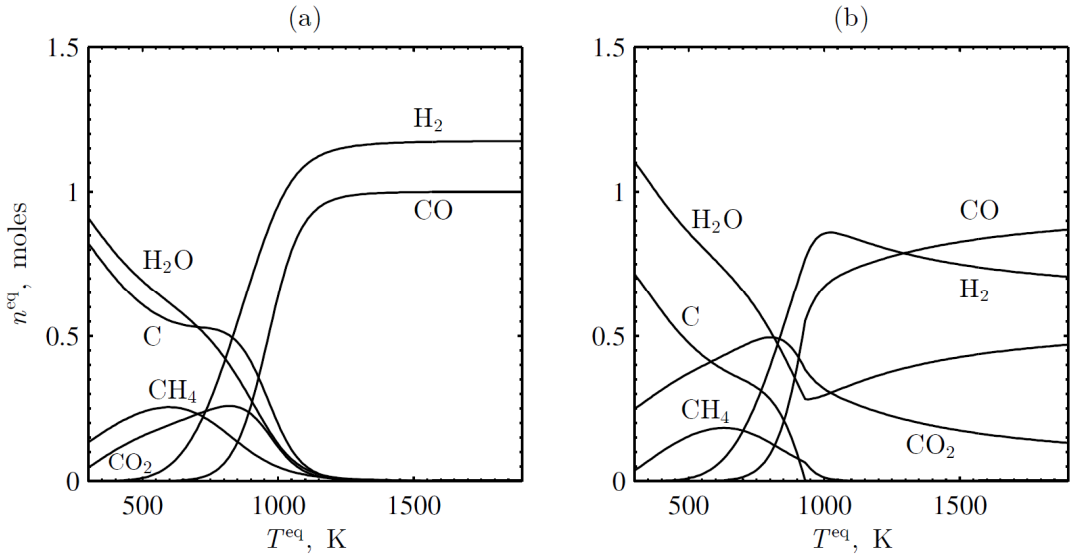

Figure 2.1 Equilibrium compositions at 1 bar as a function of temperature between 300 and 1900 K for the (a) $CH_{0.81}O_{0.23}$ + $0.77H_2O$ and (b) $CH_{0.81}O_{0.23}$ + $0.77H_2O$ + $0.3O_2$ systems.

Lignite coal was chosen as the feedstock due to its abundance and relatively high reactivity [62]. Lignite coal has a composition of $CH_{0.81}O_{0.23}$ and a lower heating value (LHV) of 28,500 kJ/kg [63]. Equilibrium compositions for the $CH_{0.81}O_{0.23}$ + $0.77H_2O$ system are shown in Figure 2.1a from 300 – 1900 K. The upper temperature bound is consistent with coal gasification technologies that operate at ~42 bar and reach 1873 K [64]. At lower temperatures, large amounts of C remain unreacted at equilibrium and the formation of CH_4 steadily increases until 600 K, and then decreases until it is no longer forecast above 1200 K. The H_2O(v) gradually decreases until it no longer remains at equilibrium above 1200 K. CO_2 is forecast at lower temperatures with a peak at about 800 K, and decreases as the Boudouard reaction becomes more thermodynamically

favorable. Both CO and H_2 appear at 700 K in the products at equilibrium and continue to increase with temperature. At above 1000 K, CO and H_2 are the primary constituents forecast at equilibrium as only residual amounts of C remain.

In autothermal gasification, O_2 is added to the system, which results in highly-exothermic combustion that produces CO_2 and H_2O. Partial combustion of the feedstock (*i.e.*, a fuel-rich mixture), occurs during autothermal gasification where process heat is produced. The equilibrium compositions for the $CH_{0.81}O_{0.23} + 0.77H_2O + 0.3O_2$ system are shown in Figure 2.1b. The formation of CH_4 reaches a peak at about 600 K then steadily decreases with temperature. Almost no C remains in the system at temperatures above 900 K. CO and H_2 are no longer forecast to be the sole products above 1200 K as the reverse water-gas shift reaction becomes favorable at elevated temperatures, decreasing the H_2:CO ratio.

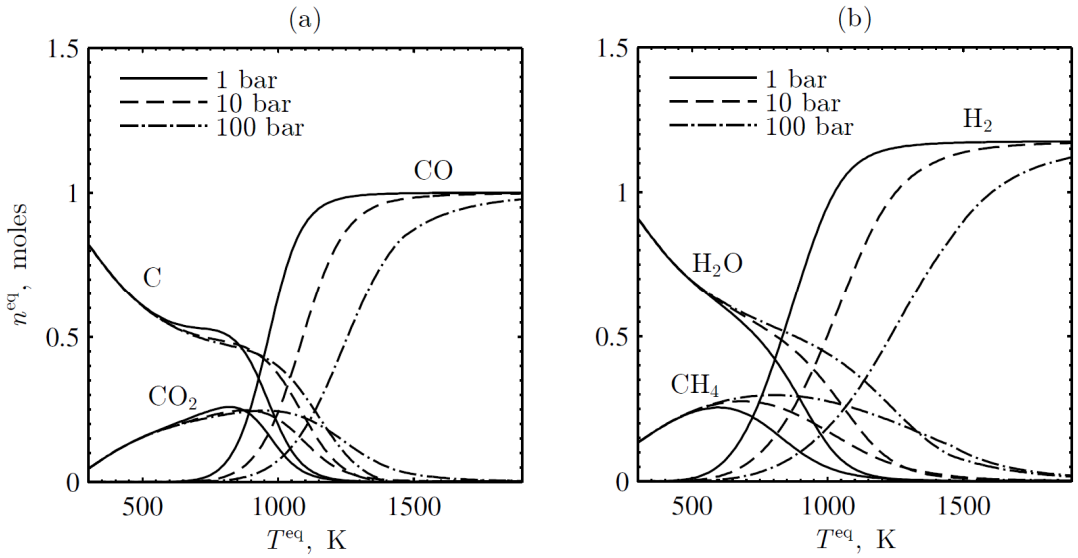

Figure 2.2 Equilibrium compositions at 1, 10, and 100 bar as a function of temperature for the $CH_{0.81}O_{0.23}$ + $0.77H_2O$ system (a) C-containing species and (b) H-containing species.

Figure 2.2 shows the equilibrium compositions for pressures of 1, 10, and 100 bar for the $CH_{0.81}O_{0.23}$ + $0.77H_2O$ system as function of temperatures for (a) C-containing and (b) H-containing species. The elevated pressures cause the C, CO_2, CH_4, and H_2O to shift to larger amounts and CO and H_2 to smaller amounts at higher temperatures, particularly within 700-1500 K temperature range according to Le Chatelier's principle.

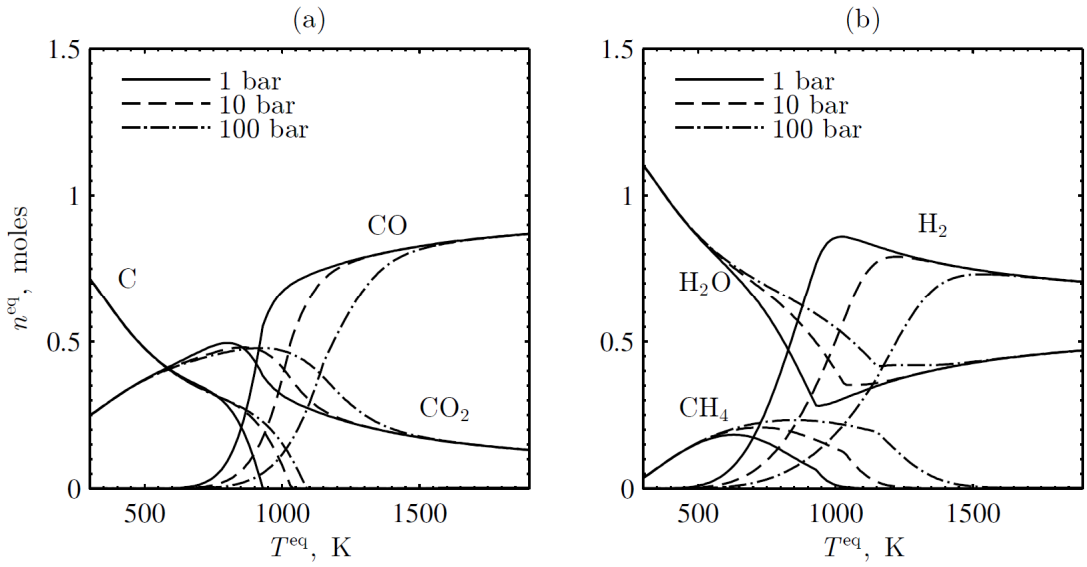

Figure 2.3 Equilibrium compositions at 1, 10, and 100 bar as a function of temperature for the $CH_{0.81}O_{0.23}$ + $0.77H_2O$ + $0.3O_2$ system (a) C-containing species and (b) H-containing species.

Figure 2.3 shows the equilibrium compositions for the same pressures for the $CH_{0.81}O_{0.23}$ + $0.77H_2O$ + $0.3O_2$ system. The same trend can be seen with lower CO and H_2 yields at moderate temperatures with higher pressures.

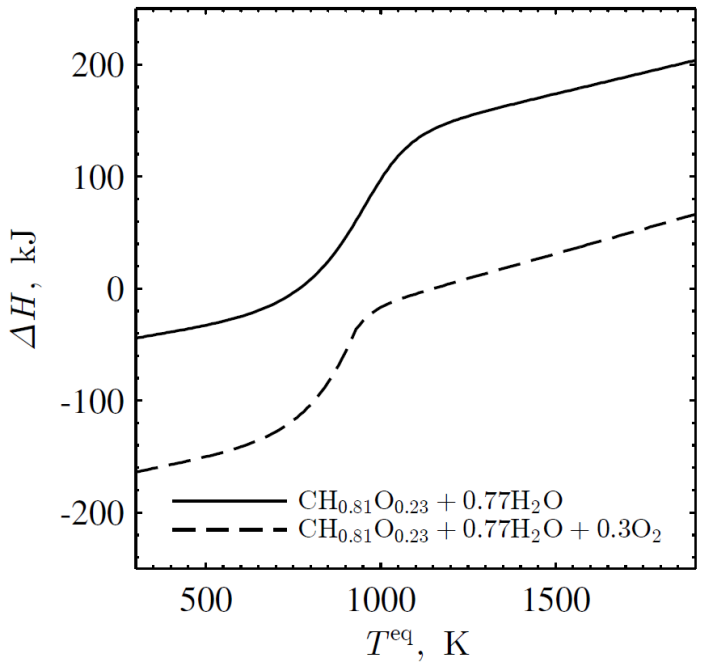

Figure 2.4 Reaction enthalpy as a function of temperature for the $CH_{0.81}O_{0.23}$ + $0.77H_2O$ and $CH_{0.81}O_{0.23}$ + $0.77H_2O$ + $0.3O_2$ systems at 1 bar.

The reaction enthalpies for the $CH_{0.81}O_{0.23}$ + $0.77H_2O$ and $CH_{0.81}O_{0.23}$ + $0.77H_2O$ + $0.3O_2$ systems are shown in Figure 2.4 from 300 – 1900 K, determined as:

$$\Delta H = \sum_{products} n_i \overline{h}_i \left(T^{eq}\right) - n_{H_2O} \overline{h}_{H_2O} \left(473K\right) - n_{coal} \overline{h}_{coal} \left(300K\right) \tag{2.1}$$

where n_i is the moles of species i and $\overline{h}_i(T)$ is the molar specific enthalpy of species i at temperature T. The reaction enthalpy contains both the sensible heat required to heat the reactants and the heats of formation. The reactants are 473 K steam and ambient temperature (300 K) coal. Steam temperature was chosen based on previous entrained-flow solar reactor modeling [12]. Possible energy sources to preheat the steam include sensible heat from the products, waste heat from downstream F-T synthesis, or a separate solar process.

The overall reaction is endothermic in the absence of O_2 at temperatures greater than 800 K. It becomes exothermic at lower temperatures due to lower energy species such as H_2O and CO_2 favored at equilibrium. With the addition of O_2, the overall reaction is exothermic at temperatures below 1200 K. This shift to lower ΔH across all temperatures is due to the complete consumption of the O_2 in combustion reactions.

2.4 Modeling the Hybrid Solar/Autothermal Reactor

The hybrid solar/autothermal reactor is schematically depicted in Figure 2.5. During on-sun operation, concentrated solar irradiation enters the hybrid solar/autothermal reactor through a quartz window and impinges directly on a SiC emitter plate. SiC has both a high absorptivity over the solar spectrum and thermal conductivity and a low coefficient of thermal expansion, making it an ideal material for application in high-temperature solar reactors. The two-cavity configuration, or indirect reactor design, allows more sunlight to be captured without fouling of the window [65]. The cavity was modeled with walls constructed of Al_2O_3, which has previously been used for reactor liner and insulation in prototype solar reactors [30, 36]. Al_2O_3 acts as ceramic insulation that absorbs, emits, and reflects radiation. In practice, a multi-material or component design would likely be necessary to mitigate the stress effects of rapid thermal shocks. Many previous indirectly irradiated reactor designs use windows [12, 38, 44, 66], and a windowed design has the additional advantage of mitigating heat losses at night [67]. The cylindrical cavity shape increased the apparent emissivity of the window to 0.95. The absorbed heat is transferred via conduction to the reaction zone, and the thermal inertia of the reactor also reduces the severity of thermal shocks (*e.g.*, from intermittent cloud cover).

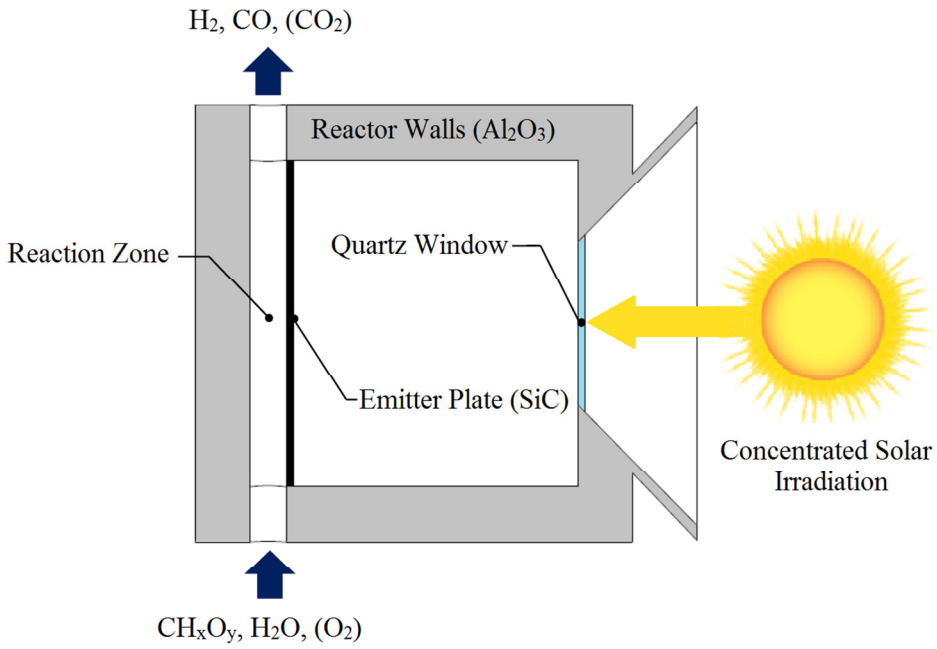

Figure 2.5 Schematic depiction of the hybrid solar/autothermal reactor. Concentrated solar irradiation enters the quartz window and is absorbed by the emitter plate. The emitter plate delivers heat to the reaction zone via conduction.

Specific heats and thermal conductivities were determined as functions of temperature [68-70], and spectral optical properties were determined from compiled radiative property information [67, 71]. The radiative heat transfer between surfaces was modeled using a two-band approximation, where the transparent and opaque wavelength intervals for quartz are 0-λ_c and λ_c-∞, respectively, with λ_c = 4μm. The surfaces were assumed to be diffuse emitters and reflectors.

Carbonaceous materials and H_2O(v) are introduced into the reaction zone. Heat via conduction and thermal radiation is transferred to the reactants, resulting in the production of syngas at greater than 1100 K at 1 bar. The products are removed from the reactor from the top and chemical equilibrium is assumed. During periods with little or no available sunlight, O_2 is added to the inlet reactant stream, and the resulting combustion provides the process heat to ensure continuous production of syngas.

The hybrid solar/autothermal reactor was designed for use in Sandia National Laboratories' National Solar Thermal Test Facility (NSTTF) in Albuquerque, New Mexico. NSTTF has a heliostat field capable of providing over 5 MW_{th} in solar power and solar concentration ratios of over 3000 suns (the solar concentration ratio is defined as the solar radiative flux normalized to 1 kW/m^2, often expressed in units of "suns"). Hourly direct-normal irradiance (I_{DN}) and ambient temperature (T_{amb}) data were obtained in the form of typical meteorological year (TMY3) data [72] for Albuquerque, NM. The estimate of the heliostat field optical efficiency of 62% is from literature [73].

The hybrid solar/autothermal reactor operates in three general modes: 1) solar gasification for periods of high I_{DN}, 2) autothermal gasification for nighttime operation, and 3) a combined system during periods of insufficient I_{DN}. During operation, the temperature of the reaction zone and syngas output are monitored, and the flow of O_2, H_2O, and/or carbonaceous material to the system are dynamically adjusted to address deficiencies of I_{DN} in order to maintain a prescribed temperature, allowing for continuous, 24-h production of syngas for a subsequent F-T synthesis.

The simplified modeling focused on capturing the primary flows of heat and mass coupled to the chemical equilibrium predictions to assess the potential of such a process over long periods of time. The wall, emitter plate, and quartz window were modeled assuming one-dimensional, transient heat conduction for radial and Cartesian systems, represented as:

$$\rho c_p \frac{\partial T}{\partial t} = \frac{1}{r}\left(\frac{\partial}{\partial r}\left(kr\frac{\partial T}{\partial r}\right)\right) \text{ or } \rho c_p \frac{\partial T}{\partial t} = \left(\frac{\partial}{\partial x}\left(k\frac{\partial T}{\partial x}\right)\right) \tag{2.2}$$

where T is the temperature, t is the time, r and x are distances, and ρ, c_p, and k are the density, specific heat, and thermal conductivity of the material, respectively. The model employed a finite-difference grid for the control-volume method that was solved using an explicit solution scheme. Stability was maintained by interpolating the input data to allow for a 20-s time step. Grid independence for the reactor walls was determined by spatially discretizing the walls until the percent difference in temperatures was <5%. The boundary conditions on the outside of the reactor are represented as:

$$\begin{aligned} q''_{\mathrm{w}} &= -k \left. \frac{\partial T(t)}{\partial n} \right|_{\mathrm{w}} \\ &= h\left(T_{\mathrm{w}}(t) - T_{\infty}(t)\right) + \sigma\left(T_{\mathrm{w}}^4(t) - T_{\mathrm{sky}}^4(t)\right)\left(\varepsilon_1 f\left(T_{\mathrm{w}}(t)\,\lambda_{\mathrm{c}}\right) + \varepsilon_2\left(1 - f\left(T_{\mathrm{w}}(t)\,\lambda_{\mathrm{c}}\right)\right)\right) \end{aligned} \tag{2.3}$$

where n indicates the directional displacement normal to the surface, T_{w} is the wall surface temperature, T_{∞} is the ambient air temperature, h is the convective heat transfer coefficient, σ is the Stefan-Boltzmann constant, ε is the spectral emissivity of the surface, and f is the fractional function for temperature T_{w} over 0-λ_{c}. Within the cavity, only radiative heat transfer was considered due to negligible convective heat transfer effects in the evacuated cavity. Convective heat transfer coefficients for other parts of the reactor were found from known correlations for cylinders and flat plates [74]. Air velocities were estimated based on average annual wind speeds.

The radiosity method for enclosures was used to analyze the radiative exchange in the evacuated cavity, where multiple reflections, absorptions, and reemissions occur. Analytical solutions for view factors were used [75]. Each temperature node in the first

cavity had two radiosity equations for bandwidths of 0-λ_c and λ_c-∞ and are represented, respectively, as:

$$\frac{q_i}{\varepsilon_i} - \sum_{j=1}^{N}\left(\frac{1}{\varepsilon_j} - 1\right) F_{i-j} q_j + H_{oi} = f\left(T_i \lambda_c\right) E_{b,i} - \sum_{j=1}^{N} F_{i-j} f\left(T_i \lambda_c\right) E_{b,i} \tag{2.4}$$

$$\frac{q_i}{\varepsilon_i} - \sum_{j=1}^{N}\left(\frac{1}{\varepsilon_j} - 1\right) F_{i-j} q_j = \left(1 - f\left(T_i \lambda_c\right)\right) E_{b,i} - \sum_{j=1}^{N} F_{i-j} \left(1 - f\left(T_i \lambda_c\right)\right) E_{b,i} \tag{2.5}$$

where q_i is the net heat flux of surface i in a given wavelength band, $F_{i\text{-}j}$ is the view factor of j seen from i, ε_i is the spectral emissivity of surface i, H_{oi} is the solar irradiation incident on surface i, $E_{b,i}$ is Planck's total blackbody emissive power of surface i, and f is the fractional function for the temperature of surface i over 0-λ_c.

The radiosity equation for the semi-transparent window is similarly represented as:

$$\frac{q_i}{1-\rho_i} - \sum_{j=1}^{N}\left(\frac{\rho_j}{1-\rho_j}\right) F_{i-j} q_j + H_{oi} = \frac{\alpha_i}{1-\rho_i} f(T_i \lambda_c) E_{b,i} - \sum_{j=1}^{N}\left(\frac{\alpha_j}{1-\rho_j}\right) F_{i-j} f(T_i \lambda_c) E_{b,j} \tag{2.6}$$

where ρ_i and α_i are the slab spectral reflectivity and absorptivity of the quartz window, respectively. The window was treated as a single uniform temperature volume with an associated thermal capacitance. The solar irradiation was treated as a collimated beam transmitted through the quartz window and directly impinged on the emitter plate.

The zonal method was used to determine the radiative exchange within the reaction zone considering a participating medium [76], represented as:

$$\sum_{j=1}^{N}\left(\frac{\delta_{ij}}{\varepsilon_j}-\frac{\rho_j\overline{s_i s_j}}{\varepsilon_j A_j}\right)\varepsilon_j A_j H_{oj}=\sum_{j=1}^{N}\overline{s_i s_j}\varepsilon_j E_{bsj}+\sum_{k=1}^{K}\overline{s_i g_k}E_{bgk} \tag{2.7}$$

where δ_{ij} is the Kronecker delta, A_j is the area of surface j, ρ_j is the reflectivity of surface j, $\overline{s_i s_j}$ is the direct exchange area between surfaces i and j, H_{oj} is the total irradiation per unit area on surface j, and $\overline{s_i g_k}$ is the surface-to-volume direct exchange area from surface i to volume k. Direct exchange areas for surface-volume and surface-surface radiative exchanges were computed using a Monte Carlo analysis with 10^6 rays, assuming $\kappa = 4$ m^{-1} based on previous modeling of vortex and flow and tubular reactors [32, 42]. Negligible thermal capacitance, uniform absorption coefficient, gray absorption and emission, and a uniform temperature were assumed in the reaction zone volume due to rapid radiative exchange. The assumption of negligible particle thermal capacitance was made due to the thermal capacitance of the reactor walls being several orders of magnitude higher and the particles constantly being replaced within the reaction zone. The particles were assumed to be absorbing, emitting, and non-scattering. In reality, small carbonaceous particles tend to exhibit forward scattering behavior [32, 33], which would not significantly affect temperatures due to the large parallel disk geometry of the reaction zone. An iterative procedure was used to calculate equilibrium amounts and reaction zone temperature at each time step. A total H_2 + CO production rate of ~3.5 mol/s was chosen for the reactor model.

2.5 Model Operation and Control[1]

A feedback control system was used to control temperature by adjusting the inputs to the hybrid solar/autothermal reactor with the primary goal of maintaining the reaction zone temperature, T_{reac}, above a given setpoint. A simplification of the reactor model was created to analyze the control design problem through the use of linear transfer function models. The controller was synthesized using the linear model of the system and a loop shaping filter according to the McFarlane Glover H-infinity loop shaping procedure [78]. This method was chosen to ensure the robustness of a controller designed primarily to achieve bandwidth and steady error design goals. The first control design step included the design of a simple PI control system that minimized steady error (zero steady state error for the linear approximate model) and achieved a high bandwidth (characteristic time of approximately 125 s). Once the PI design was created, a "robustifying" controller was used to increase the robustness to uncertainties of the closed-loop control system.

2.5.1 Simplified Model

A control oriented model was created to help demonstrate the requirements for control design to achieve performance and stability goals. There were two major inputs, I_{DN}, treated as a disturbance, and the quantity of the reactants fed into the reactor. To analyze the system from a control point of view, a linear approximate model was formed by fitting linear model time responses to the response of the high fidelity model given small step inputs. This was done for each of the two inputs with respect to the output of T_{reac}. The linear model with two inputs and one output is represented as:

[1] This section includes work by Tyler Shinn and Roger Fales, and is published in [77]

$$y(t) = \begin{bmatrix} G_{\mathrm{d}} & e^{-s\tau}G \end{bmatrix} \begin{Bmatrix} d(t) \\ u(t) \end{Bmatrix} \tag{2.8}$$

where *d(t)* is the disturbance input due to solar irradiation variations and *u(t)* is the control effort which is equivalent to the amount of additional reactants, O_2 and coal, fed into the reactor. At the input of the plant, *G*, there was a time delay, τ, due to the transport delay in the feeding mechanism and delay due to the implementation of the control system. A transfer function was selected for the disturbance (G_{d}) and the plant (*G*) to match the response of the high fidelity model response given the same inputs to I_{DN} disturbance, *d*(*t*) and control effort (input coal and O_2), *u*(*t*). An optimization routine that penalized the square error between the linear model response and the high fidelity model response given the same perturbation to inputs by manipulating parameters of a transfer function yielded the following two transfer functions represented, respectively, as:

$$G = \frac{91.033\left(s + 7.455\times10^{-5}\right)\left(s + 4.112\times10^{-5}\right)}{\left(s + 8.47410^{-5}\right)\left(s + 3.47610^{-5}\right)} \tag{2.9}$$

$$G_{\mathrm{d}} = \frac{0.0026235\ (s + 4.125\times10^{-5})}{(s + 0.002083)\ (s + 2\times10^{-5})} \tag{2.10}$$

where *s* represents the Laplace operator. Note that *G* has real zeros that are close to the origin of the s-plane indicating that there will be a limitation on the performance of a feedback control system.

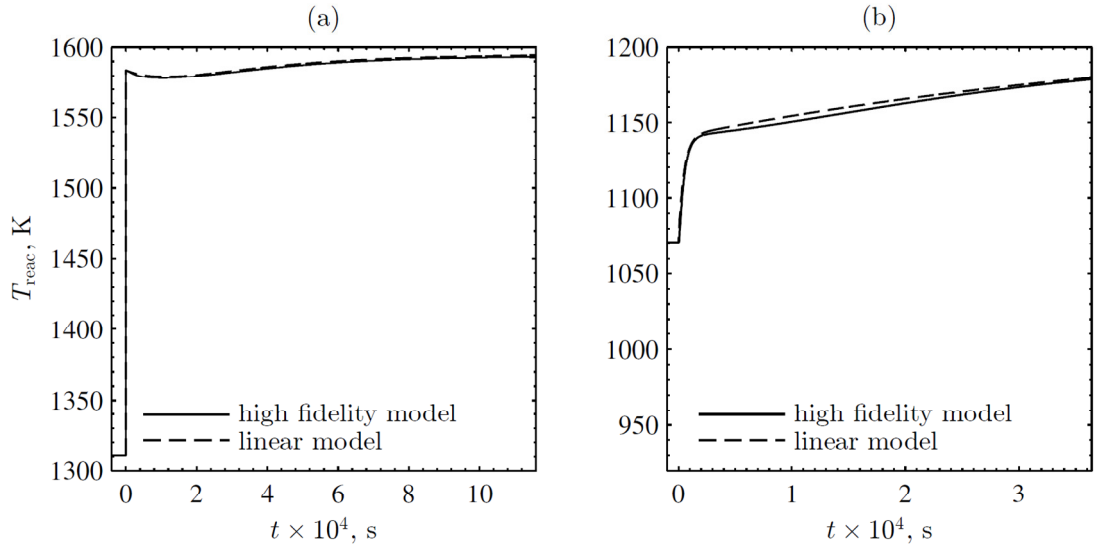

Figure 2.6 Comparison of the predicted reaction zone temperature as a function of time between the high-fidelity (solid) and simplified (dashed) models for the (a) step input response and (b) step disturbance response.

The slow zero performance limitation is combined with another limitation that is due to the time delay, $\exp(-s\tau)$, at the input of the plant. In general, time delays in the system dynamics tend to cause an upper bound on control performance [78]. The performance limitations imposed by these two characteristics of the plant form the basis for an argument for feed-forward control to improve performance in future work. Simulations using the high fidelity model and linear model were used to show the degree to which the linear model matches the response of the high fidelity model. For each simulation a step response was given to the system. The step inputs were for the control input (additional coal and O_2) and the disturbance (solar irradiation). Plots of step responses comparing the temperature responses of the high fidelity and linear models are given in Figure 2.6 for the control input and disturbance input plant models, respectively. The time delay was 20 s. These plots show that the linear models were a good

approximation of the high fidelity model since the temperature responses of the two models were similar for both input cases.

2.5.2 Control Design

A diagram of the structure of the control system is given in Figure 2.7. The diagram includes the plant G, disturbance plant, G_d, uncertainty model, $W_i\Delta$, controller, K_1 K_2, and weights used to analyze performance of the control system, W_p and W_u. A preliminary control design, K_1, was created to explore the challenges associated with the control system. The control design was a proportional integral (PI) controller with temperature feedback. The PI control design was selected to achieve a fast response with low steady state error. Minimization of overshoot and robustness were not emphasized at this stage.

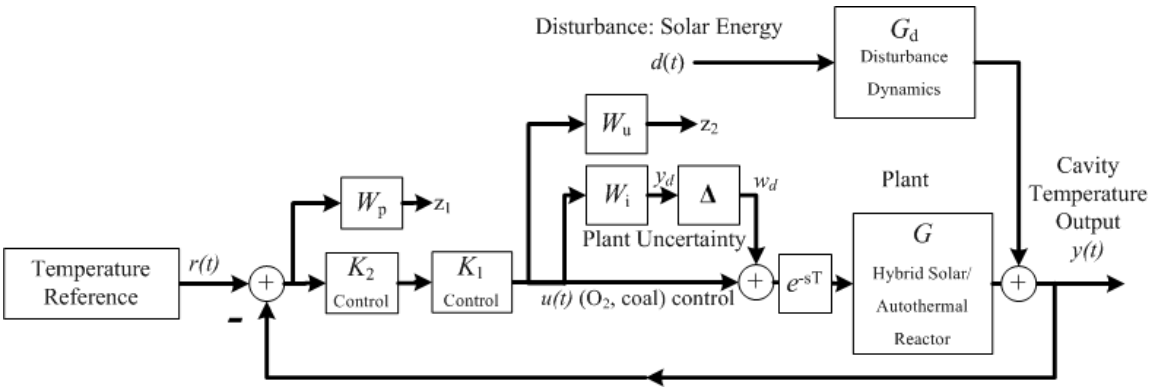

Figure 2.7 Diagram of the control system.

A first order low pass filter with a break frequency of 0.01667 rad/s was employed along with the PI controller to avoid high gains at high frequencies, which could destabilize the system due to the time delay. PI control gains were selected to produce a fast response with low steady error. A relatively high control gain was selected to reduce error due to disturbances. The integral gain reduced steady state error to zero

for step inputs and to low levels for higher order inputs for the linear system. The PI controller with low pass filter is represented as the transfer function:

$$K_1 = \frac{0.00028333(s+0.05)}{s(s+0.01667)} \tag{2.11}$$

In Figure 2.8, a simulation of the closed-loop PI temperature control system indicates that the temperature response was stable and fast but characterized by significant oscillations. Large oscillations indicated that the control system had poor robustness due to uncertainty. Uncertainty may include changes in the dynamics that could occur due to changing operating conditions, unmodeled dynamics, model information lost due to linearization, etc.

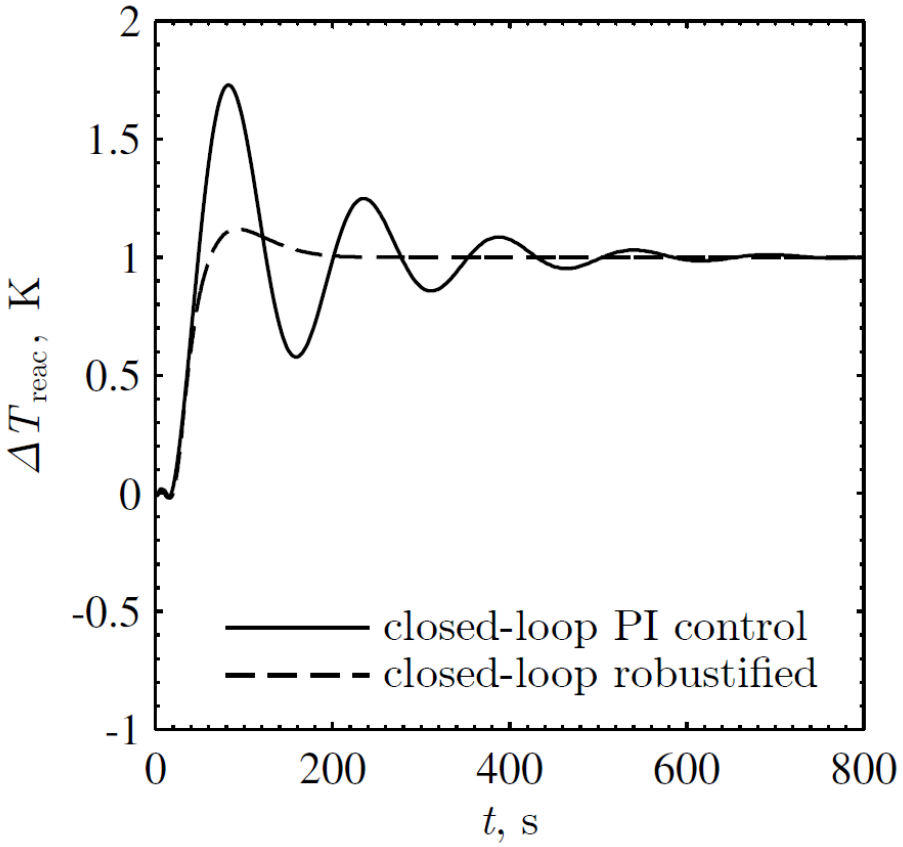

Figure 2.8 Response of the closed-loop control system applied to the linear model given a unit step change in reference set point temperature for two cases, the PI controller, K_1, and the robustified controller, PI combined with K_2.

The "robustifying" controller, K_2, shown in Figure 2.7, was designed to improve the robustness of the control system to uncertainty. The design methodology used here increases robustness to coprime factor uncertainty [79]. Details of applying the method are found in literature [78]. The resulting controller transfer function is:

$$K_2 = \frac{0.3658\left(s+0.2322\right)\left(s+0.02278\right)\left(s+7.458\times10^{-5}\right)\left(s+4.111\times10^{-5}\right)\left(s^2+0.3678s+0.06459\right)}{\left(s+0.04817\right)\left(s+7.455\times10^{-5}\right)\left(s+4.112\times10^{-5}\right)\left(s^2+0.117s+0.03415\right)\left(s^2+0.6851s+0.1768\right)} \quad (2.12)$$

With the robustifying controller applied to the closed-loop control system along with the PI controller, the response was similarly fast compared to PI only, but with low overshoot and little oscillation as shown in Figure 2.8. The robustifying controller greatly improved the time domain response characteristics.

The performance of the control system was also analyzed in the frequency domain. In Figure 2.7, performance outputs z_1 and z_2 are weighted versions of the error and control effort respectively and were used in performance analysis. The weights, W_p and W_u can be formed using design requirements. The design requirements discussed earlier were converted into frequency domain requirements as follows. The bandwidth was selected to be ω_b=0.008 rad/s due to the desired characteristic time discussed earlier. Low frequency error was required to be small such that the low frequency error specification was A=0.01 or 1% of the change in the setpoint. Transient or high frequency error was allowed to reach 200%. Therefore, a high frequency error performance specification was given as M=2. The control effort was limited to avoid this situation and overuse of control inputs. The weight on the control effort was based on the design specifications, $W_p = \frac{\frac{s}{M} + \omega_b}{s + \omega_b A}$. A limitation of 1 mole of control effort reactants per 5 degrees of temperature variation was selected. Therefore, the weight on the control effort was selected to be W_u=5. In order to achieve the desired design specifications, the gain between the inputs (reference setpoint and I_{DN} disturbance) and the output performance signals, z_1 and z_2 had the goal of being one or less for all frequencies. Based on an analysis of Figure 2.7, the transfer functions in Table 2.1 were required to have a magnitude less than 1 for all frequencies in order to meet the design specifications. The

design results in Table 2.1 indicate that the system achieved the desired performance in terms of control effort and temperature error given disturbances and changes to the reference temperature setpoint.

Table 2.1 Frequency response magnitudes of closed-loop performance transfer functions.

Transfer function	Maximum gain for all frequencies
$SK_1K_2w_u$	0.0613
$G_dSK_1K_2w_u$	0.6046
Sw_p	0.8564
G_dSw_p	0.7511

Note that $L = K_1K_2e^{-s\tau}G$, $s = \frac{1}{1+L}$, and $\tau = \frac{L}{1+L}$. Also note that a first order Padé approximation was used in place of the time delay in Table 2.1. The analysis of the closed-loop frequency responses of the performance transfer functions indicated the linear approximate reactor model responded well to the control design.

The results of the high-fidelity model are presented with the K_1K_2 control system applied in the subsequent section. Neglecting controller dynamics, the operation of the control system was such that the controller implementation allowed additional O_2 plus coal to be applied to the system when the temperature was below the set point. Again neglecting the controller dynamics, O_2 was reduced when the temperature rose above the set point, reducing the need for consumption of feedstock (coal) for temperature control purposes. Since less than zero O_2 was not possible, a saturation scheme was implemented so that once the O_2 level commanded by the control system reached zero, the control system no longer could affect the temperature and was essentially disabled. At this point, the temperature was able to rise above the given temperature set point (*e.g.*,

when abundant solar energy was available). When the controller called for an increase in O_2, the saturation scheme had no effect on the control system (*e.g.*, conditions where the temperature was below the set point and the commanded O_2 level was greater than zero).

2.6 Results and Discussion

The model was run for five consecutive days of the year to demonstrate robustness of the control algorithm. The results from the first simulation day were not included due to preheating the reactor to the proper operating temperature before chemical reactions began to take place. The two external heat transfer drivers of the model, I_{DN} and T_{amb}, are shown for the four-day period in Figure 2.9. The first day was relatively sunny with some cloud over during the middle of the day, and on the second day there were no clouds as shown by the high I_{DN}. There was intermittent cloud cover on the third day as evidenced by the low I_{DN}, and relatively few clouds on the fourth day. The T_{amb} increased during the day where it peaked and decreased as the sun set for all days.

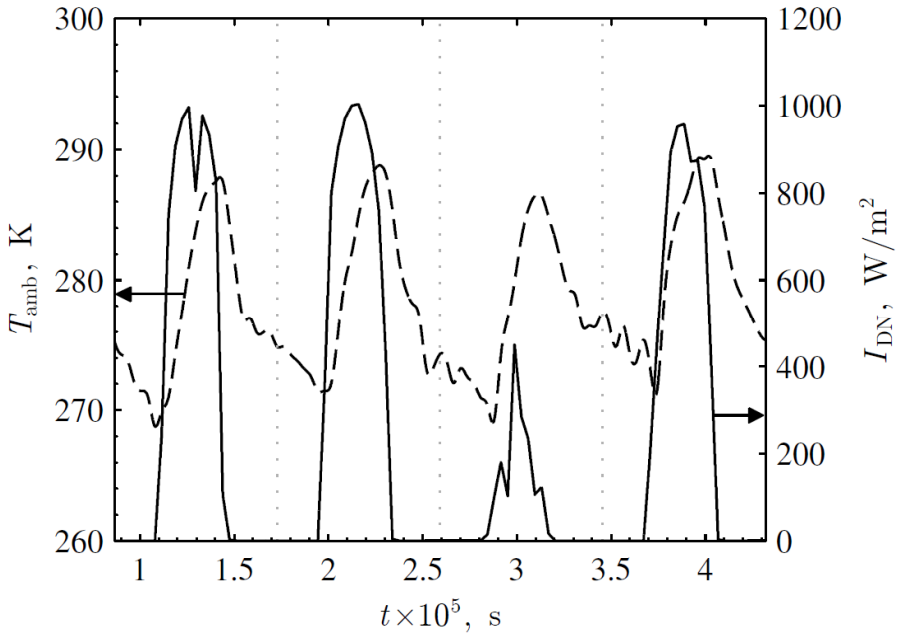

Figure 2.9 Ambient temperature (dashed) and direct-normal irradiance (solid) data for four days during the winter.

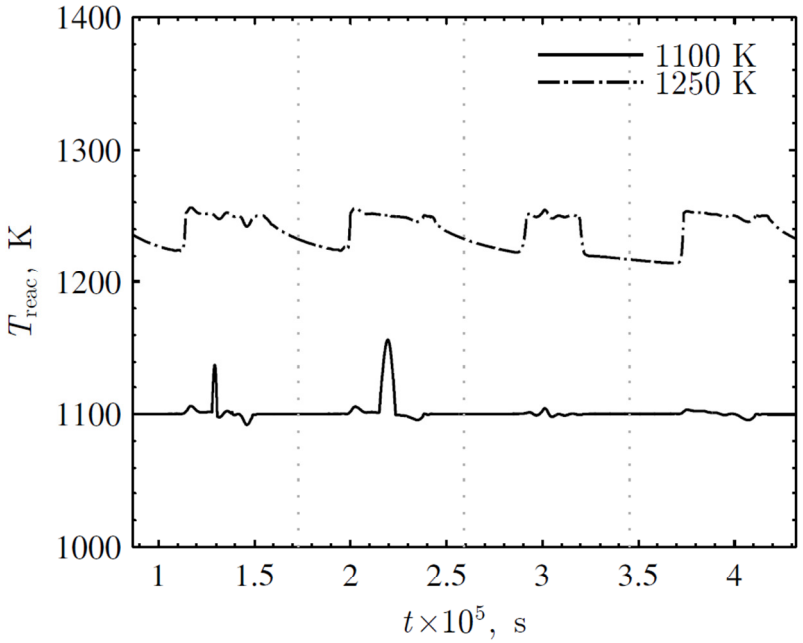

Figure 2.10 Reaction zone temperatures as functions of time for a four-day period for temperature set points of 1100 K (solid) and 1250 K (dot-dashed).

The model was run at separate minimum temperature setpoints of 1100 K and 1250 K. The reaction zone temperatures across four days of operation for the two setpoints are shown in Figure 2.10. The higher temperature setpoint of 1250 K allowed for higher conversions of the feedstock to syngas, while less O_2 was required for the lower temperature setpoint of 1100 K. At the 1250 K setpoint, T_{reac} increased and remained relatively constant when I_{DN} was available. T_{reac} decreased during the night in the absence of I_{DN} as some of the heat was stored due to the thermal mass of the reactor. At the 1100 K setpoint, T_{reac} remained constant regardless of I_{DN}, except for a few small temperature spikes during peak I_{DN}. As seen in Figure 2.10, even when I_{DN} was relatively low, the reactor temperature was maintained and could still be assisted by concentrated solar irradiation. Temperature control effort (additional O_2 and coal) was not present during times of high I_{DN} such that the temperature was above the setpoint and control effort was at zero as described in Subsection 2.5.2. The most rapid change in I_{DN} during temperature control occurred over a 2-h period, starting from approximately 1000 W/m^2 down to 0 W/m^2, with a maximum rate of decrease of 0.23 W/m^2-s. This disturbance corresponded to a temperature deviation of 3.4 K from the 1100 K set point, which was 0.31% error, and also the maximum error seen in the cavity temperature for all temperature control periods during the simulation. When the set point was 1250 K, the temperature control errors were larger but still reasonably low.

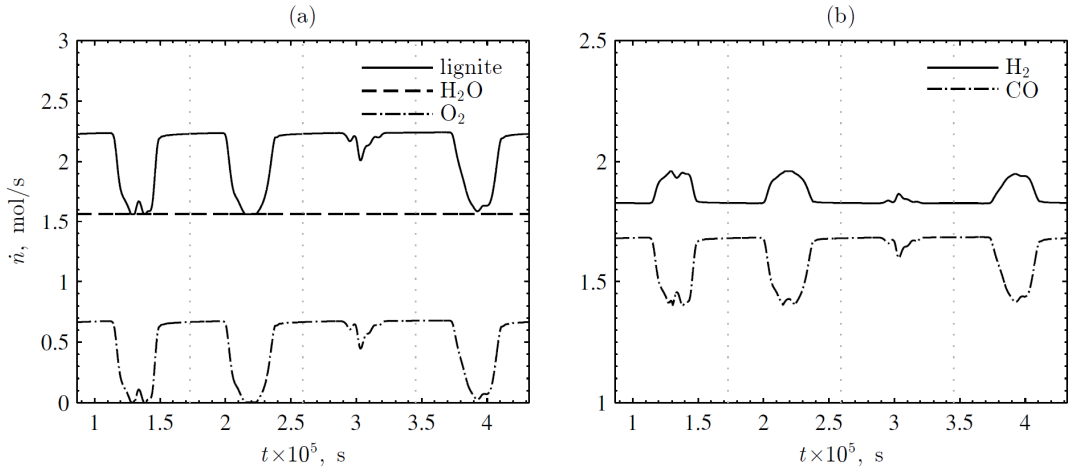

Figure 2.11 Molar flows as functions of time for (a) reactants of lignite (solid), H_2O (dashed), and O_2 (dot-dashed) and (b) products of H_2 (solid) and CO (dot-dashed) for a minimum temperature set point of 1100 K.

The input and output flows for four days of operation at 1100 K are shown in Figure 2.11. The inlet flows were specified to maintain a combined ~3.5 mol/s of H_2 plus CO output at the 1100 K setpoint with the additional objective of maximizing the yield of H_2 and CO while minimizing the production of CO_2. The amount of H_2O fed into the reactor remained constant at 1.56 mol/s. During autothermal operation (*e.g.*, nighttime operation), the amount of lignite coal and O_2 introduced into the reactor remained constant and about 30% of the carbonaceous feedstock was combusted to provide heat to maintain the setpoint temperature. As the I_{DN} rose to peak levels, the flows of lignite coal and O_2 were reduced as more of the feedstock was directly converted to syngas via solar allothermal gasification. An equimolar mixture of H_2O and lignite coal was used during solar operation. Operating at the 1100 K setpoint always produced a syngas mixture that contained more H_2 than CO. The H_2:CO ratios increased slightly during solar operation, desirable for F-T synthesis. The typical H_2:CO ratio for F-T synthesis is 1.7 for iron-

based catalysts and 2.15 for cobalt-based catalysts [4]. These ratios are moving targets and have some flexibility during transient operation [5]. The H_2:CO ratio of the products can be made suitable for F-T synthesis in a downstream water-gas shift reactor, which can shift the products more efficiently and at lower temperatures than the solar reactor [5]. However, the modeling of such an integrated system is outside the scope of this analysis.

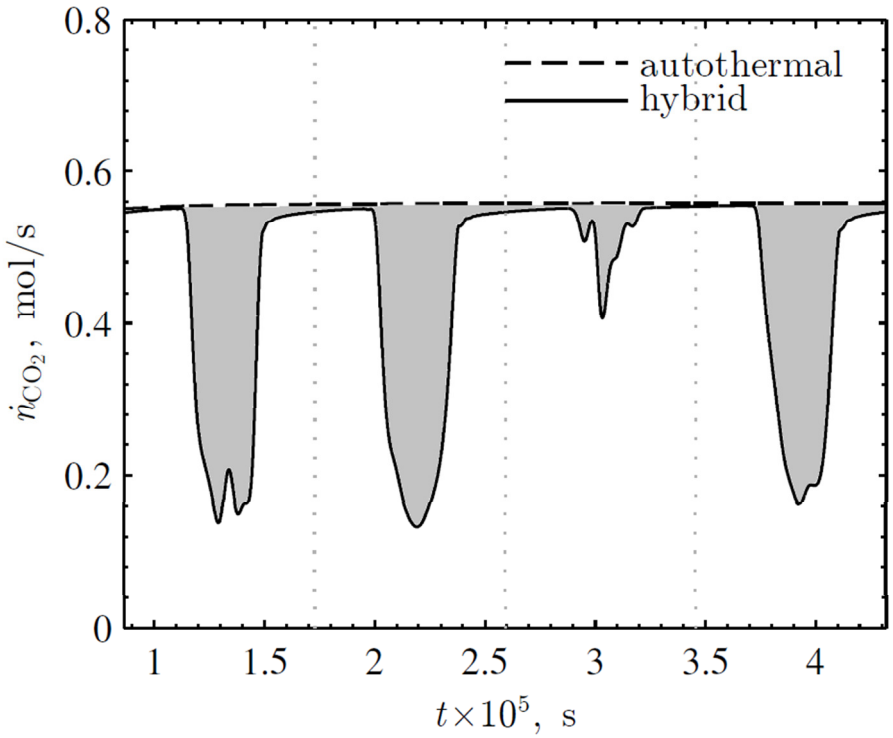

Figure 2.12 Molar flow of CO_2 produced as a function of time at an 1100 K set point for the autothermal (dashed) and hybrid (solid) cases with the shaded areas representing mitigated CO_2 emissions via the chemical storage of concentrated solar irradiation.

The model was run in an autothermal-only mode at the 1100 K setpoint with I_{DN} set to zero at all times to compare reactor performance and outputs from hybrid solar/autothermal operation. CO_2 produced due to partial feedstock combustion and

incomplete conversion is shown in Figure 2.12 for the autothermal-only mode and the hybrid solar/autothermal mode. CO_2 emissions were significantly reduced during the day when I_{DN} was high compared with autothermal-only operation. The shaded areas represent mitigated CO_2 emissions due to concentrated solar irradiation during the day. Numerical integration across the four days shown revealed a reduction in CO_2 emissions by 19% in the hybrid case as compared to the autothermal baseline case. During periods of high I_{DN}, CO_2 emissions were reduced by over 33% per day. Though the higher setpoint temperature required more O_2 for process heat, the favored reverse water-gas shift reaction caused the overall CO_2 emissions to be lower in the autothermal mode. This high-temperature effect is shown in Figure 2.1b.

The cold gas ratio is used to describe ratio of the energy in the products compared to the reactants based on LHV, represented as:

$$R = \frac{\dot{n}_{CO} LHV_{CO} + \dot{n}_{H_2} LHV_{H_2}}{\dot{n}_{feedstock} LHV_{feedstock}} \tag{2.13}$$

where $\dot{n}$ is the molar flow rate. During the autothermal mode, R describes the efficiency of converting the feedstock to syngas (*i.e.*, the cold gas efficiency). Model cold gas efficiency was 87%.

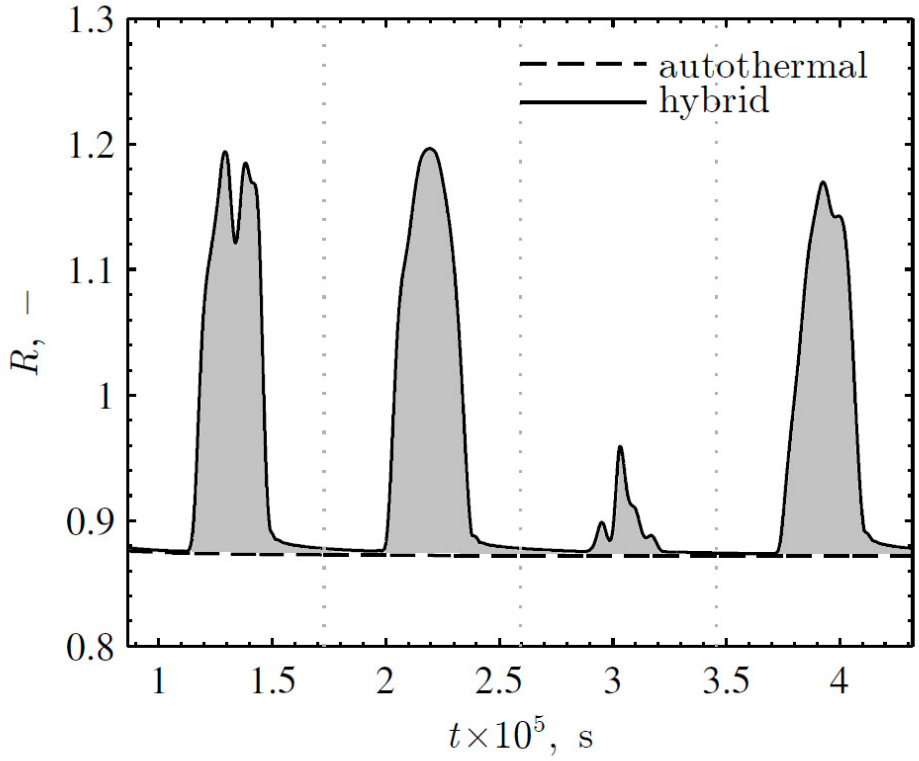

Figure 2.13 Cold gas ratio as a function of time for the 1100 K set point for the autothermal (dashed) and hybrid (solid) cases with shaded areas representing stored concentrated solar irradiation.

R is plotted as a function of time in Figure 13. The shape of *R* closely followed I_{DN}, indicating a direct correlation between process efficiency and available I_{DN}. At peak levels of I_{DN}, the cold gas ratio reached values of up to 1.2. This represents a 20% increase in the LHV of the product gases over the feedstock via the chemical storage of I_{DN}. The average cold gas ratio for the four days shown in Figure 2.9 was 0.946. The average cold gas ratio was over 1 during days with the highest I_{DN}. In addition, the fuel was converted into a more transportable form that can be used to drive a wider range of more efficient applications.

During solar operation, the solar-to-fuel efficiency is represented as:

$$\eta_{\text{solar-to-fuel}} = \frac{\dot{n}_{\text{CO}} LHV_{\text{CO}} + \dot{n}_{\text{H}_2} LHV_{\text{H}_2}}{\dot{Q}_{\text{solar}} + \dot{n}_{\text{feedstock}} LHV_{\text{feedstock}}} \tag{2.14}$$

where $\dot{Q}_{\text{solar}}$ is the amount of concentrated solar power entering through the aperture of the reactor. $\eta_{\text{solar-to-fuel}}$ describes how efficiently the solar energy is stored in the product gas based on the lower heating value of the fuels and the amount of available solar irradiation, which constantly changes. During times of peak I_{DN}, $\eta_{\text{solar-to-fuel}}$ was 39%, slightly higher than values reported in previous modeling and experimental campaigns using low-rank coals and waste materials in packed-bed solar gasification reactors [35, 38, 66]. Additional increases in $\eta_{\text{solar-to-fuel}}$ not considered in this analysis could be realized by using the sensible heat from the products to preheat the incoming reactants.

Separation of CO_2 from the product gases is required, and the minimum theoretical power is represented as:

$$\dot{W}_{\text{sep,CO}_2} = \dot{n}_{\text{CO}_2} R_{\text{u}} T_{\text{amb}} \ln\left(\frac{1}{y_{\text{CO}_2}}\right) + \dot{n}_{\text{syngas}} R_{\text{u}} T_{\text{amb}} \ln\left(\frac{1}{y_{\text{syngas}}}\right) \tag{2.15}$$

where R_{u} is the universal gas constant, T_{amb} is the ambient temperature (298.15 K), and y_i is the mole fraction of component i. $\dot{W}_{\text{sep}}$ can also be represented as a fraction of the total theoretical work that can be extracted from the products of the system:

$$F_{\dot{W}_{\text{sep,CO}_2}} = \frac{\dot{W}_{\text{sep,CO}_2}}{\dot{n}_{\text{CO}} \Delta G|_{\text{CO}+0.5\text{O}_2 \Rightarrow \text{CO}_2 @ T_{\text{amb}}} + \dot{n}_{\text{H}_2} \Delta G|_{\text{H}_2+0.5\text{O}_2 \Rightarrow \text{H}_2\text{O} @ T_{\text{amb}}}} \tag{2.16}$$

where ΔG is the change in molar Gibbs free energy for a given reaction at T_{amb} with the syngas products. $F_{\dot{W}_{\text{sep,CO}_2}}$ is plotted as a function of time in Figure 2.14 for both the

autothermal and hybrid cases. Although the power required to separate CO_2 was very small (<0.01) relative to the potential power output of the system, this is a minimum theoretical value over a maximum theoretical value and would be higher if losses were taken into account. A large $\dot{W}_{sep}$ negatively affects the overall process efficiency. The shaded area represents energy saved through the production of a cleaner syngas product during solar operation. On a day of high I_{DN}, energy required for CO_2 separation was reduced by over 27%.

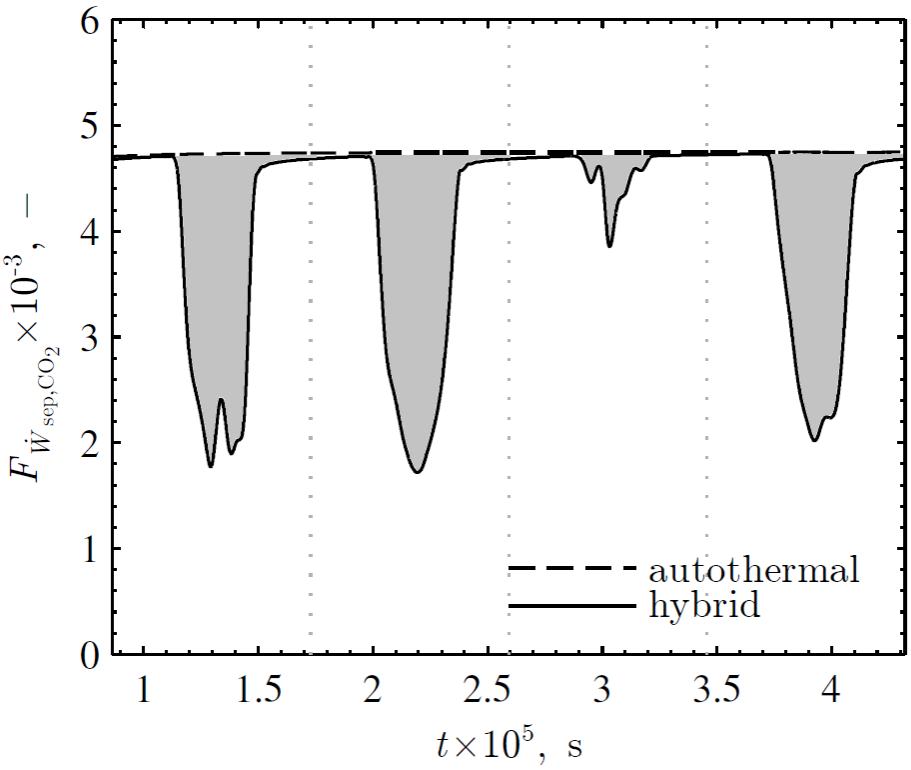

Figure 2.14 Minimum theoretical power of CO_2 separation from syngas as a fraction of the theoretical work from the syngas versus time at the 1100 K set point for the autothermal and hybrid cases. The shaded areas represent the minimum energy saved by producing cleaner syngas during solar operation.

The minimum theoretical power of separating O_2 from atmospheric air was calculated in a similar manner using N_2 and O_2, assuming an air composition of 79% N_2

and 21% O_2, respectively. In practice, power required to separate O_2 is several times higher. Cryogenic separation is the most common commercial-scale separation process and has an energy expense of 0.245 kWh/kg_{O_2} [23]. Solar-powered electrolysis is another possible method of producing pure streams of O_2, but it suffers from low efficiency, high cost [80], and requires a mechanism for storage as the O_2 is required during periods with little or no solar irradiation. Consistent with the analysis for CO_2 separation, $F_{\dot{W}_{sep,O_2}}$ is plotted as a function of time in Figure 2.15 for both the autothermal and hybrid cases. More O_2 used in the hybrid solar/autothermal reactor translated to more energy that would need to be expended to separate O_2 from air to drive the autothermal gasification processes. By using solar energy instead of combusting the feedstock with O_2, additional energy savings were achieved. The shaded area represents energy saved by reducing the O_2 fed into the system during solar operation. On a day of high I_{DN}, energy required for O_2 separation was reduced by over 45%.

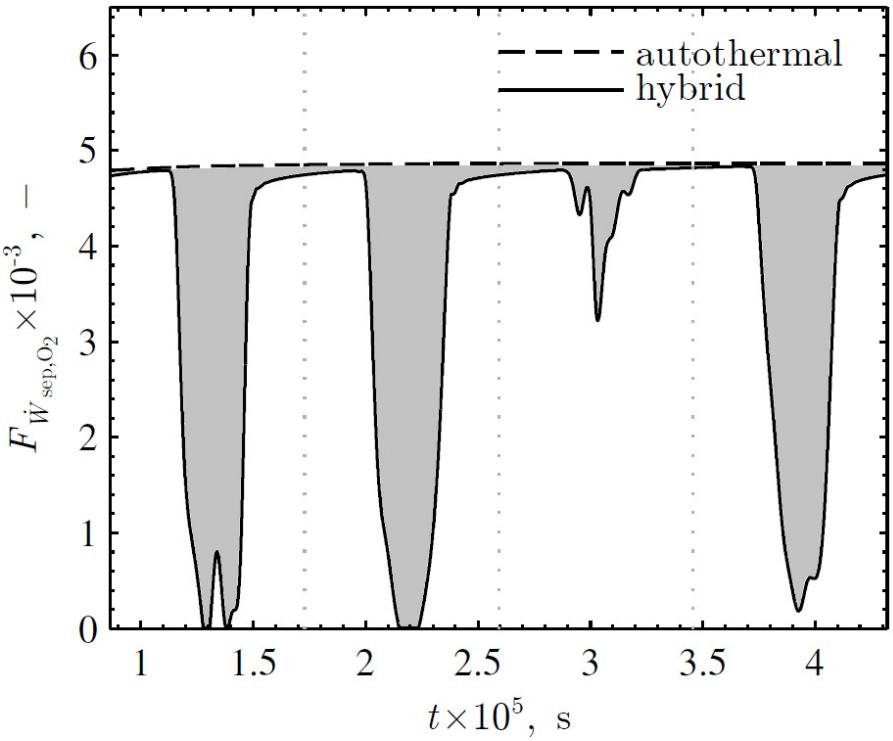

Figure 2.15 Minimum theoretical power of O_2 separation from atmospheric air as a fraction of theoretical work from the syngas versus time at the 1100 K set point for the autothermal and hybrid cases. The shaded areas represent the minimum energy saved by reducing the amount of O_2 used during solar operation.

Hybrid operation runs for four full days from each month of the year were tested and averaged into representative seasonal data. These data were again compared to the autothermal-only baseline case. Compiled results are shown in Table 2.2. As expected, optimal performance occurred during the summer months when I_{DN} was higher for longer periods of the day. Average cold gas ratio, $\bar{R}$, was found to be 0.958 during the summer months, with reductions in CO_2 emissions of 22.8% compared with the autothermal-only mode. Average reductions in separation work for CO_2 and O_2 in the hybrid mode were 18.16% and 30.2%, respectively. The winter months had the lowest improvement over the autothermal mode with $\bar{R}$ = 0.939. Reduction in CO_2 emissions was about 5% less

than that for summer, at 17.85%. For the winter months, average reductions in separation work for CO_2 and O_2 in the hybrid mode were 14.25% and 23.52%, respectively. Spring and fall months showed intermediate improvements over the autothermal-only mode. There were clear benefits to running a hybrid process at all times of the year, though the summer months have greatest solar resources and thus the greatest potential for reduced carbon intensities.

Table 2.2 Averaged modeling results reported during different seasons for the hybrid mode compared with the autothermal mode.

Season	$\overline{I_{DN}}$ (W/m^2)	$\bar{R}$ (-)	Reduction in CO_2 emissions (%)	Reduction in W_{sep} of CO_2 (%)	Reduction in W_{sep} of O_2 (%)
"Spring" (months 3-5)	266	0.945	20.46	16.55	26.52
"Summer" (months 6-8)	314	0.958	22.80	18.16	30.20
"Fall" (months 9-11)	247	0.941	19.33	15.60	25.14
"Winter" (months 12-2)	237	0.939	17.85	14.25	23.52

2.7 Summary

The goals of dynamically modeling an integrated solar and autothermal gasification process for continuous, quasi-stable syngas production in a simplified reactor concept and designing a stable temperature controller for the system were realized. The closed-loop controller was able to achieve performance with low frequency error within 1% and high frequency error within 200% of the commanded change in set point temperature and a bandwidth of 0.008 rad/s. Combining the high-fidelity model with the proposed temperature controller, simulation results showed that the temperature control error was less than 3.4 K (0.74% of nominal) for a five-day simulation with transient solar disturbances present. Using available concentrated solar irradiation yielded a number of

environmental and economic benefits for the gasification process. With lignite coal as the feedstock, cold gas ratios of 1.2 and solar-to-fuel efficiencies of 39% were achieved during complete solar operation, while a cold gas efficiency of 87% was maintained during autothermal operation. Solar operation was also determined to be advantageous in terms of reducing power required to separate reactant gases and product streams.

CHAPTER 3. KINETIC ANALYSES[2]

3.1 Introduction

The concept of a hybrid solar/autothermal gasification reactor was demonstrated using the ideal condition of chemical equilibrium; the next step was to evaluate kinetic rates of the relevant reactions. This chapter presents the kinetic analyses of gasification and combustion reactions for several carbonaceous feedstocks. Experimental procedures and methodology are presented, followed by the kinetic analyses with error calculations. Experiments were carried out using non-isothermal thermogravimetry and appropriate Langmuir-Hinshelwood-type mechanisms were used to fit rate constants. Several additional experimental conditions were run to examine the effects of particle size, heating rate, and total gas flow rate. SEM and BET analyses were performed to examine particle characteristics. The results of the kinetic analyses are summarized.

3.2 Relevant Literature

Chemical kinetics for combustion and gasification of carbonaceous materials, particularly coal, are well-studied, but remain a somewhat contested area due to the complexity of the elementary reactions. There are inherent limitations in the experimental apparatuses for the determination of rate constants that must be acknowledged. TGAs are commonly-used instruments that allow for the conversion of a solid to be temporally monitored under specified temperature and gas partial pressure conditions. Woodruff and Weimer [82] developed a novel technique for measuring high-temperature gasification kinetics

[2] Work from this chapter is published in [81]

and outlined some of the challenges associated with thermogravimetric analysis. Williams [83] noted some of the difficulties as well. These include time scale of analysis, heat and mass transfer limitations, diffusional effects, accurate temperature measurement, limited heating rate, and cost of the instrument. However, the goal of the present study was not to redefine the methodologies for kinetic analysis. For this reason, the standard practice of thermogravimetric analysis was performed with the aim of developing applicable reaction rate equations for the design of a hybrid solar/autothermal gasification reactor.

Detailed knowledge of reaction kinetics is a prerequisite for comparing different carbonaceous feedstocks and guiding the thermochemical reactor design process for specific residence times, temperature ranges, etc. Previous studies have developed kinetic models to describe H_2O, CO_2, and combined H_2O-CO_2 gasification at near-atmospheric pressures and form the basis for the present kinetic analysis. One popular model is the oxygen-exchange mechanism, which captures the adsorption and desorption of oxygen complexes on carbon surfaces. Early studies by Gadsby *et al.* [84, 85], Walker *et al.* [86], Ergun [87], and Laurendeau [88] investigated the kinetics of CO_2- and H_2O-C gasification reactions and developed adsorption/desorption-based mechanisms. A more recent review by Di Blasi [89] compiled the results of lignocellulosic char gasification and combustion studies, with the majority considering a global model. Müller *et al*. [90] investigated the kinetics of charcoal gasification under direct high-flux irradiation, and determined rate constants for both a complex, multi-step sorption model as well as a simplified mechanism and found both to match the experimentally-measured data relatively well. Trommer *et al.* examined the gasification kinetics of petroleum coke

using thermogravimetry [27] and a directly-irradiated fluidized bed [28] and fit kinetic parameters for Langmuir-Hinshelwood-type rate laws. Kruesi *et al.* [23] determined kinetic parameters for sugarcane bagasse gasification using a similar mechanism and thermogravimetric measurements. Isoconversional methods offer another possibility for obtaining kinetic parameters, but model-fitting is considered a better approach when the mechanism is known [91].

Other authors have extended the oxygen-exchange mechanism to include more reaction steps that involve OH radical and H atom groups. This more detailed model assumes that H_2O undergoes dissociation at the carbon surface and the radicals participate in reactions at the carbon surface. Variations of this model have been employed in gasification kinetic studies by Roberts and Harris [92], Trommer and Steinfeld [27], Müller *et al.* [90], Hüttinger and Merdes [93], van Heek *et al.* [94], Mühlen *et al.* [95], and Blackwood and Ingeme [96] that have generally been performed at elevated pressures (>1 bar). These more complex mechanisms may capture reaction kinetics more accurately at higher pressures when inhibition is significant. In associative or dissociative adsorption, H_2 or H may be interacting with the C surface, respectively. The subsequent combination of H atoms may be slow enough to inhibit the overall reaction. The level of complexity in Langmuir-Hinshelwood-type mechanisms required to capture gasification reaction rates, particularly at higher pressures, is still the subject of some debate [92].

Oxidation reactions between C and O_2 (*i.e.*, combustion) are significant in autothermal gasification and must also be considered for the system. Reactions between carbonaceous solids and O_2 are well-studied. However, there is little consensus among

researchers regarding the kinetic parameters or proper rate expression [88, 97]. The majority of studies use a global power rate law or two-step Langmuir-Hinshelwood rate law to describe oxidation of coal or biomass chars. Laurendeau [88] provided a comprehensive review of earlier investigations into the C/O_2 reaction mechanism. Hecker *et al.* [98] analyzed the rates of high-pressure coal char oxidation using thermogravimetry and an n^{th}-order rate law. Hong *et al.* [99] modeled high-pressure char oxidation using a Langmuir-Hinshelwood model modified with an effectiveness factor for pore diffusion effects. Hurt and Haynes [97] attempted to reconcile the inconsistent n^{th}-order behavior of power-law kinetics with simple Langmuir-Hinshelwood models, offering surface heterogeneity as a possible explanation. Murphy and Shaddix [100] proposed combining these two models into an n^{th}-order Langmuir-Hinshelwood equation. Zhuang *et al.* [101], Hurt and Calo [102], and Niksa *et al.* [103] have proposed a three-step model to account for reactions between gas phase oxygen and surface complexes. While good fits are possible using the global power rate law in a certain temperature range, it fails to mechanistically capture the events of adsorption and desorption on homogeneous surfaces.

All of the aforementioned studies used chars, cokes, or graphite due to the high temperatures (>1073 K) that must be reached before gasification occurs. Heating feedstock particles in an inert atmosphere devolatilizes them through pyrolysis, leaving mostly fixed carbon. Prior work notes the lack of interchangeability between slow and fast pyrolysis kinetics for woody biomass [83, 104]. Moreover, pyrolysis affects subsequent gasification kinetics of the feedstock; high heating rates (10-300 K/s) for fast pyrolysis have been shown to increase char reactivity [89, 105]. A review by Yaman

[106] noted the association between lower heating rate and higher char and gas product yields. Pyrolysis rates are generally faster than char oxidation rates, which are faster than char gasification rates; the throughput of a hybrid solar/autothermal gasification process is likely to be limited primarily by gasification rates [89]. Due to the limited heating rates of available experimental equipment, a separate, conventional slow pyrolysis pretreatment of feedstocks is assumed for the present work. This ensures that pyrolysis oils are extracted prior to gasification, leaving a more homogeneous feedstock with high fixed carbon content, which is desirable for process controllability.

3.3 Experimental Section

3.3.1 Feedstock Samples and Preparation

The raw carbonaceous feedstocks examined in this work were laboratory-grade activated charcoal (Sigma-Aldrich, untreated powder derived from wood, 100-400 mesh, used as a control), Illinois #6 bituminous coal (100-170 mesh), and *miscanthus x giganteus* (miscanthus, 60-80 mesh). Photos of these feedstocks are shown in Figure 3.1. Miscanthus is a rhizomatous perennial grass that has been investigated as an energy crop due to its high biomass yield and high nitrogen and water-use efficiencies [107-110]. Solar gasification is able to utilize a wide range of carbonaceous feedstocks; experimentation allowed for the testing of two biomass samples and one fossil fuel sample. The use of a novel biomass grown on agriculturally marginal land has implications for areas where solar resources are abundant.

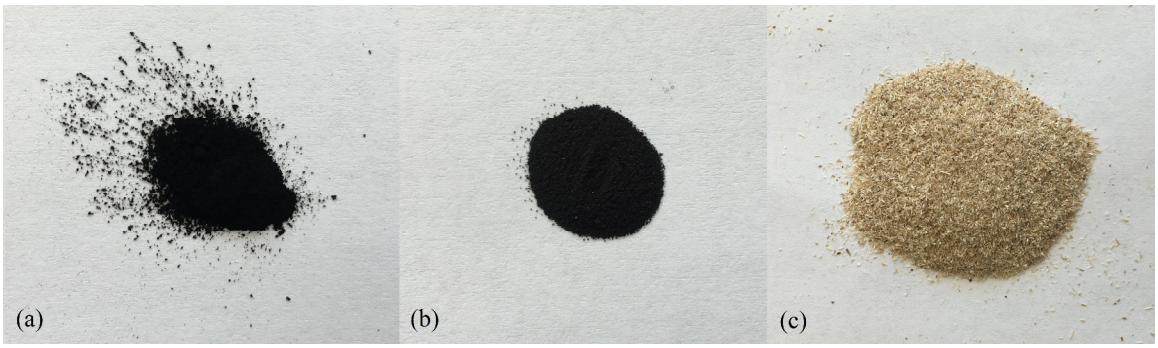

Figure 3.1 Photos of the (a) activated charcoal (100-400 mesh), (b) Illinois #6 bituminous coal (100-170 mesh), and (c) miscanthus (60-80 mesh).

Feedstock chars were used in all thermogravimetric experiments either by *in-situ* pyrolysis during gasification run heat-up or through pre-pyrolysis for combustion runs. The activated charcoal was supplied as a char. Prior to experimentation, coal and miscanthus samples were dried. Due to high mass loss during devolatilization, miscanthus was pre-pyrolyzed for both combustion and gasification in a N_2-purged split tube furnace (Thermcraft) at 10 K/min to a final temperature of 773 K based on literature and preliminary TGA experiments [111, 112]. Bituminous coal samples were pre-pyrolyzed for combustion experiments at 10 K/min to a final temperature of 773 K under an Ar flow in the TGA, described in more detail in an upcoming section. Photos of the bituminous coal char and miscanthus char are shown in Figure 3.2.

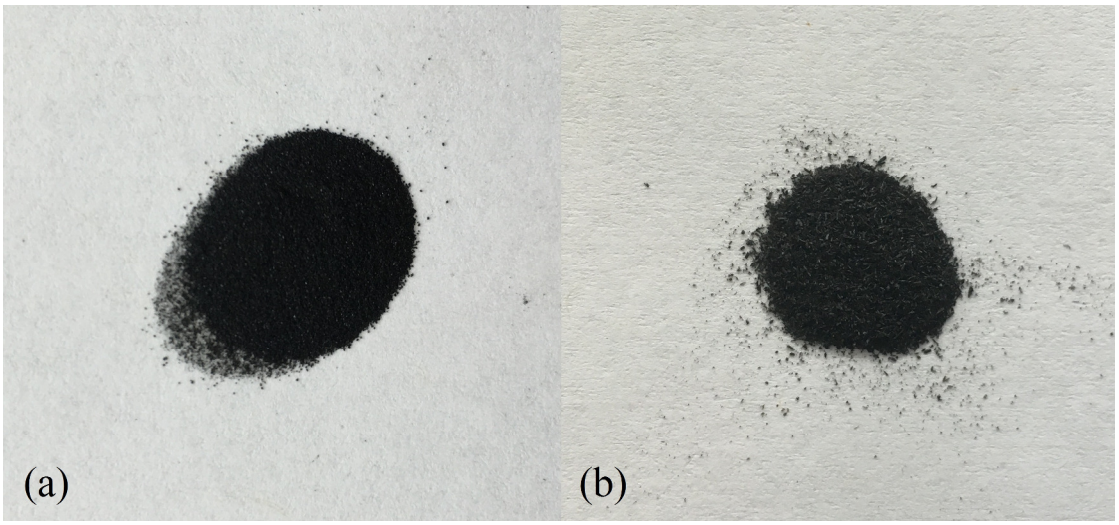

Figure 3.2 Photos of the (a) bituminous coal char and (b) miscanthus char.

Results from proximate and ultimate analyses for the feedstocks are provided in Table 3.1. A clear tradeoff was evident between carbon content and volatile matter; reactivity for both combustion and gasification generally increases with volatile matter [113]. This applies to pyrolyzed feedstocks as well, potentially due to volatile content affecting char porosity, and some O and H remaining in the char [113, 114]. Activated charcoal has the highest carbon content, followed by bituminous coal, then miscanthus. Miscanthus has the highest amount of volatile matter, followed by bituminous coal, then activated charcoal. Miscanthus and activated charcoal have low amounts of ash, but bituminous coal contains almost 10% ash by weight. Bituminous coal also contains the most N and S, resulting in potential NO_x and SO_x production.

Table 3.1 Proximate and ultimate analyses of feedstocks (values in weight % unless otherwise noted).

	Activated charcoal	Bituminous coal	Miscanthus
Carbon	73.34	63.75	45.28
Hydrogen	3.50	4.50	6.04
Nitrogen	0.12	1.25	0.33
Oxygen (BD)	21.33	6.88	45.82
Sulfur	<0.01	2.51	0.06
Ash	1.71	9.70	2.47
Moisture	7.12	11.12	5.51
Volatile matter	17.71	34.99	74.32
Fixed carbon	73.46	44.19	17.70
H/C [mol/mol]	0.569	0.841	1.589
O/C [mol/mol]	0.218	0.081	0.760

3.3.2 Experimental Procedures

Experimentation was performed in a TGA (Netzsch, STA449 F3 Jupiter, ± 1 µg) equipped with a furnace suitable for atmospheres containing up to 100% H_2O(v) (T_{max} = 1523 K). A schematic of the TGA furnace is shown in Figure 3.3. Powder carbonaceous feedstock samples were placed on a 17-mm-diameter Al_2O_3 crucible, which was in contact with an S-type thermocouple. Spreading the samples in thin layers on the crucible minimized heat transfer limitations. The initial and final sample masses were measured using an analytical balance (Mettler-Toledo, ML54, ± 0.1 mg). Blank runs were subtracted from sample runs to mitigate buoyancy and momentum effects due to changing temperatures. A 100 mL_N/min (L_N denotes liters at normal conditions at 273 K and 1 bar) flow of Ar that did not reach the sample was used to protect the balance, and a downward reacting gas flow allowed reacting gases to impinge directly on the sample. A similar experimental setup was used in previous work [27, 115].

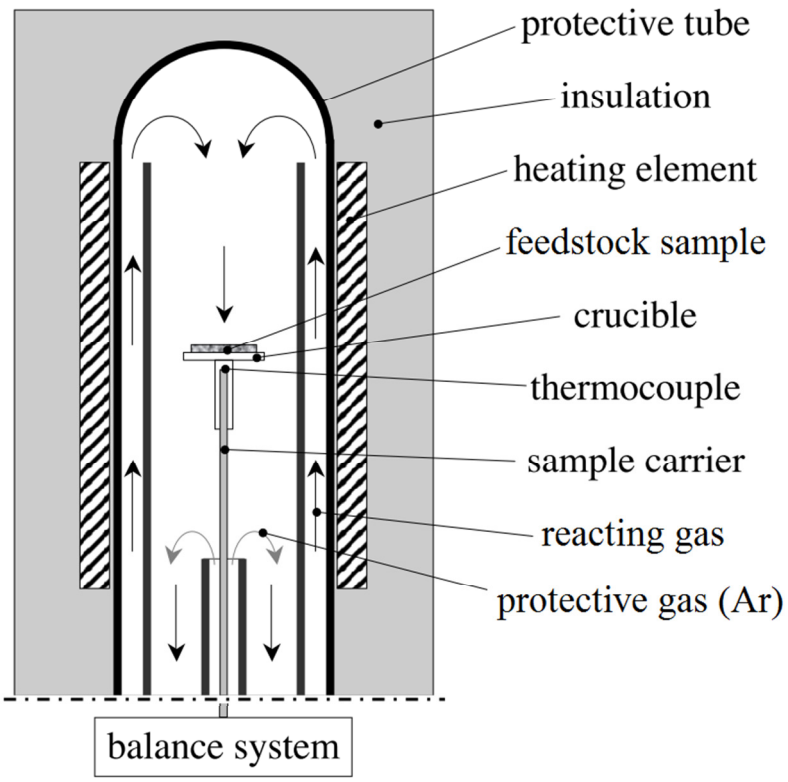

Figure 3.3 Schematic of the TGA furnace, adapted from [116].

3.3.2.1 Gasification

Gasification experiments were performed using non-isothermal thermogravimetry. Sample sizes of ~30, ~20, and ~10 mg were used for bituminous coal, activated charcoal, and miscanthus char, respectively. A larger sample of bituminous coal was used due to the higher amount of volatiles released during pyrolysis, leaving ~66% of the initial mass in char prior to gasification. Very low particle densities for miscanthus char prevented the reliable use of larger samples. Previous studies have varied sample masses across samples due to differing particle characteristics [37, 117]. The furnace was evacuated and purged with Ar prior to each experiment, and samples were subsequently heated at a rate of 10 K/min in an Ar atmosphere to remove volatiles from the samples via pyrolysis as

they approached favorable temperatures for gasification reactions (>1073 K). Although CO_2 is not an input for steam gasification, it is produced in combustion reactions related to autothermal processes and the water-gas shift reaction and can subsequently react with feedstock particles. For this reason, gasification runs used H_2O balanced in CO_2. As the samples reached sufficiently-high temperatures, a water vapor generator (Bronkhorst, LIQUIFLOW) supplied between 20-100% $H_2O(v)$ balanced in CO_2 at 130 mL_N/min. A transfer line at 423 K prevented $H_2O(v)$ condensation before it reached the TGA, using similar conditions to previous work [118]. CO_2 flow rate was controlled using mechanical flow controllers (Aalborg, P-Meter).

The measured temporal mass loss from thermogravimetry for miscanthus char gasification is shown in Figure 3.4. The sample was heated at a rate of 10 K/min in 100% Ar (the shaded area), during which moisture and volatiles were driven off of the sample via pyrolysis, resulting in a ~20% mass loss. At 1093 K, a mixture of 80% H_2O-CO_2 was introduced to the sample, resulting in gasification reactions. These reactions proceeded until ~9% of the sample remained as ash. This was higher than the ash content reported in Table 3.1 due to pyrolysis prior to thermogravimetry, which removed volatiles and increased the relative amount of ash in the char.

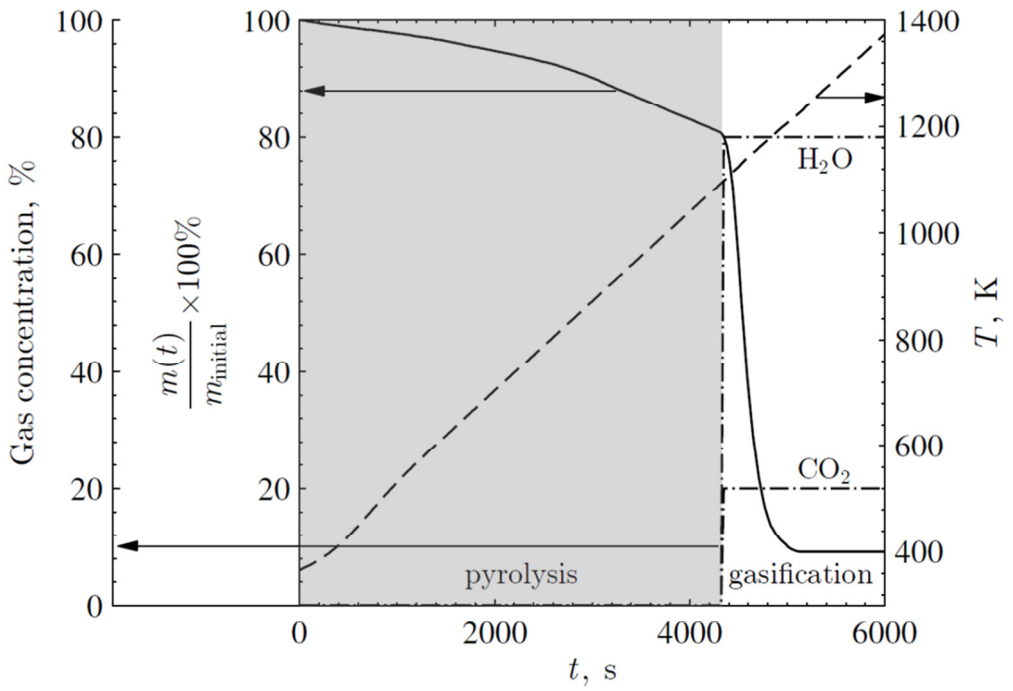

Figure 3.4 Temporal percent mass change (solid) and temperature (dashed) measured during non-isothermal gasification of miscanthus char initially heated in 100% Ar and then heated in 80% H_2O–CO_2 (dot-dashed) at 10 K/min.

3.3.2.2 Combustion

Combustion experiments were performed using non-isothermal thermogravimetry, as preliminary isothermal thermogravimetry was found to be unreliable; temperatures of interest were characterized by conversions that were too rapid to have confidence about gas concentrations at the sample (<1 min). Bituminous coal samples were pre-pyrolyzed for combustion experiments at 10 K/min to a final temperature of 773 K under an Ar flow in the TGA. Samples sizes of ~20, ~20, and ~2 mg were used for bituminous coal char, activated charcoal, and miscanthus char, respectively. Due to the high reactivity of miscanthus char, very small samples were necessary to prevent thermal runaway. The furnace was evacuated and purged with Ar prior to each experiment. Samples were then

heated at a rate of 20 K/min under a constant oxidizing flow of 130 mL_N/min until fully combusted. Although heating rates of up to 50 K/min were possible with the instrument, 20 K/min was chosen as the maximum to avoid significant heat transfer limitations. Other combustion studies employing non-isothermal thermogravimetry have used heating rates of up to 40 K/min [119, 120]. O_2 and Ar flow rates were controlled using a mechanical flow controller (Aalborg, P-Meter). Due to the low O_2 concentrations expected during autothermal gasification, the O_2 concentration was varied between 10-40% O_2-Ar.

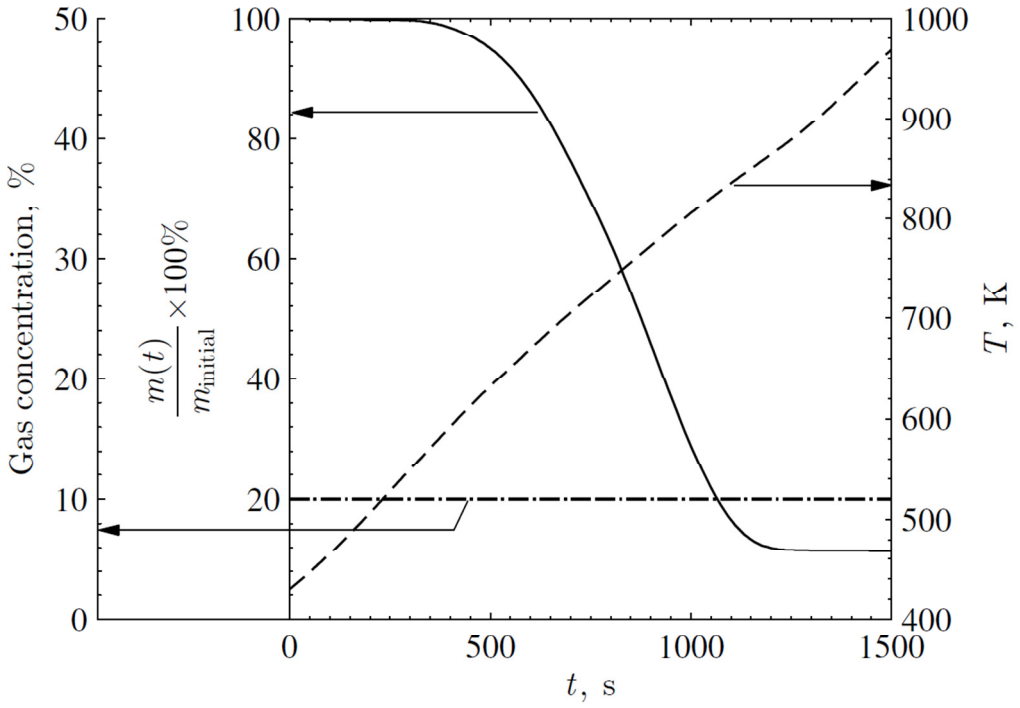

Figure 3.5 Temporal percent mass change (solid) and temperature (dashed) measured during non-isothermal combustion for bituminous coal char heated in 10% O_2–Ar (dot-dashed) at 20 K/min.

The measured temporal mass loss for bituminous coal char combustion is shown in Figure 3.5. Very little mass loss occurred before the temperature reached ~600 K. As

the temperature continued to increase, a rapid mass loss was seen until the sample was completely combusted by ~870 K with ~11.4% of the sample mass remaining as ash.

3.4 Kinetic Analyses

The temporal conversion was determined from the mass loss as:

$$\alpha(t) = \frac{m_{\text{initial}} - m(t)}{m_{\text{initial}} - m_{\text{final}}} \tag{3.1}$$

where t is time; $m(t)$ is temporal sample mass measured by TGA; m_{initial} is sample mass at the start of gasification or combustion; and m_{final} is final mass. The differential rate was expressed with a first-order reaction model, which accounts for a changing particle surface area as conversion progresses without specific knowledge of the initial effective surface area per mole, represented as:

$$r = \frac{1}{1-\alpha}\frac{d\alpha}{dt} \tag{3.2}$$

The oxygen-exchange mechanism for H_2O-CO_2 gasification consisting of three reactions was used to represent reversible adsorption/desorption of oxygen complexes. The adsorption/desorption of H_2O/H_2 and CO_2/CO on active carbon surfaces are represented, respectively, as:

$$H_2O + C\langle * \rangle \underset{k_{-1}}{\overset{k_1}{\longleftrightarrow}} H_2 + C\langle O \rangle \tag{3.3}$$

$$CO_2 + C\langle * \rangle \underset{k_{-2}}{\overset{k_2}{\longleftrightarrow}} CO + C\langle O \rangle \tag{3.4}$$

The unidirectional desorption reaction of C and O to form CO is represented as:

$$C\langle O\rangle \xrightarrow{k_3} CO \tag{3.5}$$

The resulting rate laws for formation and consumption of H_2O, CO_2, H_2, and CO are expressed in terms of the fraction of the sites covered with adsorbed O, θ_O, and fraction of vacant sites, $(1 - \theta_O)$:

$$r_{H_2O} = k_{-1} p_{H_2} \theta_O - k_1 p_{H_2O} (1 - \theta_O) \tag{3.6}$$

$$r_{CO_2} = k_{-2} p_{CO} \theta_O - k_2 p_{CO_2} (1 - \theta_O) \tag{3.7}$$

$$r_{H_2} = k_1 p_{H_2O} (1 - \theta_O) - k_{-1} p_{H_2} \theta_O \tag{3.8}$$

$$r_{CO} = k_2 p_{CO_2} (1 - \theta_O) - (k_{-2} p_{CO} - k_3) \theta_O \tag{3.9}$$

Assuming sorption equilibrium gives:

$$\frac{d\theta_O}{dt} = r_{H_2O} + r_{CO_2} + k_3 \theta_O = 0 \tag{3.10}$$

In the TGA setup, gas flow was high enough that gaseous products were rapidly removed from the reaction site, making back reactions negligible for Equations 3.3 and 3.4. Substituting Equations 3.6 and 3.7 into the above equation gives:

$$\theta_O = \frac{k_1 p_{H_2O} + k_2 p_{CO_2}}{k_1 p_{H_2O} + k_2 p_{CO_2} + k_3} \tag{3.11}$$

resulting in a rate of C consumption due to gasification represented as:

$$r_g = r_{CO} + r_{CO_2} = k_3\theta_O = \frac{k_1 p_{H_2O} + k_2 p_{CO_2}}{1 + \frac{1}{k_3}\left(k_1 p_{H_2O} + k_2 p_{CO_2}\right)} \tag{3.12}$$

where p is the partial pressure of the given component normalized by 1 bar. k is the rate constant, assumed to have an Arrhenius-type temperature dependency, represented as:

$$k_i = k_{0,i} \exp\left(-\frac{E_{a,i}}{R_u T}\right) \tag{3.13}$$

where k_0 is the pre-exponential factor; E_A is the apparent activation energy; R_u is the universal gas constant; and T is the temperature.

The Langmuir-Hinshelwood-type rate expression for combustion was developed in a similar way. The mechanism was reduced to the two reaction steps that capture the adsorption and desorption of oxygen on carbon surfaces represented, respectively, as:

$$2C\langle * \rangle + O_2 \xrightarrow{k_4} 2C\langle O \rangle \tag{3.14}$$

$$C\langle O \rangle \xrightarrow{k_5} CO \tag{3.15}$$

Again assuming sorption equilibrium gives θ_O as:

$$\theta_O = \frac{k_4 p_{O_2}}{k_4 p_{O_2} + k_5} \tag{3.16}$$

The rate of C consumption due to combustion is represented as:

$$r_c = k_5\theta_O = \frac{k_4 k_5 p_{O_2}}{k_4 p_{O_2} + k_5} \tag{3.17}$$

Weighted non-linear regression [121] was used to fit α to the respective rate expressions using the least squares criterion for best fit. Chi-squared was minimized using a multidimensional constrained non-linear minimization algorithm [61] (Nelder-Mead), represented generically as:

$$\chi^2_{\min} = \sum_j \left(\frac{F_j}{\sigma_j} \right)^2 \tag{3.18}$$

where F is a function of measured properties and values that are initially unknown, represented as:

$$F_j = f\left(q_{1j}, ..., q_{nj}; \beta_1, ..., \beta_\rho\right) = 0 \tag{3.19}$$

where q denotes n measurands assumed as known, and β represents ρ fitting parameters assumed initially as unknown. The standard error was estimated as:

$$\sigma_j^2 = \sum_{i=1}^{n} \left(\frac{\partial F_j}{\partial q_{ij}} \right)^2 \sigma_{ij}^2 \tag{3.20}$$

where σ_{ij} represents the experimental uncertainty of the parameter. In this way, pre-exponential factors and activation energies were directly determined. Ninety-five percent confidence limits for the β's were estimated using chi-squared boundaries as described in

literature [122]. This was determined to be a better measure for evaluating goodness of fit, as R^2 has been shown to be an unreliable measure for nonlinear models [123].

3.5 Results and Discussion

The results of the kinetic analyses for combustion and gasification of the feedstocks are described in this section.

3.5.1 Gasification

Figure 3.6 shows the experimental and fitted α_g's for (a) activated charcoal, (b) bituminous coal char, and (c) miscanthus char gasification in reacting gas concentrations of 20-100% H_2O-CO_2. α_g was evaluated between ~1140-1270 K for activated charcoal, ~1150-1260 K for bituminous coal char, and ~1120-1180 K for miscanthus char with a heating rate of 10 K/min. The t required for complete α_g was relatively independent of reactant concentration. Complete α_g occurred in ~1000, ~800, and ~500 s for activated charcoal, bituminous coal char, and miscanthus char, respectively. Good agreement between experimental and fitted α_g's was seen. r_g decelerated with increasing α_g in agreement with the first order mechanism. α_g for activated charcoal showed a weak dependence on gas concentration with higher concentrations of H_2O(v) leading to more rapid α_g. A similar trend was observed for bituminous coal char with α_g showing a stronger dependence on H_2O-CO_2. Miscanthus char showed the opposite trend with lower concentrations of H_2O and higher corresponding concentrations of CO_2 leading to slightly higher rates of conversion. This is possibly due to a complex interaction between the catalytic ash effects and the reacting gasses. Alkali metals such as K and Na are known to have catalytic effects on char gasification reactions [124, 125]. SiO_2 has also

been shown to partially deactivate the catalytic activity of K, while CO_2 may suppress this deactivation [124]. Miscanthus ash has been shown to contain relatively large amounts of both K_2O and SiO_2 [110], indicative of indigenous metal content within the fuel that may affect rates. Other factors such as pore structure, carbon structure, and the possible preference of H_2O and CO_2 to react with different active sites may play a role as well [114, 126]. α_g for activated charcoal was slightly over-predicted for higher concentrations of H_2O-CO_2. α_g for bituminous coal char was slightly under-predicted for 40% H_2O-CO_2 and slightly over-predicted for 20% H_2O-CO_2. α_g for miscanthus char was marginally over-predicted upon approach to full α_g.

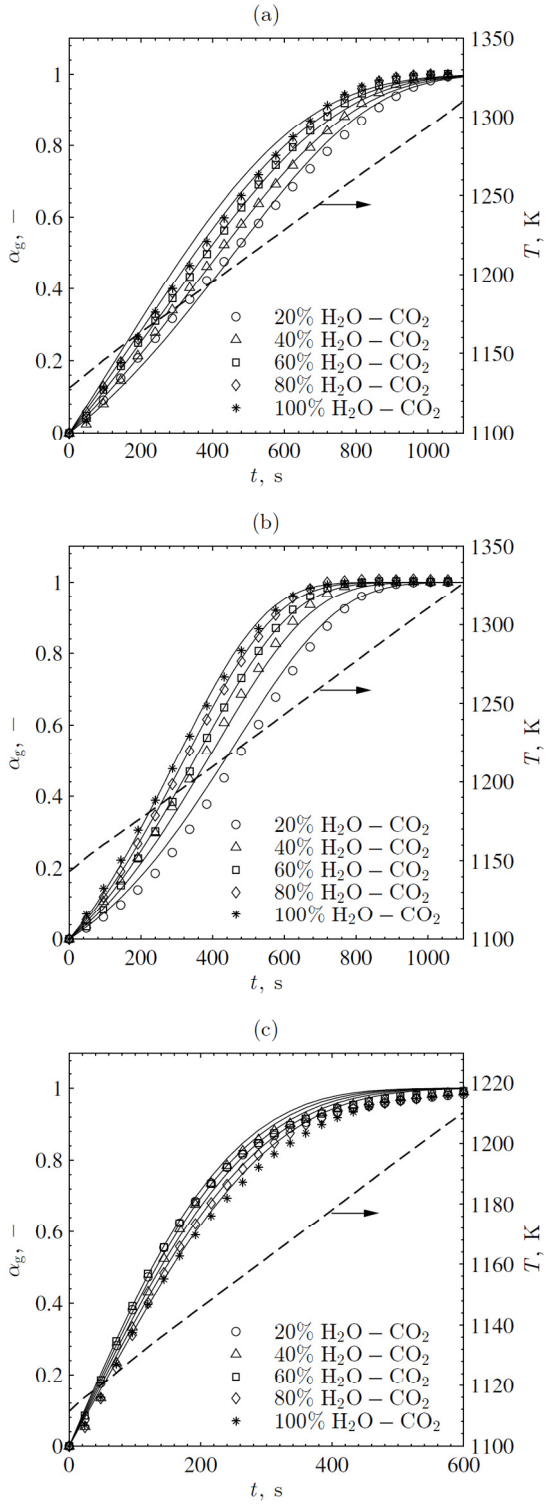

Figure 3.6 Experimental (markers) and fitted (solid) conversion for (a) activated charcoal, (b) bituminous coal char, and (c) miscanthus char gasification between 20 and 100% H_2O–CO_2 with the temporal temperature (dashed) increasing at 10 K/min.

Fitted results for k_0 and E_a for gasification reactions are shown with 95% confidence intervals in Table 3.2. E_a's for the forward reactions of Equations 3.3 and 3.4 are in agreement with values for carbonaceous feedstock gasification previously reported in literature [27, 85, 88, 89, 94, 127-130]. Desorption E_a's for the reaction in Equation 3.5 are not as well-reported in literature. In addition, the range is quite large for the reported values, varying between 120-421 kJ·mol^{-1} for lignocellulosic chars [89]. The k_3 parameters also have the largest 95% confidence limits shown in Table 3.2.

Table 3.2 Gasification kinetic parameters for the three carbonaceous feedstocks examined.

	Gasification	
	k_0 (s^{-1})	E_a (kJ·mol^{-1})
	Activated charcoal	
k_1 (s^{-1})	$2.80 \times 10^3 \pm 20.5$	135.4 ± 0.06
k_2 (s^{-1})	$2.66 \times 10^6 \pm 4.20 \times 10^4$	208.9 ± 0.13
k_3 (s^{-1})	$2.12 \times 10^8 \pm 2.57 \times 10^7$	205.1 ± 1.27
	Bituminous coal char	
k_1 (s^{-1})	$8.92 \times 10^9 \pm 6.54 \times 10^7$	281.6 ± 0.70
k_2 (s^{-1})	$3.25 \times 10^7 \pm 7.34 \times 10^5$	236.3 ± 0.22
k_3 (s^{-1})	$1.93 \times 10^9 \pm 4.26 \times 10^6$	192.5 ± 3.26
	Miscanthus char	
k_1 (s^{-1})	$1.04 \times 10^8 \pm 1.45 \times 10^6$	223.6 ± 0.10
k_2 (s^{-1})	$1.34 \times 10^8 \pm 1.69 \times 10^6$	204.6 ± 0.13
k_3 (s^{-1})	$1.11 \times 10^7 \pm 2.10 \times 10^6$	160.0 ± 1.63

3.5.2 Combustion

Figure 3.7 shows the experimental and fitted α_c's for (a) activated charcoal, (b) bituminous coal char, and (c) miscanthus char combustion in reacting gas concentrations of 10-40% O_2-Ar. α_c's were evaluated between ~610-960 K for activated charcoal, ~600-900 K for bituminous coal char, and ~610-770 K for miscanthus char with heating rates

of 20 K/min. r_c slowed very gradually towards the end of combustion for activated charcoal, possibly due to very small particles. Agreement between the fitted and experimental α_c's was very strong with r_c increasing with increasing O_2 concentration. As with gasification, combustion was more rapid for bituminous coal char than activated charcoal. Combustion was much more rapid for miscanthus char than the other two feedstocks; α_c was completed in about half of the time. As O_2 concentrations increased above 30%, virtually no change was observed in r_c for miscanthus char.

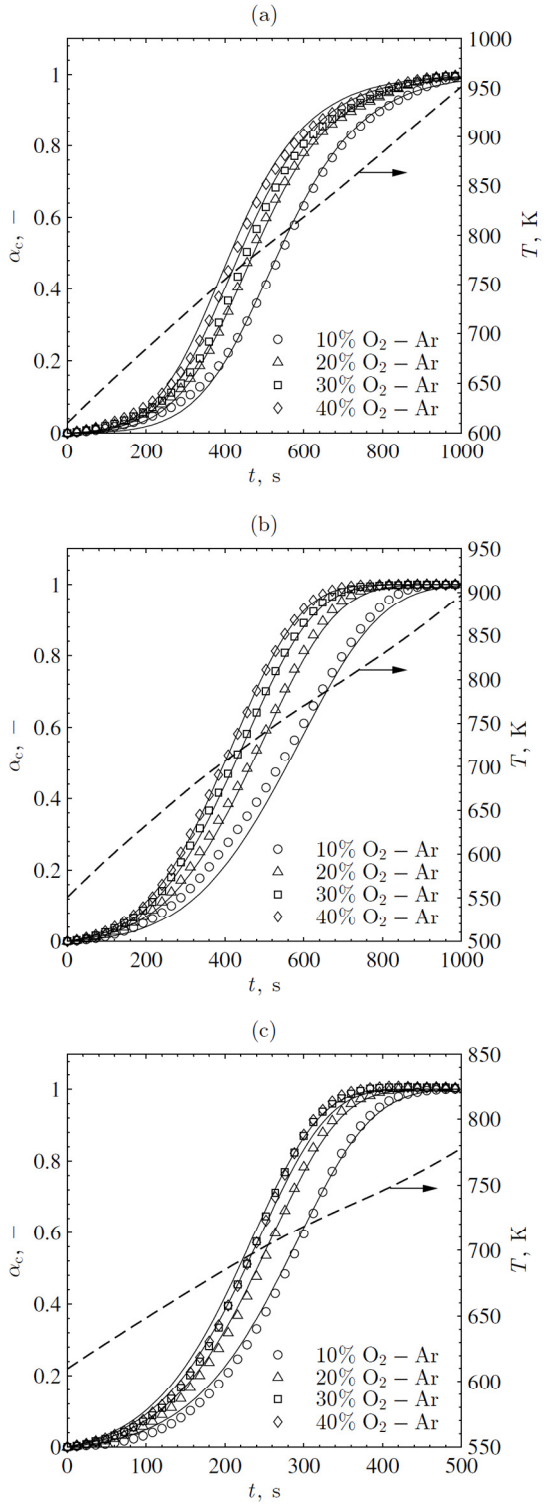

Figure 3.7 Experimental (markers) and fitted (solid) conversion for (a) activated charcoal, (b) bituminous coal char, and (c) miscanthus char combustion between 10 and 40% O_2–Ar with the temporal temperature (dashed) increasing at 20 K/min.

Results from combustion experiments indicated that changes in concentrations at the lower end of the range have the greatest impact on rate. This is significant for gasification, as the amounts of O_2 fed into the reactor are small compared to H_2O(v) and feedstock. The rate dependence of char combustion upon p_{O_2} as a result of possible adsorption control is described in literature [102]. Fitted results for combustion Arrhenius parameters for all feedstocks are shown with 95% confidence intervals in Table 3.3. $E_{a,5}$ for activated charcoal and associated error were fixed at zero, as preliminary results revealed negligible changes with temperature. Fitted E_a's for combustion cover a range of values around 100 kJ·mol^{-1}. A review of kinetic parameters for lignocellulosic char combustion has found values for activation energy to range from 76-229 kJ·mol^{-1} for a single-step combustion reaction [89]. Although Equations 3.5 and 3.15 illustrate the same desorption reaction, the differences between k_3 and k_5 can possibly be resolved by concentration of reaction sites due to gas phase and thermal energy, which can vary based on the reactants present [87].

Table 3.3 Combustion kinetic parameters for the three carbonaceous feedstocks examined.

	Combustion	
	k_0 (s^{-1})	E_a (kJ·mol^{-1})
	Activated charcoal	
k_4 (s^{-1})	$2.93 \times 10^{8} \pm 4.24 \times 10^{6}$	144.0 ± 0.09
k_5 (s^{-1})	$8.10 \times 10^{-3} \pm 0.04 \times 10^{-3}$	-
	Bituminous coal char	
k_4 (s^{-1})	$1.13 \times 10^{4} \pm 1.15 \times 10^{2}$	77.0 ± 0.06
k_5 (s^{-1})	726.5 ± 11.47	64.7 ± 0.10
	Miscanthus char	
k_4 (s^{-1})	$1.02 \times 10^{9} \pm 2.89 \times 10^{7}$	134.7 ± 0.18
k_5 (s^{-1})	$5.19 \times 10^{7} \pm 1.09 \times 10^{6}$	126.3 ± 0.14

3.5.3 Effect of Heating Rate

Further experimentation was performed to explore the impact of heating rate in the TGA. The 60% H_2O-CO_2 gasification run for activated charcoal was repeated using heating rates of 15 and 20 K/min. Similarly, the 20% O_2-Ar combustion run for activated charcoal was repeated using heating rates of 10 and 15 K/min. Fitted kinetic parameters from Table 3.2 and Table 3.2 were used to calculate α, and results are shown in Figure 3.8a. For gasification, the fitted parameters slightly under-predict the α_g at higher heating rates. This is likely due to a heat transfer limitation; steeper thermal gradients in the instrument at higher heating rates create a greater lag between thermocouple temperature and actual sample temperature. Fitted results may be for a slightly lower temperature than the actual sample temperature. A similar effect is shown in Figure 3.8b. Kinetic parameters for combustion slightly over-predict α_c at the lower heating rates. More emphasis was placed on fitting at higher temperatures for combustion, thus, the higher heating rate was used.

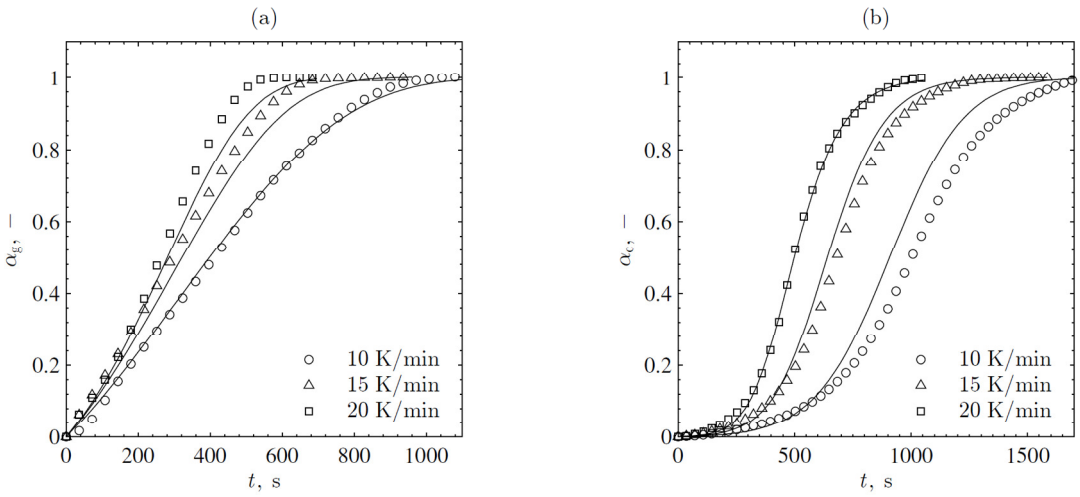

Figure 3.8 Experimental (markers) and fitted (solid) conversion for (a) 60% H_2O–CO_2 activated charcoal gasification and (b) 20% O_2–Ar activated charcoal combustion at various heating rates.

3.5.4 Effect of Particle Size

A series of experiments was performed using a sieved sample of activated charcoal to examine the effect of particle size. Particles were sieved to mesh size 100-170, limiting the particles to only the upper end of the original size distribution (100-400 mesh). Gasification and combustion thermogravimetry was performed using the same procedures described in Section 3.3. Fitted kinetic parameters from Table 3.2 and Table 3.3 were used to calculate α for the sieved particles, and results are shown in Figure 3.9. Parameters predicted α well for both gasification and combustion. Although slightly faster rates of conversion can be expected for smaller particles owing to larger surface area-to-volume ratios, a significant different in rate was not observed for the thermogravimetric experiments.

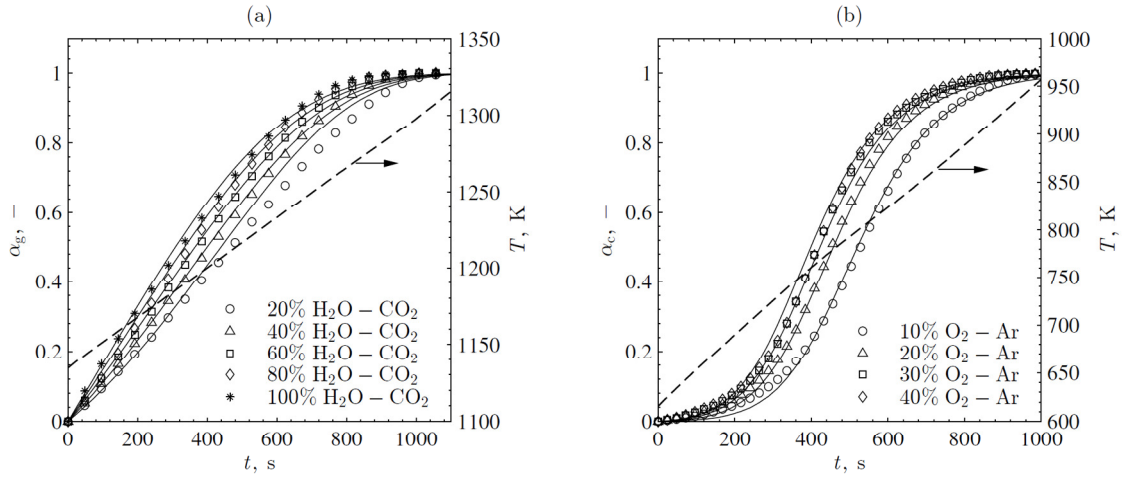

Figure 3.9 Experimental (markers) and fitted (solid) conversion for activated charcoal (100–170 mesh) (a) gasification and (b) combustion with the temporal temperature (dashed) increasing at 10 K/min and 20 K/min, respectively.

3.5.5 Effect of Total Reacting Gas Flow Rate

Gas diffusion to the sample can be rate-limiting if reactions occur sufficiently-quickly. In order to ensure that the reaction was not diffusion-controlled, a series of experiments was performed with various total reacting gas flow rates. The 60% H_2O-CO_2 gasification run and 20% O_2-Ar combustion run for activated charcoal were repeated using total reacting gas flow rates of 100 mL_N/min and 160 mL_N/min. Fitted kinetic parameters from Table 3.2 and Table 3.3 were used to calculate α, and results are shown in Figure 3.10. Conversion rates were nearly equivalent for all three gas flow rate cases for both gasification and combustion, indicating that the reaction was not diffusion-controlled.

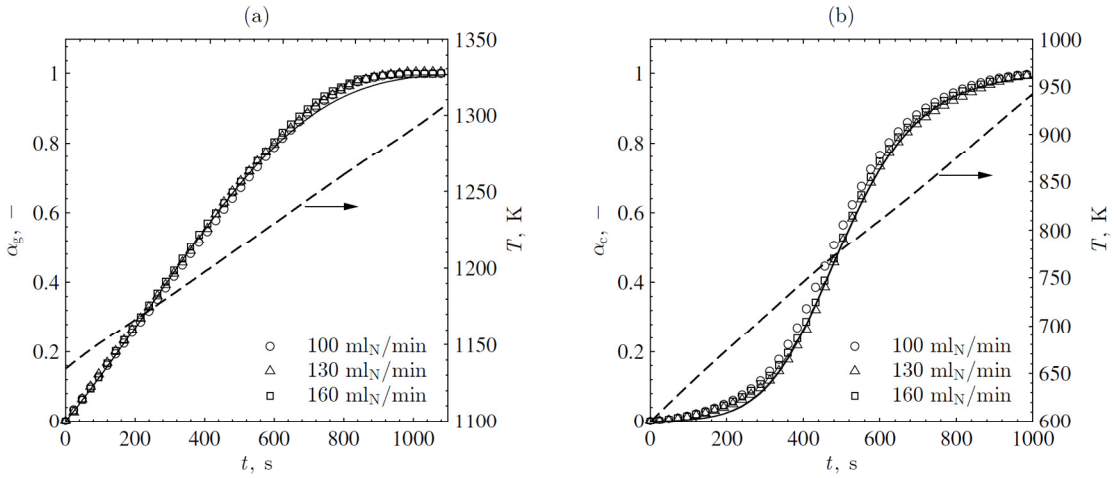

Figure 3.10 Experimental (markers) and fitted (solid) conversion for activated charcoal at various total reacting gas flow rates for (a) 60% H_2O–CO_2 activated charcoal gasification and (b) 20% O_2–Ar activated charcoal combustion with the temporal temperature (dashed) increasing at 10 K/min and 20 K/min, respectively.

3.5.6 Solid Characterization

Feedstock particle microstructures were examined using SEM (Zeiss Leo 1530), shown in Figure 3.11. The image of activated charcoal (Figure 3.11a) shows very small particles with non-spherical geometry. The bituminous coal particle (Figure 3.11b) shows relatively flat features. The miscanthus image (Figure 3.11c) shows the fibrous structure of the cellulosic biomass, and the image of the char after pyrolysis (Figure 3.11d) shows a more strand-like particle feedstock with high surface area. SEM revealed non-spherical geometries, justifying the use of the first-order reaction model as opposed to the contracting volume model, which applies for spherical or cubical geometries [131].

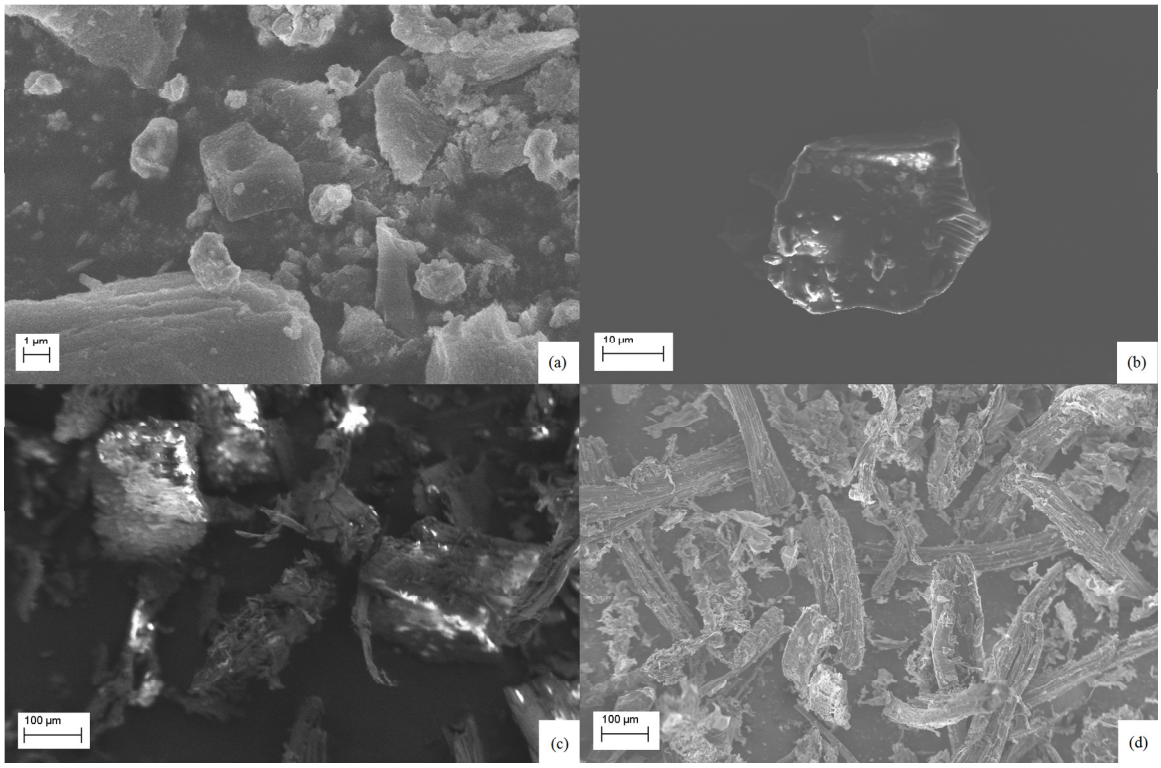

Figure 3.11 SEM images of (a) activated charcoal, (b) bituminous coal, (c) miscanthus, and (d) miscanthus char.

Surface area and porosity characterizations were performed using BET N_2 physisorption analysis (Micrometrics, ASAP 2020). Results for surface area and pore volume of activated charcoal, bituminous coal char, and miscanthus char are shown in Table 3.4. The activated charcoal contained the largest surface area and pore volume due to the activation process creating pores and voids in the structure. The bituminous coal char had very small values for surface area and pore volume, possibly due to the large presence of micropores, which N_2 physisorption has difficulty detecting. Miscanthus char had intermediate values for surface area and pore volume, indicating the presence of some macropores and mesopores.

Table 3.4 Surface area and porosity characterization of the samples performed by N_2 physisorption.

Sample	S_{BET}, $m^2 \cdot g^{-1}$	V_0*, $cm^2 \cdot g^{-1}$
Activated charcoal	1007.9	1.071
Bituminous coal char	0.3	0.001
Miscanthus char	53.1	0.035

* V_0 measured for pores less than ~300 nm width at $P/P_0 = 0.99$

3.6 Summary

Combustion and gasification reaction kinetics were examined using non-isothermal thermogravimetry for three carbonaceous feedstocks: (1) activated charcoal, (2) bituminous coal char, and (3) miscanthus char. In a solar or autothermal gasification application, a wide range of carbonaceous feedstocks may be utilized and materials were chosen to assess representative chars derived from fossil fuels or biomass. Associated rate constants were fitted using Langmuir-Hinshelwood-type rate laws, in contrast to the more commonly used global power rate laws for gasification or combustion reactions. Results confirmed that rates of conversion for gasification and combustion could be accurately captured using Langmuir-Hinshelwood kinetics, allowing for a mechanistic interpretation of surface reactions. Arrhenius parameters were found to be in good agreement with literature for H_2O-CO_2 gasification using the oxygen-exchange mechanism. In addition, apparent activation energies were found to be similar among the three feedstocks for the gasification reactions. Lower activation energies were found for combustion, given a two-step reaction model. Fitted conversion was found to have strong agreement with experimental conversion for both gasification and combustion. Reacting gas concentration had a minor effect on reaction rate for both gasification and

combustion reactions. Miscanthus char had the fastest reaction kinetics for both gasification and combustion by a wide margin, followed by bituminous coal char, then activated charcoal. Fitted kinetic parameters were used to guide reactor designs for a hybrid solar/autothermal gasification application that allowed for rapid, near-complete conversion of the respective feedstocks.

CHAPTER 4. MONTE CARLO RAY TRACING SIMULATIONS[3]

4.1 Introduction

This chapter describes robust radiation modeling for a bench-scale prototype reactor. The reactor uses HFSS radiative heat inputs to simulate solar concentration ratios that would be achievable in a heliostat field/solar power tower configuration. In order to accurately model the heat fluxes on an indirectly-irradiated tubular fluidized-bed reactor, a Monte Carlo ray tracing routine was implemented. The radiation was treated as a large number ($>10^6$) of discrete bundles of energy that could be absorbed or reflected inside of the cavity based on spectral material properties (*i.e.*, collision-based Monte Carlo ray tracing). The methodology of the simulations and reactor geometry are described. A series of grid independence and verification studies were performed, followed by several parametric studies showing how reactor geometry and lamp usage affects input radiative heat fluxes from the HFSS into the prototype reactor. Results of the model are presented and discussed.

4.2 Monte Carlo Ray Tracing Methodology

Monte Carlo ray tracing is a numerical method that allows for the detailed modeling of radiation exchange involving complex geometries with spectral surface properties and directional dependencies. By discretizing radiation as bundles of energy, each with a set power and stochastically-determined path, the method is able to overcome the challenges of using conventional analytical methods. As the radiation is partitioned into more energy

[3] This chapter contains work that was completed under the framework of a joint École Polytechnique Fédérale de Lausanne-Georgia Institute of Technology master's thesis by Iacopo Guschetti

bundles, the solution becomes more statistically valid. If the surfaces are sufficiently discretized, a uniform heat flux for each corresponding surface element can be assumed. The medium inside of the reactor was room air and was considered to be non-participating. There was no window, and all of the surfaces in the reactor were considered to be opaque. Spectral properties were assumed to be independent of temperature.

Initial ray position and direction data were taken from a custom Monte Carlo code [132]. The code was built to provide radiative inputs from the HFSS, which consists of seven 6-kW_e xenon arc lamps mounted on truncated ellipsoidal reflectors. Rigorous calorimetric experiments were performed to measure the total radiative power of the seven lamps entering a 40 mm diameter aperture, which was found to be 6.132 kW_{th} [132]. Position and direction vectors were determined at the focal plane for 64 million rays spread across the seven lamps. Figure 4.1 shows the *x-y* position of 640,000 randomly-selected rays from the Monte Carlo data using all lamps. Although rays can extend as far as several meters outside of focal point, over one-third of the rays fall on a 40 × 40 mm area at the origin, which is shown in black on Figure 4.1.

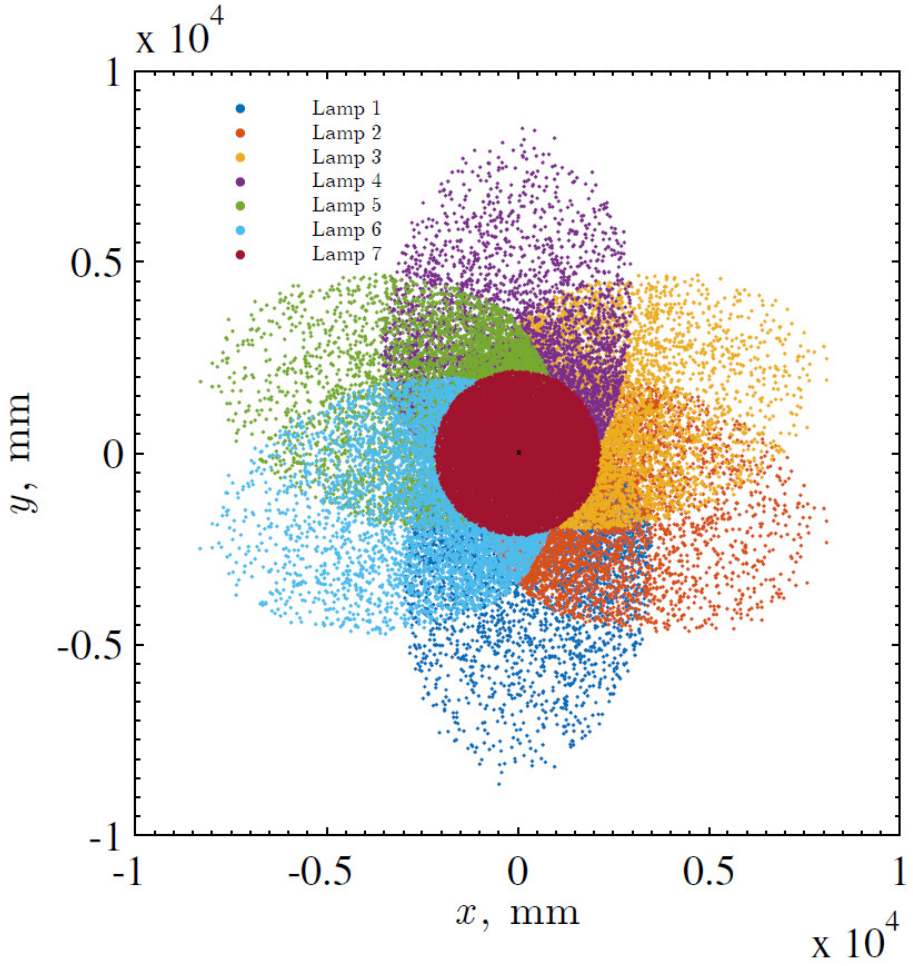

Figure 4.1 Position plot of 640,000 rays in the *x*-*y* plane. Black square at the origin is 40 × 40 mm area at the focal point.

The spectral distribution of the radiation was determined according to Planck's spectral distribution of blackbody emissive power, assuming a refractive index of 1:

$$E_{b\lambda}(T,\lambda) = \pi I_{b\lambda}(T,\lambda) = \frac{2\pi h c_0^2}{\lambda^5 \left[e^{hc_0/\lambda k_B T} - 1 \right]} \tag{4.1}$$

where h is Planck's constant (6.626×10^{-34} m/s), c_0 is the speed of light in a vacuum (2.998×10^8 m/s), k_B is Boltzmann's constant (1.381×10^{-23} J/K), λ is the wavelength,

and T is the temperature. The probability of an emission at a given temperature for a wavelength and direction interval is represented as:

$$P(T,\lambda,\theta)d\theta d\lambda = \frac{2\pi\varepsilon_\lambda(T,\lambda,\theta)I_{b\lambda}(\lambda)\cos\theta\sin\theta d\lambda}{\varepsilon\sigma T^4} \tag{4.2}$$

Spectral, directional emissivity was assumed to be a function of wavelength and zenith angle, giving:

$$P(T,\lambda)d\lambda = d\lambda\int_0^{\pi/2} P(T,\lambda,\theta)d\theta = \frac{2\pi d\lambda\int_0^{\pi/2}\varepsilon_\lambda(T,\lambda,\theta)I_{b\lambda}(\lambda)\cos\theta\sin\theta}{\varepsilon\sigma T^4} \tag{4.3}$$

Integrating the probability density function gives a cumulative distribution function, given as:

$$R(\xi) = \int_{-\infty}^{\xi} P(\xi^*)d\xi^* \tag{4.4}$$

Noting that $P(\lambda)d\lambda$ is equal to zero in the interval (-∞, 0), integrating Equation 4.4 gives:

$$R_\lambda = \frac{2\pi\int_0^{\lambda}\int_0^{\pi/2}\varepsilon_\lambda(T,\lambda^*,\theta)I_{b\lambda}(\lambda^*)\cos\theta\sin\theta d\lambda^*}{\varepsilon\sigma T^4} \tag{4.5}$$

where R_λ represents the probability of a ray's wavelength to be in the range 0 to λ and is uniformly distributed between 0 and 1. The total area under the curve $P(\lambda)$ is equal to 1. Directionality of the rays was given in the Monte Carlo data and surface properties were assumed to be independent of temperature, so Equation 4.5 is reduced to the following expression for diffuse-gray surfaces:

$$R_{\lambda,\text{diffuse-gray}} = \frac{\pi \int_0^{\lambda} I_{b\lambda}(\lambda^*) d\lambda^*}{\varepsilon \sigma T^4} = f\left(T\lambda^*\right) \tag{4.6}$$

where f is the fractional function for temperature T over wavelengths 0-λ*. The desired wavelength interval was discretized and the corresponding values for R_λ were obtained and stored. When assigning wavelengths to the rays, the process was reversed: a random number R_λ was generated from a uniform distribution and the corresponding wavelength was assigned to the ray. After setting the wavelength, the total power of the seven lamps was redistributed to each ray according to the given intensity calculated using Equation 4.1. The dimensionless spectral blackbody intensity of the sun for a surface temperature of T = 5777 K is shown for the wavelength interval of 0 to 6 μm in Figure 4.2. For the solar spectrum, peak intensity occurs at ~0.5 μm.

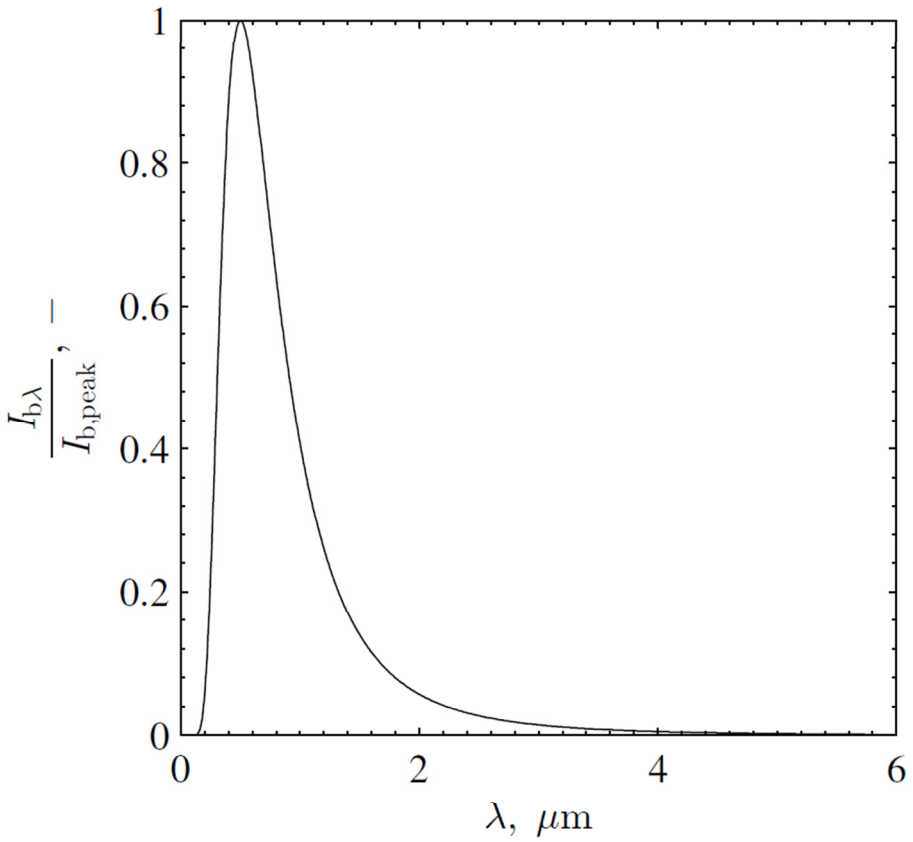

Figure 4.2 Dimensionless spectral blackbody intensity at T = 5777 K for the wavelength interval 0 to 6 μm.

With the program input data determined as described above, the Monte Carlo ray tracing program was able to proceed. A flow diagram for the algorithm is shown in Figure 4.3.

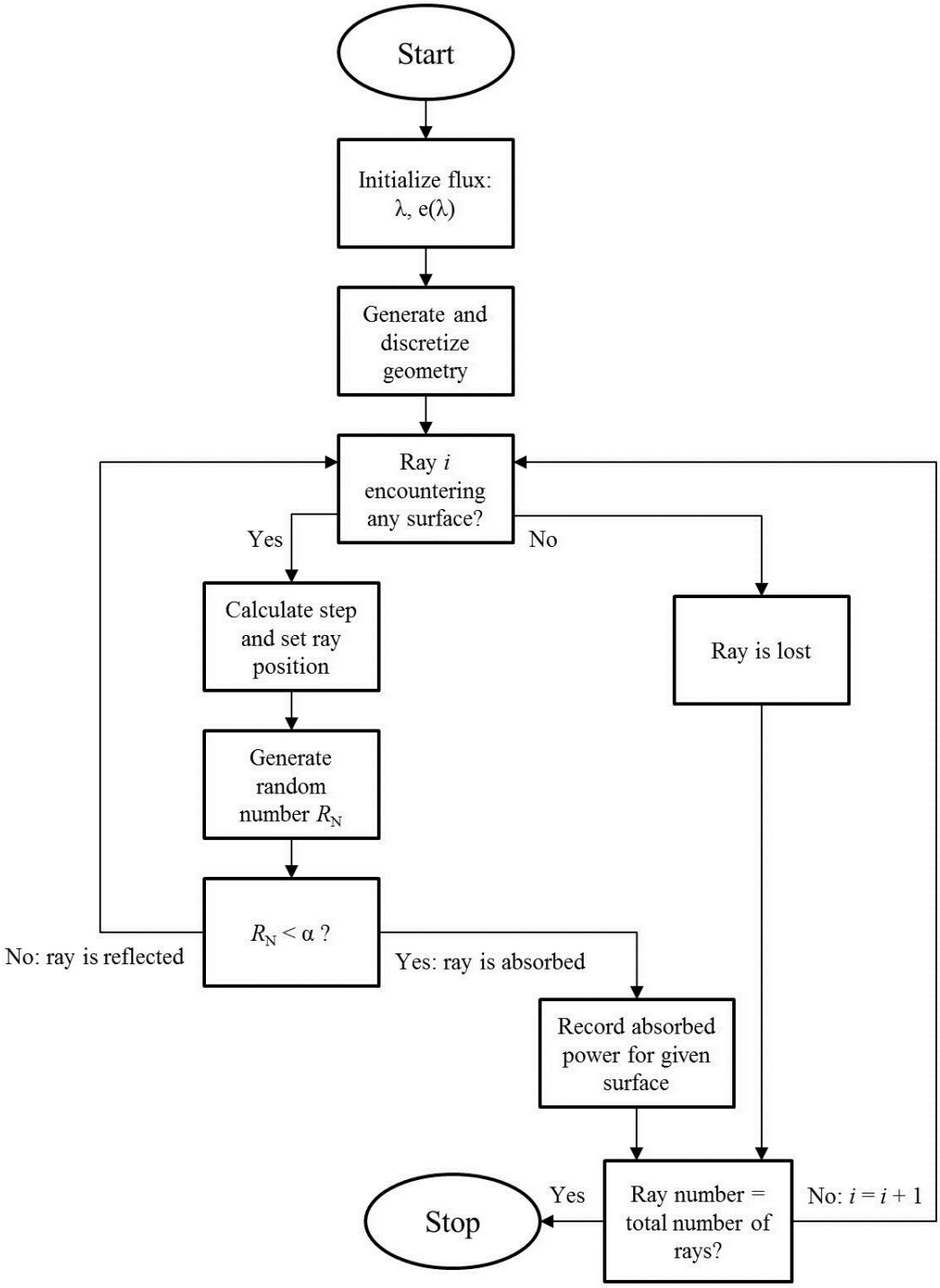

Figure 4.3 Flow diagram of the Monte Carlo ray tracing algorithm.

After the wavelength and flux were initialized for each bundle, the geometric surfaces were generated and discretized. The reactor geometry and discretization are described in an upcoming section. A surface is generically defined in vector form [76] as:

$$\vec{r} = \sum_{i=1}^{3} x_i \left(\upsilon_1, \upsilon_2 \right) \hat{e}_i \,,\ \upsilon_{1,\min} \le \upsilon_1 \le \upsilon_{1,\max} \,,\ \upsilon_{2,\min} \left(\upsilon_1 \right) \le \upsilon_{2,\max} \left(\upsilon_1 \right) \tag{4.7}$$

where $\vec{r}$ is the vector pointing from (0, 0, 0) on the world coordinates to a point on the surface, υ_1 and υ_2 are two surface parameters that depend on the geometry, x_i are the (x, y, z) coordinates of the surface point, and $\hat{e}_i$ are the unit vectors ($\hat{\imath}$, $\hat{\jmath}$, $\hat{k}$) in the x, y, z directions, respectively. For example, a vector $\vec{r}$ pointing to the surface of a cylinder from (0, 0, 0) on the world coordinates is defined as:

$$\begin{gathered} \vec{r} = \left[r_{\text{cyl}} \cos \upsilon_1 + x_{\text{cyl}} \right] \hat{\imath} + \left[r_{\text{cyl}} \sin \upsilon_1 + y_{\text{cyl}} \right] \hat{\jmath} + \left[\upsilon_2 + z_{\text{cyl}} \right] \hat{k} \\ 0 \le \upsilon_1 \le 2\pi \,,\ 0 \le \upsilon_2 \le h_{\text{cyl}} \end{gathered} \tag{4.8}$$

where r_{cyl} and h_{cyl} are the radius and height of the cylinder, respectively. Coordinates (x_{cyl}, y_{cyl}, z_{cyl}) define a point at the bottom, center of the cylinder in the world coordinates. Any shape can be divided into a number of subsurfaces. Two unit tangents to the surface at any point and their corresponding unit surface normal are defined as:

$$\hat{t}_1 = \frac{\partial \vec{r}}{\partial \upsilon_1} \Bigg/ \left| \frac{\partial \vec{r}}{\partial \upsilon_1} \right| ,\ \hat{t}_2 = \frac{\partial \vec{r}}{\partial \upsilon_2} \Bigg/ \left| \frac{\partial \vec{r}}{\partial \upsilon_2} \right| \tag{4.9}$$

$$\hat{n} = \frac{\hat{t}_1 \times \hat{t}_2}{\left|\hat{t}_1 \times \hat{t}_2\right|} \tag{4.10}$$

where υ_1 and υ_2 are ordered such that $\hat{n}$ is pointing outward from the surface. The direction of each ray may be specified as a unit vector with zenith angle θ measured from the surface normal and azimuthal angle ϕ measured from $\hat{t}_1$, giving:

$$\hat{s} = \sin\theta\left[\cos\phi\hat{t}_1 + \sin\phi\hat{t}_2\right] + \cos\theta\hat{n} \tag{4.11}$$

assuming that $\hat{t}_1$ and $\hat{t}_2$ are orthogonal. A two-dimensional schematic that includes some of the relevant parameters in Equation 4.11 is shown in Figure 4.4. The rays in the schematic are assumed to travel within the plane of the cross section. With the ray and surface parameterized, the program began tracing each ray, testing whether it intersected each surface or not.

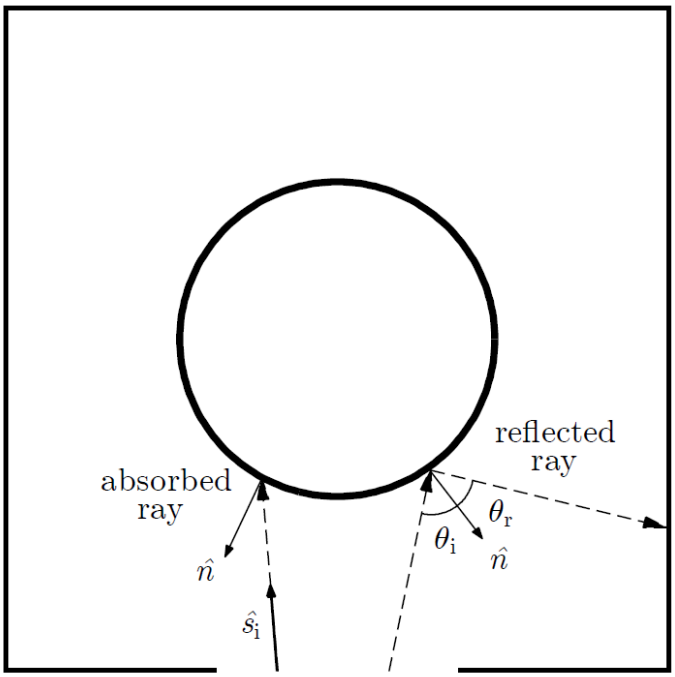

Figure 4.4 Two-dimensional schematic of a cylinder within a cavity. Two rays enter the aperture; one is absorbed and one is reflected.

The vector describing the intersection point is represented as:

$$\vec{r}_i = \vec{r}_o + D\hat{s} \tag{4.12}$$

where $\vec{r}_o$ represents the ray starting at a given point of origin and D represents the distance traveled by the ray before intersection. Rearranging and substituting gives D in terms of the ray unit vector dotted with unit vectors $\hat{\imath}, \hat{\jmath}$, and $\hat{k}$:

$$D = \frac{x(\upsilon_1,\upsilon_2) - x_o}{\hat{s}\cdot\hat{\imath}} = \frac{y(\upsilon_1,\upsilon_2) - y_o}{\hat{s}\cdot\hat{\jmath}} = \frac{z(\upsilon_1,\upsilon_2) - z_o}{\hat{s}\cdot\hat{k}} \tag{4.13}$$

where D is unknown and υ_1, and υ_2 are associated with the given geometry. This equation can be used to determine whether or not an intersection occurs within the surface. If a given ray did not intersect any surface, it was lost and the ray was no longer taken into account in the procedure. If the ray encountered one or more surfaces, its position was updated to the closest surface. When a ray encountered a surface, a random number R_N between 0 and 1 was generated from a uniform distribution, determining whether the ray was absorbed or reflected according to the surface properties. If the ray was absorbed, the associated power was assigned to the surface location where the ray intersected and the ray path stopped. If the ray was reflected, the same procedure was iterated again until the ray was absorbed or lost. The entire algorithm was repeated until all rays were absorbed or lost.

4.3 Reactor Geometry

A cavity-type reactor design was employed in the bench-scale reactor, allowing for the efficient capture of simulated concentrated solar radiation. Blackbody cavities can obtain significantly higher apparent emissivities through the use of small apertures that prevent radiation from leaving. The reactor consisted of an opaque absorbing/emitting tube situated inside of a box with an aperture. For the purpose of obtaining heat fluxes, only the inside dimensions of the cavity were of interest. The dimensions of the reactor are shown in Figure 4.5. The cavity dimensions were 110 × 160 × 110 mm, and the outer diameter of the tube was 52 mm. The tube was initially positioned at the center of the cavity in the *x*-*z* plane. The circular aperture was 40 mm in diameter and was positioned at the center of the front of the cavity.

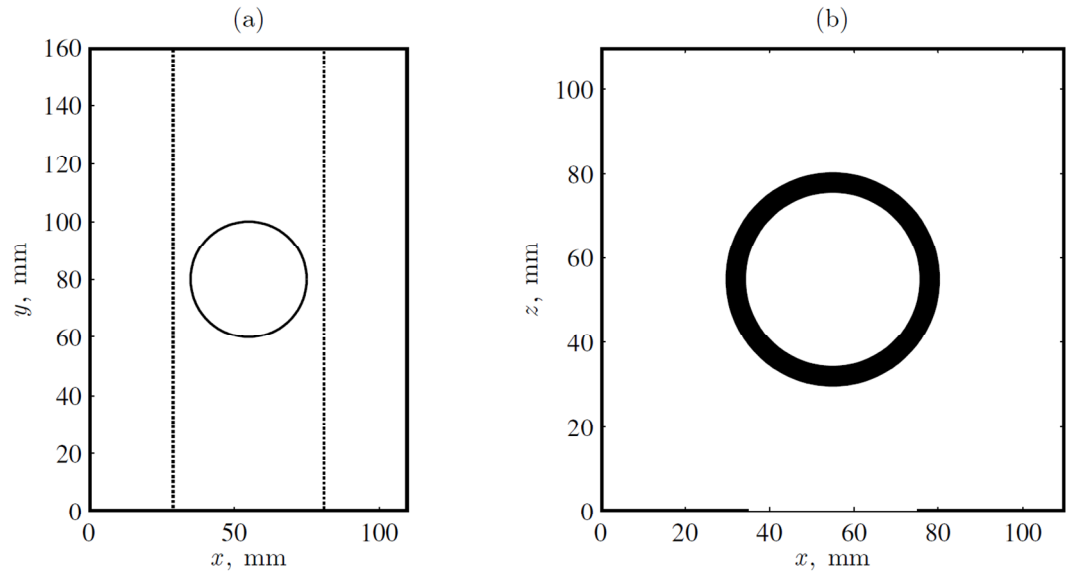

Figure 4.5 (a) Reactor geometry viewed from the front, with the emitter tube inside of the cavity shown using dotted lines. (b) Rector geometry viewed from the top, with cross-section taken at the aperture (y = 80 mm).

4.4 Reactor Surface Properties

The choice of material had a significant effect on the captured radiation due to spectrally-dependent surface properties. The reactor cavity used two materials that are common in concentrated solar applications: Al_2O_3 and SiC. The cavity walls were made of Al_2O_3, which has a relatively low thermal conductivity, is chemically inert, and has a high melting point. It also has a relatively high reflectivity, allowing it to redirect radiation to the emitter tube. The spectral hemispherical emissivity of Al_2O_3 as a function of wavelength was obtained from experimentally-measured values [133], and is shown in Figure 4.6. The gray band approximation was used for the Monte Carlo ray tracing simulation. The lower emissivity at shorter wavelengths (λ<5 μm) allowed the walls to reflect significant incoming radiation, as >98% of energy emitted by the sun falls in this wavelength range. At longer wavelengths, Al_2O_3 exhibits an emissivity close to unity.

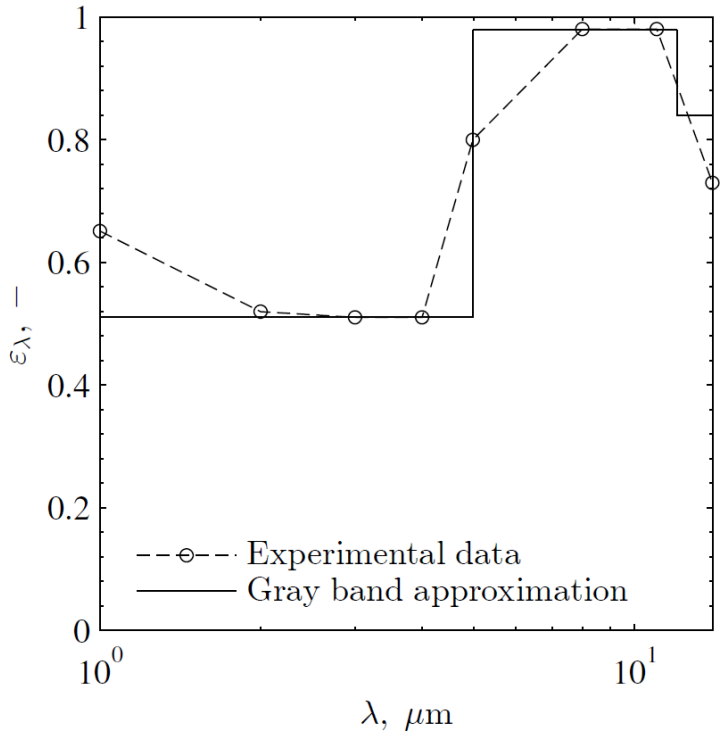

Figure 4.6 Experimental data and gray band approximation of spectral hemispherical emissivity for Al_2O_3 plotted against wavelength [133].

The emitter tube was made of SiC, which has a very high emissivity and high thermal conductivity. This allowed radiation to be effectively captured and transported to the reactants via conduction. The fluidized bed inside of the tube was not relevant to the Monte Carlo model and is described in greater detail in an upcoming chapter. Experimental data taken at high temperatures (>1000 K) showed that the spectral hemispherical emissivity of SiC was almost constant over the wavelengths of interest and generally varies between ε_λ = 0.90 and 0.96 [134]. For this reason, the Monte Carlo model used a total, hemispherical emissivity of ε = 0.93. A diffuse-gray approximation for SiC emissivity has been applied to Monte Carlo ray tracing in a previous study [43].

4.5 Reflection Mode

Two reflected modes were initially implemented in the program: diffuse and specular. For specular reflections, the angle of reflection from the surface normal is equal to the angle of incidence, following from the law of reflection from optics, and is represented in vector form as:

$$\hat{s}_{\mathrm{r}} = \hat{s}_{\mathrm{i}} + 2\left|\hat{s}_{\mathrm{i}} \cdot \hat{n}\right| \hat{n} \tag{4.14}$$

Diffusely-reflected rays are reflected in all directions from the plane of the surface. The reflection mode depends on surface roughness at the microscopic level; rough surfaces reflect diffusely and smooth surfaces reflect specularly. When the reflection was set to diffuse, the angles for the reflected ray were determined using the relations:

$$\theta_{\mathrm{r}} = \arcsin\left(\sqrt{R_{\mathrm{N}}}\right) \tag{4.15}$$

$$\phi_{\mathrm{r}} = 2\pi R_{\mathrm{N}} \tag{4.16}$$

where R_{N} is a random number from a uniform distribution between 0 and 1, and is separately generated for each angle.

Running simulations with specular and diffuse reflections revealed only small variations in distribution of radiation within the cavity, possibly due to significant initial absorption of incoming rays by the tube. The Al_2O_3 walls were rough and porous, which leads to highly-diffuse reflections. The SiC tube also has a relatively rough, dull surface,

causing diffuse reflections. For this reason, reflection mode was set to diffuse for all surfaces in the reactor.

4.6 Number of Rays & Grid Independence

Using a small number of rays leads to high variability in the Monte Carlo simulation results due to the use of random numbers. However, as the sample size increases, the standard error decreases. Therefore, using a larger number of rays gives a more accurate result at the expense of increased computational time. In addition, the grid needs to be sufficiently discretized such that the extrema of heat flux can be captured on the surface. For these reasons, investigations on the effects of the number of rays and grid independence were performed.

Several different numbers of rays were investigated:

- 6×10^6 rays
- 6×10^5 rays
- 6×10^4 rays
- 6×10^3 rays

The full number of rays 6×10^7 rays was not investigated due to the significant computational time required. Several different mesh sizes were investigated for grid independence:

- 1×1 mm for the emitter tube, 2×2 mm for the cavity walls
- 2×2 mm for the emitter tube, 4×4 mm for the cavity walls
- 4×4 mm for the emitter tube, 6×6 mm for the cavity walls

- 6 × 6 mm for the emitter tube, 8 × 8 for the cavity walls

The discretization for the emitter tube was finer than that of the cavity walls due to the radiative flux directly impinging on the pipe, creating much greater local extrema. The cavity walls were mainly irradiated by reflected rays, which led to more diffuse irradiation and significantly lower heat fluxes.

4.6.1 Number of Rays

In order to examine the effect of the number of rays on the simulation results, the other parameters of the simulation were fixed. The finest mesh was used, with 1 × 1 mm elements for the emitter tube and 2 × 2 mm elements for the cavity walls. The simulations were run until all of the rays were either absorbed or lost, and the heat flux absorbed by each surface element was obtained.

The error was calculated relative to the case with the maximum number of rays (6 × 10^6 rays) using the L^2–*norm* of the difference between the heat flux for each surface, represented as:

$$L^2 - norm = \frac{\sum_{i=1}^{N} \left\| q_i - q_{i,\text{ref}} \right\|_2}{\sum_{i=1}^{N} \left\| q_{i,\text{ref}} \right\|_2} \tag{4.17}$$

where q_i and $q_{i,\text{ref}}$ are the resulting heat fluxes on i^{th} discretized surface for the investigated number of rays and the reference case, respectively. The results of the computed errors are shown as a function of the number of rays in Figure 4.7.

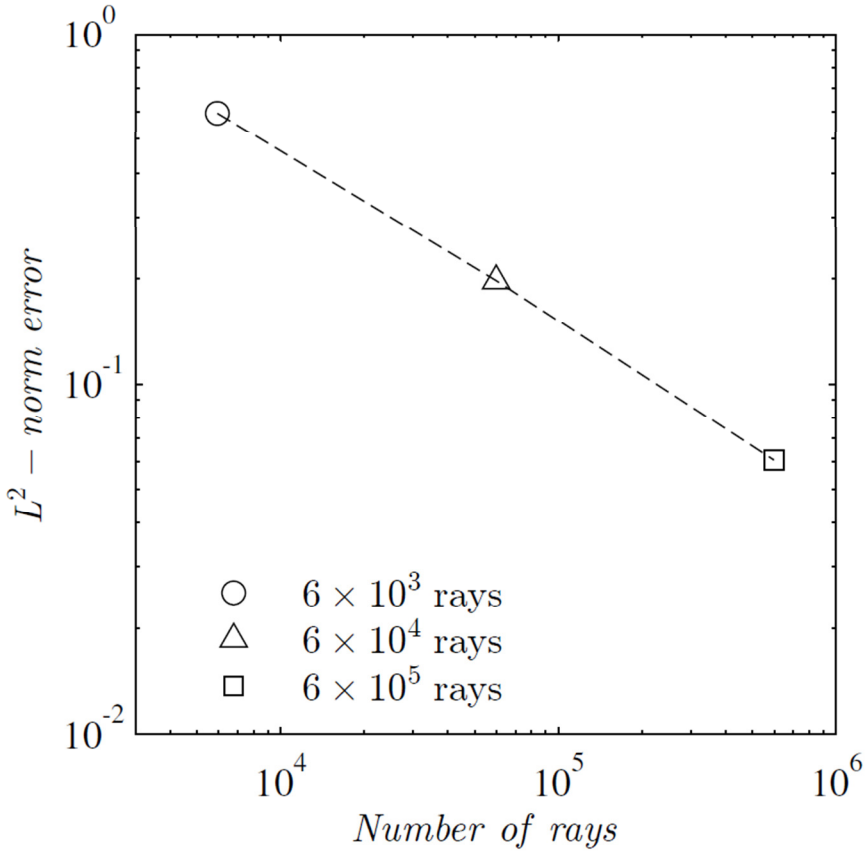

Figure 4.7 L^2*–norm* error as a function of number of rays compared with the 6×10^6 ray reference case.

As expected, the error decreased as more rays were used. In addition, the figure shows that error converges, decreasing logarithmically. The plot shows that the L^2*–norm* error for 6×10^5 rays was ~6%. Following the logarithmic trend predicts that 10^6 rays would achieve an error less than 5%, therefore each simulation was run with a minimum of 10^6 rays. Other works have used 10^6 rays for Monte Carlo modeling on a similar scale of reactor [32, 33].

4.6.2 Grid Independence

Grid independence studies were run with the maximum number of rays (6×10^6) to ensure accurate results. Similar to the number of rays, using a finer mesh improves accuracy at the expense of computational time. Therefore, the goal was to evaluate error compared with the finest-mesh reference case: 1 × 1 mm elements for the emitter tube and 2 × 2 mm elements for the cavity walls. L^2*–norm* error was calculated as in Equation 4.17 for the tube and the walls separately, and results are shown in Figure 4.8. For both the tube and the walls, the error decreased with mesh element area. For the tube, the 2 × 2 mm mesh had an error of 0.45% compared with the finest mesh. For the walls, the 4 × 4 mm mesh had an error of ~1% when compared with the finest mesh. In order to limit simulation times, meshes of 2 × 2 mm for the emitter tube and 4 × 4 mm for the walls were used, and there was minimal impact on accuracy compared with the finest mesh.

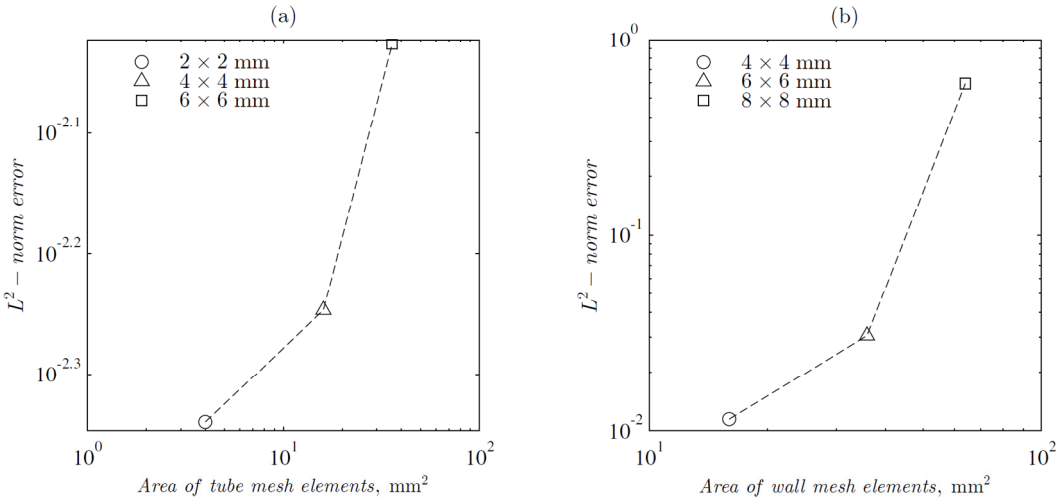

Figure 4.8 L^2*–norm* error as a function of mesh element area for (a) the tube and (b) the walls compared with the 1 × 1 mm and 2 × 2 mm reference cases, respectively.

4.7 Monte Carlo Results

All Monte Carlo simulations were run with 10^6 rays, a mesh size of 2 × 2 mm for the emitter tube, and 4 × 4 mm for the walls. The exception to this wall mesh size was the circular aperture, which used 2 × 2 mm elements to better approximate the shape of a circle. Simulations were run with less than the total seven lamps due to the excessive heat fluxes that would be provided to the reactor. Heat flux distributions on the tube and the walls were evaluated for a number of different cases. Using the initial reactor geometry, a square aperture was compared to a circular aperture, and three different lamp configurations were investigated. In addition, three different tube positions were examined in the *z*-direction. Finally, the differences between the use of top and bottom lamps were observed.

4.7.1 Square versus Circular Aperture

The shape of the aperture was chosen to be circular due to the ellipsoidal shape of the reflectors and the rotational symmetry of the lamps creating a round focal point. However, a circular aperture is more challenging to machine as well as build in a Cartesian mesh system. A 40 × 40 mm square aperture was examined in the Monte Carlo simulation and compared with the 40 mm-diameter circular aperture. The two aperture shapes are shown in Figure 4.9. Although the circular aperture is not perfectly circular within the mesh, the shape is a good approximation of a circle while avoiding a complicated or overly-fine mesh. When using a circular aperture, the area of the aperture is reduced by 17% as compared to a square aperture of the same size. This would reduce reradiation losses from the cavity, which were not captured in the model.

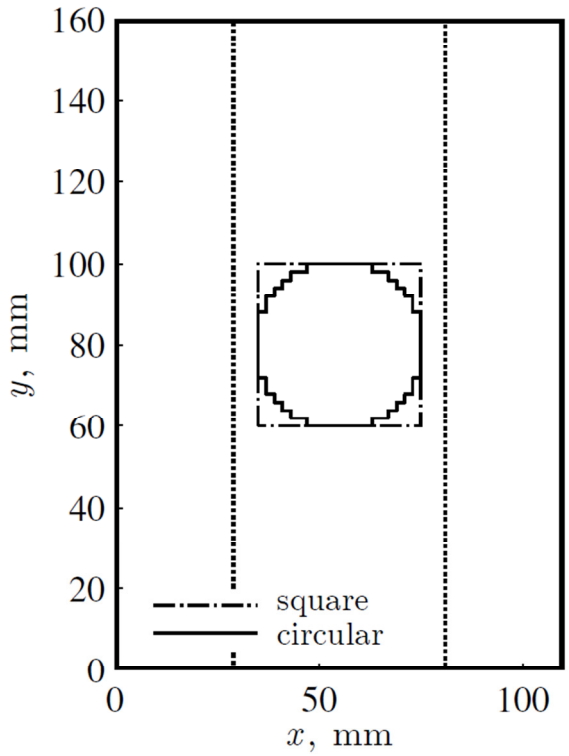

Figure 4.9 Model geometry of the 40 × 40 mm-square aperture (dot-dashed) and 40 mm-diameter circular aperture (solid).

Results from using two lamps (Lamps 4 and 7) on the different aperture shapes are shown in Figure 4.10 and Figure 4.11. Figure 4.10 shows the heat flux distribution on the front of the pipe for both aperture shapes. Although the heat flux at the focus was very similar for both cases, slight differences in the flux at the outer edges of the focus were observed. The peak flux was 592.4 kW/m^2 for the circular aperture, while the peak flux for the square aperture was slightly higher at 599.6 kW/m^2. Figure 4.11 shows the absorbed fluxes over a 40 × 40 mm area at the center of the tube in the *x*-*y* plane. The heated area extended slightly more towards the edges for the square aperture versus the

circular aperture. The average heat fluxes over the 40 × 40 mm area were 162.5 kW/m^2 for the circular aperture and 176.5 kW/m^2 for the square aperture. While using a circular aperture slightly reduced the heated area and overall incident heat flux on the tube, these effects would likely be minor in comparison with the reduction in reradiation losses that would result from using a circular aperture. Therefore, a circular aperture was preferable for the design and was used for all following simulations.

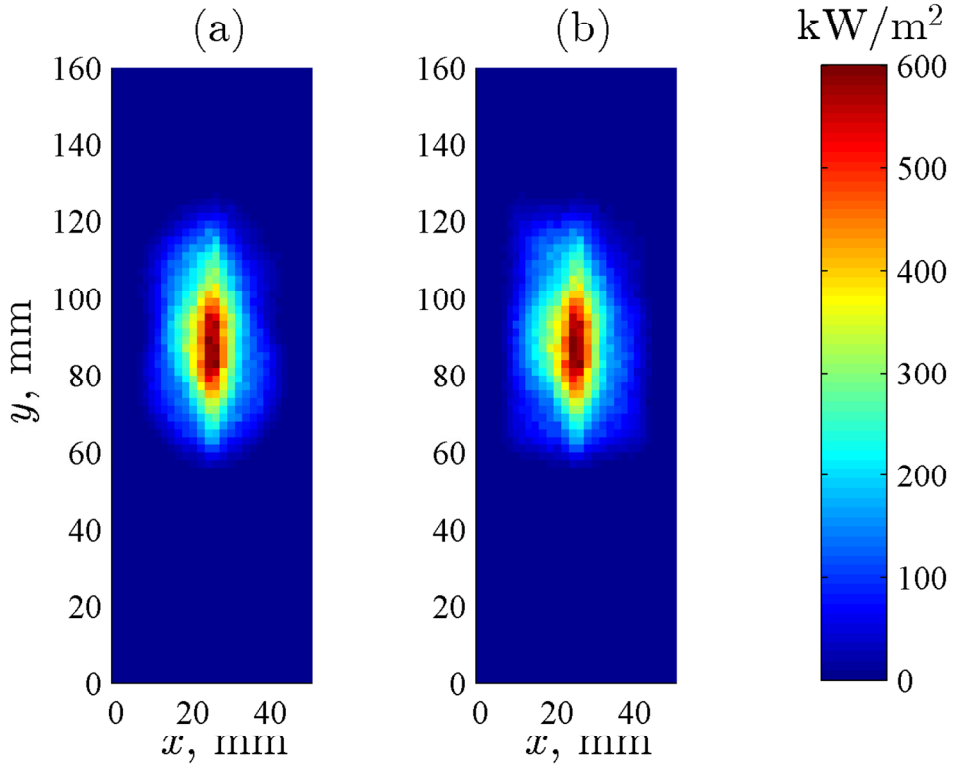

Figure 4.10 Heat flux distributions on the front of the emitter tube for a (a) circular and (b) square aperture.

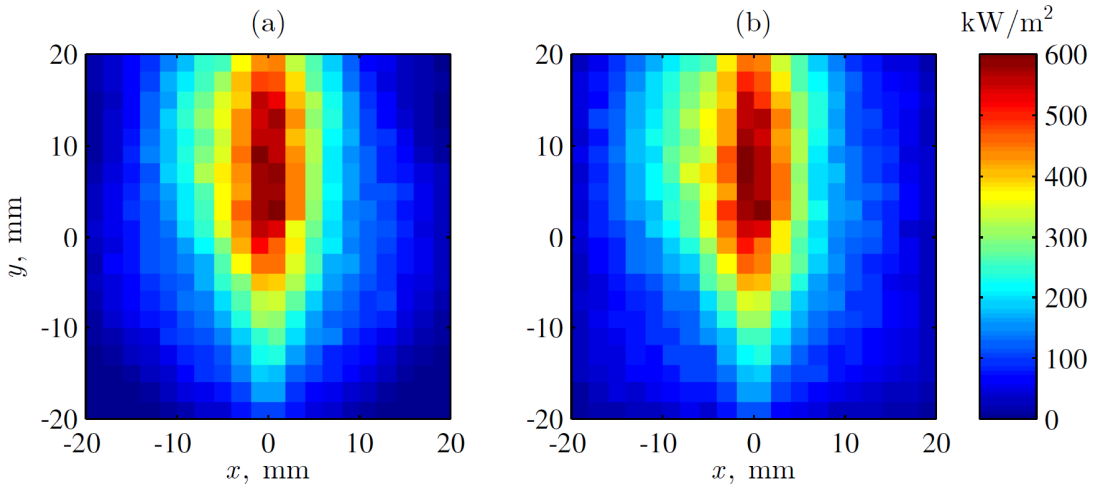

Figure 4.11 Heat flux distributions on a 40 × 40 mm area at center of the emitter tube for a (a) circular and (b) square aperture.

4.7.2 Number of Lamps

Three different configurations of lamps were tested in the Monte Carlo simulations with the tube placed at the center of the cavity. Symmetrical radiation was desirable from the standpoint of efficient heat transfer, so use of one side lamp necessitates the use of the opposing side lamp (*e.g.*, Lamps 3 and 5). Using all seven lamps would heat the tube significantly more than necessary, so investigations focused on the use of the center and bottom lamps (Lamps 7, 3, 4, and 5). The three cases simulated were two lamps (Lamps 7 and 4), three lamps (Lamps 7, 3, and 5), and four lamps (Lamps 7, 3, 4, and 5), and resulting heat fluxes on the front of the tube are shown in Figure 4.12. As expected, the number of lamps had a clear effect on heat flux, creating solar concentrations that were almost twice as high for four lamps compared to two. The total thermal lamp power was 1.752, 2.628, and 3.504 kW for two, three, and four lamps, respectively. This resulted in powers of 401, 532, and 710 W absorbed on the tube surface, respectively.

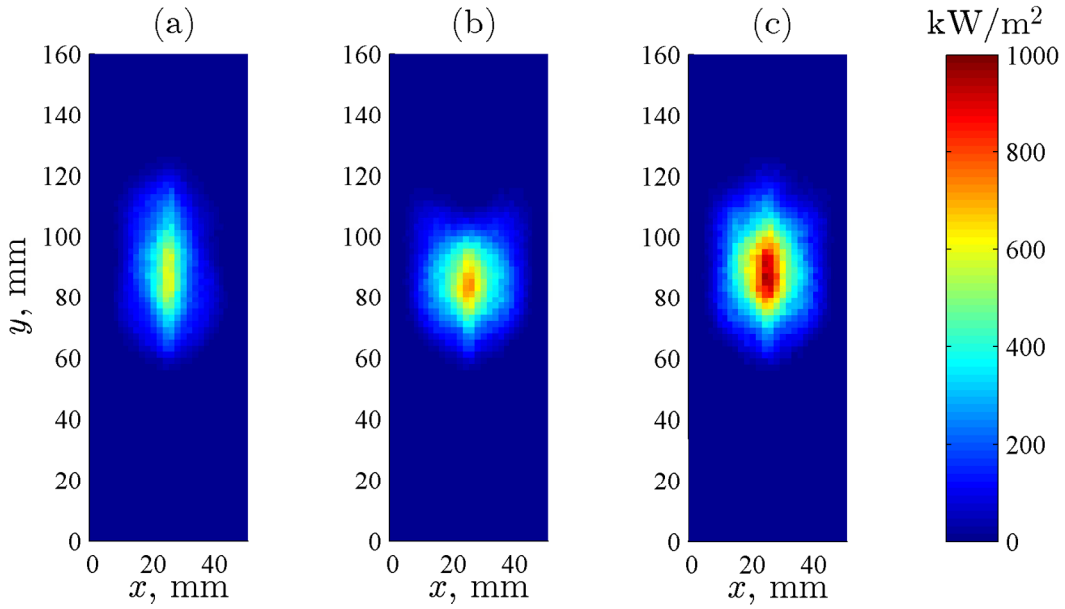

Figure 4.12 Heat flux distributions on the front of the emitter tube for (a) two (Lamps 4 and 7), (b) three (Lamps 3, 5, and 7), and (c) four (Lamps 3, 4, 5, and 7) lamps.

Figure 4.13 shows the absorbed heat fluxes on a 40 × 40 mm area at the center of the tube. It can be observed that using different lamps affected the shape of the incident flux as well as the level of peak flux. Average heat fluxes absorbed on the 40 × 40 mm area at the center were 162.5, 237.8, and 290.3 kW/m^2 for two, three, and four lamps, respectively. Peak heat fluxes were 592.4, 727.4, and 955.5 kW/m^2, respectively. Use of the side lamps caused the incident flux to be wider, as can be seen in Figure 4.13b and Figure 4.13c. It was determined that using more than two lamps would likely cause excessive temperatures and problematic thermal stresses at the focus, so further simulations were run using only two lamps. Furthermore, use of two lamps on the same vertical axis was conducive to efficiently heating a vertical-tube reactor configuration while minimizing losses to the cavity walls.

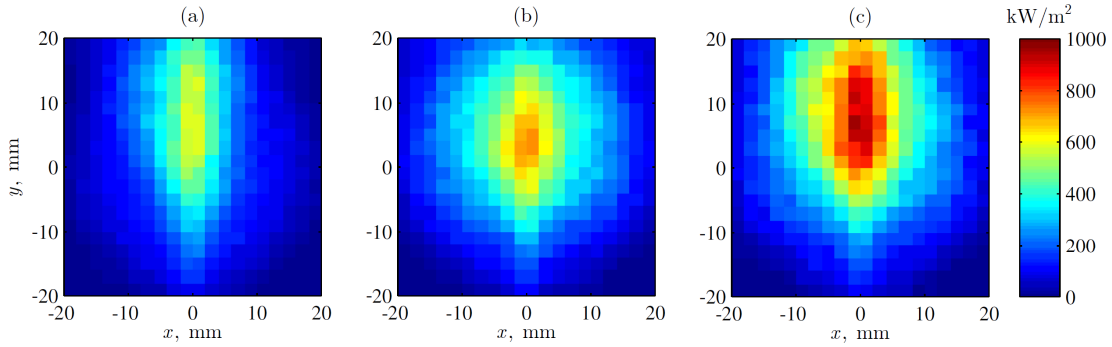

Figure 4.13 Heat flux distributions on a 40 × 40 mm area at center of the emitter tube for (a) two (Lamps 4 and 7), (b) three (Lamps 3, 5, and 7), and (c) four (Lamps 3, 4, 5, and 7) lamps.

4.7.3 Tube Position

The directionality of the incoming rays caused the radiation to become more diffuse as it moved to the back of the reactor cavity. In addition, the proximity to the aperture affected reflection losses from the tube. Three different positions of the emitter tube were tested to examine these effects. As mentioned previously, symmetrical radiation was desirable, so all positions were in the center of reactor in the *x*-direction. The three *z*-distances from the front of the reactor were 35 mm (close), 55 mm (center), and 75 mm (far), shown in Figure 4.14. The model measured incident flux and did not account for reradiation losses (*i.e.*, surface emissions from the inside of the cavity), which would be significant at high temperatures.

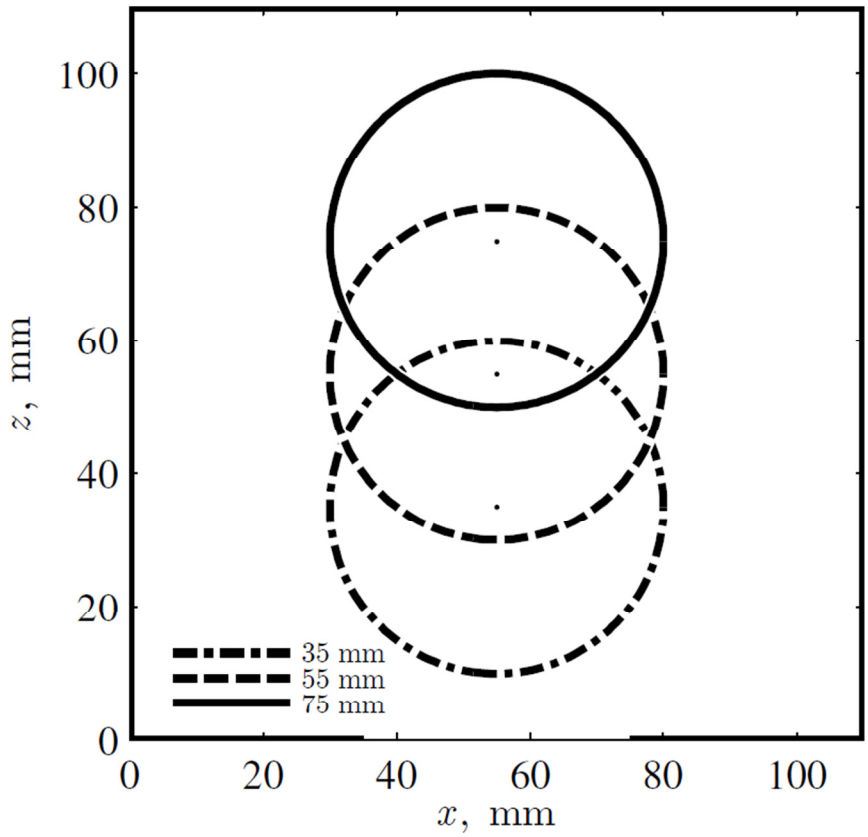

Figure 4.14 The emitter tube at three different positions in the z-direction. Distance is measured from the front of the cavity to the center of the tube.

Figure 4.15 shows the heat flux distributions on the front of the tube for the three distances. The total power absorbed by the tube did not change significantly between the three cases, and slightly increased for the farther tube. This is potentially a result of the reflected rays staying within the cavity due to the smaller view factor between the tube and the aperture. The figure shows that the farthest tube had significantly more diffuse irradiation with the largest heated area. As the tube was moved closer to the aperture, the heat flux became more circular and concentrated at the center of the tube.

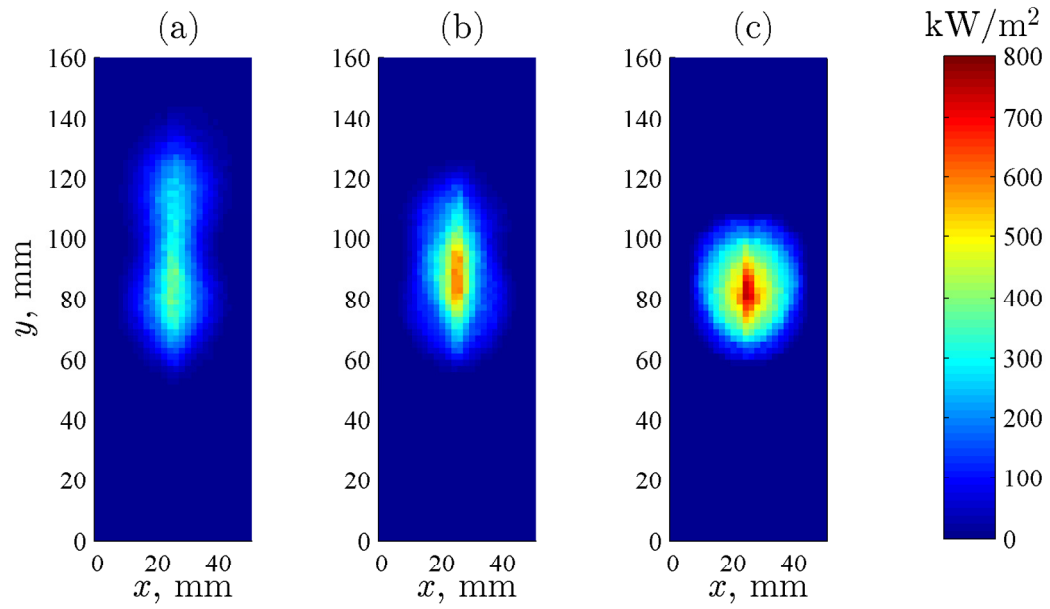

Figure 4.15 Heat flux distributions on the front of the emitter tube for distances of (a) 75, (b) 55, and (c) 35 mm from the aperture.

Figure 4.16 shows the same heat flux distributions on a 40 × 40 mm area at the center of the tube. The average heat fluxes across the area were 122.1, 162.5, and 205.2 kW/m^2 for the 75, 55, and 35 mm distances, respectively. Peak heat fluxes were 391.5, 592.4, and 748.2 kW/m^2, respectively. While the average heat flux was significantly lower for the farthest distance, it was spread across an area almost twice as large. As with using more lamps, positioning the tube closer to the aperture created highly localized heat fluxes that could cause steep temperature gradients and thermal stresses. Therefore, a position halfway between the center and far distances, 65 mm, was chosen for the last case study.

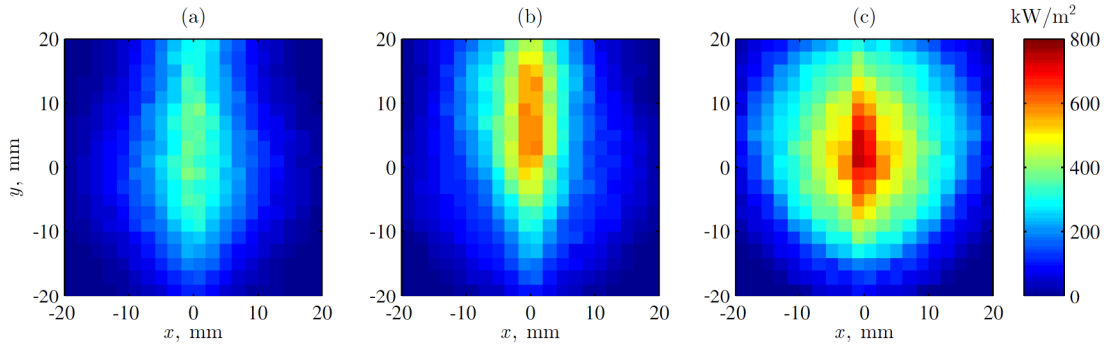

Figure 4.16 Heat flux distributions on a 40 × 40 mm area at center of the emitter tube for distances of (a) 75, (b) 55, and (c) 35 mm from the aperture.

4.7.4 Top versus Bottom Lamp

The final investigation compared the use of the top and bottom lamps and their effect on the position of the incident radiation. With the tube placed 65 mm from the cavity, simulations were run with the center and bottom lamps (Lamps 7 and 4), and the center and top lamps (Lamps 7 and 1). Figure 4.17 shows the heat flux distributions on the front of the tube for both cases. The total power absorbed by the tube was almost identical for both cases at 408 W, but using the top lamp clearly shifted the heated portion of the tube downward. This absorbed power corresponded to 23.3% of the total power emitted from the lamps. Because the inside of the tube contains gases flowing upward and a bed of inert and reacting particles at the bottom, heating a lower portion of the tube would be favorable for endothermic gasification reactions. Therefore, the top lamp was selected as the preferred lamp to use. The peak and average heat fluxes across a 40 × 40 mm area at the center of the tube were 468.2 kW/m^2 and 138.9 kW/m^2 in this configuration, respectively.

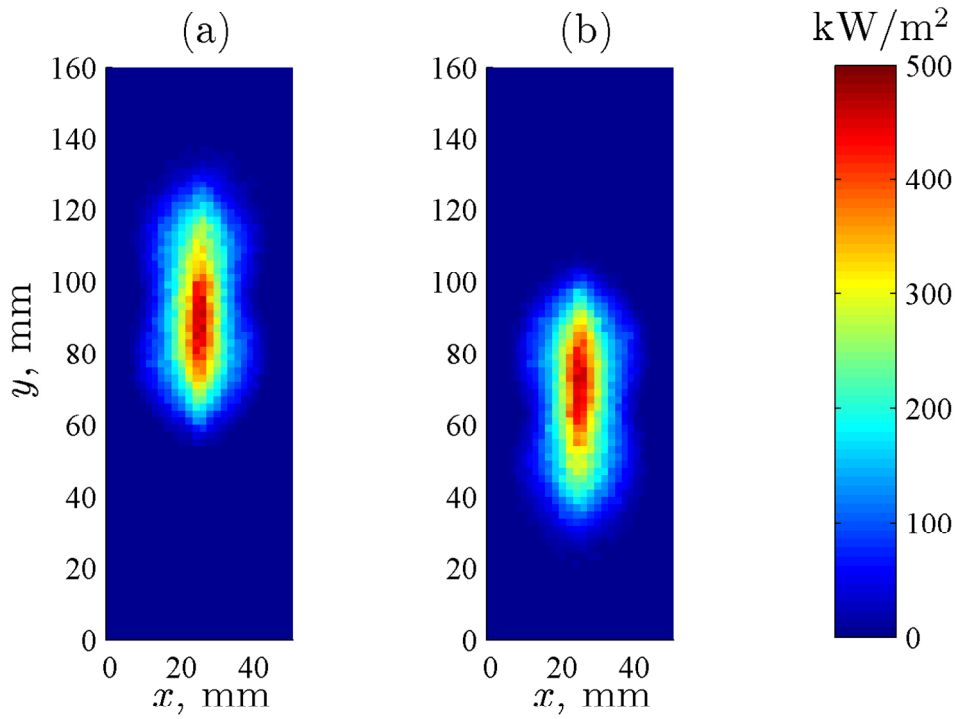

Figure 4.17 Heat flux distributions on the front of the emitter tube for use of the (a) center and bottom lamps (Lamps 7 and 4) and (b) center and top lamps (Lamps 7 and 1) at a distance of 65 mm from the aperture.

4.8 Summary

The Monte Carlo ray tracing analysis revealed a set of possible conditions and geometries for a single-tube reactor in a cavity. The key objective was to provide sufficient irradiation to supply the endothermic gasification reactions while mitigating thermal gradients and losses to the cavity walls. With these goals in mind, the final run conditions were irradiation using the top and center lamps, placing the tube 65 mm from a circular aperture. This ensured that the irradiation remained close to the position of the bed inside of the tube while diffuse enough to reduce thermal shocks. While the Monte Carlo model included reflection and absorption by the cavity walls, it did not include emissions from

the hot surfaces back to the tube, which would be significant and result in more uniform heat distributions on the tube. With estimations of the heat flux on the tube obtained, the next step was to design and fabricate the prototype reactor for testing in a HFSS.

CHAPTER 5. REACTOR DESIGN & FABRICATION

5.1 Introduction

This chapter describes the prototype reactor design and fabrication. The chapter begins with a review of previous reactor designs that are relevant to the study. The goals of the design were established, and a fluidized-bed reactor configuration was selected and developed using appropriate reactor materials. The fabrication and set up of the reactor is described, including associated instrumentation to monitor temperatures and pressures and control mass flows. The feedstock and its properties are presented, including basic fluidization calculations. Descriptions of the HFSS and downstream instrumentation to monitor gas flows are also provided.

5.2 Relevant Literature

A number of different reactor designs have been prototyped and tested for solar-driven gasification, many of which are noted in the literature review section of Chapter 2. This section highlights some the most relevant designs using indirect irradiation and fluidized beds, particularly with respect to reactor materials and geometry. Indirectly-irradiated designs have the benefit of avoiding the use of a fragile quartz glass window, which is prone to fouling, at the expense of less exergy losses from transporting heat to the reactants via conduction through an opaque absorber.

Tubes are the most commonly-used opaque absorbers. Murray and Fletcher [48] performed experiments using steel and stainless steel tubes housing a fluidized bed to gasify cellulose using concentrated solar energy. The fluidized bed was situated in an

Al_2O_3-lined cylindrical cavity to receive the radiation. Experiments were performed at 1500-1600 K, but the performance of the tubes was limited by very long heat-up times (one-and-a-half to two hours) caused by the relatively low thermal conductivity of steel. Melchior *et al.* [34] used a silicon-infiltrated SiC tube as an opaque absorber to gasify beech charcoal in an entrained flow. The reactor also used an Al_2O_3-lined cylindrical cavity to capture and redistribute radiation. Lichty *et al.* [50] tested a multiple drop-tube solar gasification reactor with a reflective polished-aluminum cavity. Tubes were constructed of either Al_2O_3 or a Ni alloy. Temperatures of up to 1660 K were reached, but Al_2O_3 tubes required a higher power input due to the poor absorptivity. Martinek *et al.* [42, 43] continued this design, employing silicon carbide tubes to absorb and transfer incoming radiation, which were able to reach higher temperatures than Inconel tubes due to the higher melting point. Kruesi *et al.* [53] implemented a SiC drop tube containing a Si-SiC reticulate porous ceramic foam to increase the particle residence time and improve heat transfer. The tube was placed in an Al_2O_3-SiO_2 cavity, and temperatures of 1256-1428 K were observed, with temperatures primarily being limited by the ash melting temperature of the biomass feedstock. Tube inner diameters have ranged from 9 [34] to 51 mm [48] depending on the reactor scale and particle transport mode.

Other geometries for indirectly-irradiated configurations have included plates and cavities. Piatkowski *et al.* [35, 36, 38] tested an indirectly-irradiated packed bed reactor that transferred heat to the reactants using a disk-shaped emitter plate. The emitter plate was constructed out of SiC-coated graphite, and the cylindrical cavity was lined with SiC tiles and Al_2O_3-SiO_2 insulation. Although the reactor operated in a batch-mode, it could handle a wide variety of carbonaceous feedstocks and temperatures of up to 1490 K were

reached. Hathaway [135] experimented with an Inconel cylindrical cavity to transfer heat to an outer shell containing a molten salt, steam, and biomass particles. The reactor was designed to operate at 1200 K, and the use of Inconel allowed for a higher apparent emissivity than if Al_2O_3 were used due to the spectral properties. Recently, Müller *et al.* [136] developed and demonstrated an indirectly-irradiated vortex-flow reactor that employed a cylindrical cavity made of SiC. The reactor also used Al_2O_3-SiO_2 insulation on the outer shell. This allowed for the efficient capture and transfer of heat to the reactants without the use of a window, and temperatures of up to 1546 K were reached. Notably, the reactor operated at higher pressures of up to 6 bar, a first for "on-sun" gasification.

Fluidized beds are commonly-used designs in combustion and gasification applications, as they allow for continuous operation, rapid adjustment of the reactant inputs, high particle residence times, and high gas-solid contact with efficient heat and mass transport. An early study by Taylor *et al.* [14] used a quartz tube fluidized bed under direct concentrated solar irradiation to gasify charcoal with CO_2. Müller *et al.* [90] and later von Zedtwitz *et al.* [31, 137] used a quartz tube fluidized bed to gasify charcoal under direct concentrated solar irradiation. An internally-circulating fluidized bed to gasify coal cokes was demonstrated by Gokon *et al.* [39-41] and Abe *et al.* [138]. The reactor consisted of a stainless steel tube with a quartz window to allow for direct irradiation of the particles. All of the aforementioned fluidized-bed reactors operated in a batch style, precluding true steady-state operation. In addition to the indirectly-irradiated reactors, Murray and Fletcher [48] also experimented with a quartz tube fluidized bed that could be fed continuously. One drawback of fluidized-bed designs compared to

packed beds is the necessity of small, relatively uniform feedstock particles and thus costlier feedstock preparation. While directly-irradiated fluidized beds allow for efficient heat transfer to the particles, they also face challenges with pressurized operation and maintaining optical transparency though prolonged use. Experimental investigations of indirectly-irradiated fluidized beds are lacking in literature [139].

5.3 Design & Fabrication

5.3.1 Design Criteria & Selection

Several design goals were considered during the selection of a reactor type. The first was the ability to run continuously to examine steady-state operation. Batch-style packed beds could potentially face challenges with hybrid solar/autothermal operation due to the extremely rapid kinetics of combustion. The second was to ensure long-enough residence times to allow for near-complete feedstock conversion. Entrained-flows or drop-tube reactors are problematic in this respect. A fluidized bed, however, would be able to meet both of these criteria. An indirectly-irradiated design was preferred to avoid the use of a window, which could have increased complications due to fouling in a process involving combustion. In addition, a relatively simple, familiar geometry was preferred for the opaque absorber, as the primary goal was to test the novel hybrid process. Therefore, a single tube within a cavity was selected as the geometry. The chosen design of the prototype reactor was very similar to the design used by Murray and Fletcher [48] with one key difference being the absorber material. Particle feeding to the bed allowed the introduction of feedstock to be modulated based on incoming solar irradiation.

5.3.2 Reactor Description

The primary materials of the reactor were chosen to be SiC for the emitter tube and Al_2O_3-SiO_2 for the insulation. The emitter tube was made of pressureless sintered SiC (Saint-Gobain Ceramics, Hexoloy SA) and had an inner diameter of 42 mm, an outer diameter of 52 mm, and length of 300 mm. Selected material properties of the SiC are given in Table 5.1. The high temperature limit, low coefficient of thermal expansion, high thermal conductivity, as well as high strength and chemical inertness make the material ideal for concentrated solar applications. The SiC tube was fabricated with a 45˚ 16.7-mm diameter angled hole in the back to allow for a feedstock delivery tube. The feedstock delivery tube was made of Al_2O_3 due to the chemical inertness, reduced thermal conductivity, and high melting point. The feedstock delivery tube was sealed and fastened into place using a high-temperature ceramic putty (Cotronics, Thermeez 7020). The emitter tube contained a bed of Al_2O_3 granules supported by a 72-mesh stainless steel screen.

The reactor cavity insulation was made of 25-50 mm-thick Al_2O_3-SiO_2 ceramic blocks (Zircar Zirconia, M-35 Buster, 80% Al_2O_3). Selected material properties of the Al_2O_3-SiO_2 are given in Table 5.1. The relatively low thermal conductivity, high melting point, and high emissivity in the IR-spectrum made it a suitable material for high-temperature insulation. The ceramic blocks were held in place using a stainless steel casing with dimensions of 210 × 215 × 275 mm. The front block contained a 40-mm diameter conical aperture with an acceptance angle of 45˚, and was cut into four pieces to reduce thermal stresses. The back block contained a 45˚ hole to allow the feedstock delivery tube to pass through.

Table 5.1 Material properties of SiC and Al_2O_3-SiO_2 [140, 141].

	Density ($g \cdot cm^{-3}$)	Max. service temperature (K)	Specific heat ($kJ \cdot kg^{-1} \cdot K^{-1}$)	Thermal expansion (10^{-6} K^{-1})	Thermal conductivity ($W \cdot m^{-1} K^{-1}$)
SiC	3.10	2173	0.67	4.0	77.5 (at 673 K)
Hexoloy SA					
Al_2O_3-SiO_2 M-35	0.56	1998	1.05	5.0	0.27 (at 1623 K)

Sheathed K-type thermocouple probes (OMEGA) were fed in from the top of the emitter tube and placed at two locations in the bed: one ~30 mm below the focal point at the tube center line (in contact with the inert bed) and one ~30 mm above the focal point at the tube center line (in the region where particles would be fluidized). Two more K-type thermocouples were placed on the outside of the emitter tube on the top and bottom to monitor the temperatures near the O-ring seals. Another thermocouple was initially placed on the inside of the tube at the focal point, but it had recurring issues due to degradation at high temperatures (>1573 K). A schematic showing the positions of the probes is provided in Figure 5.1. Continuous water cooling using coiled copper tubing was employed at the top and bottom of the emitter tube due to the high thermal conductivity of SiC.

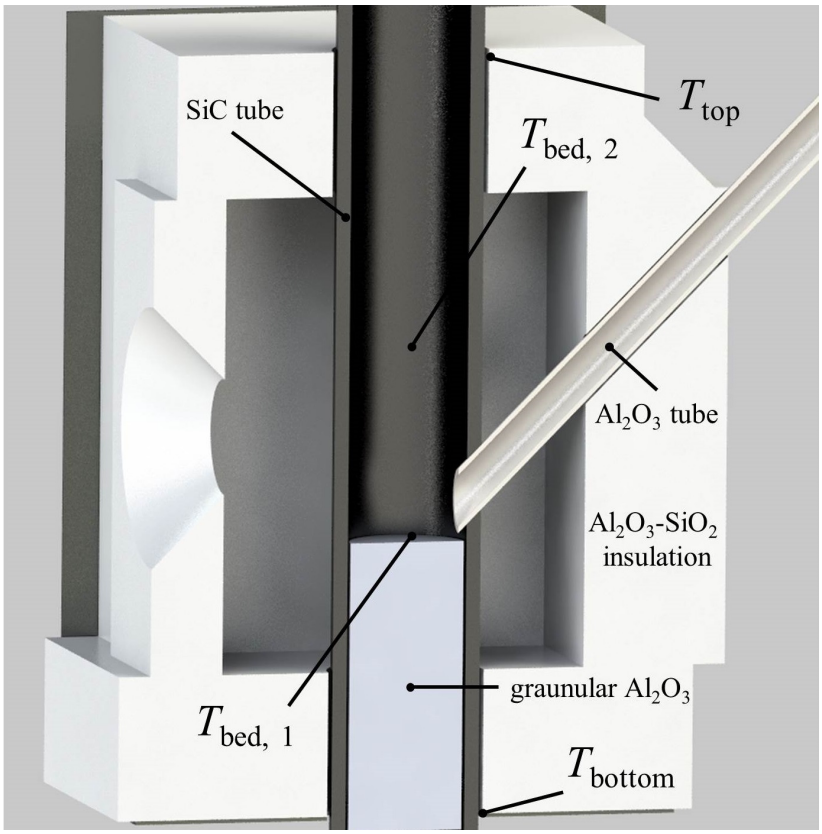

Figure 5.1 Schematic of reactor cross section with materials and thermocouple positions.

The rest of the reactor body was constructed out of stainless steel KF flanges and fittings, allowing for simple removal of the thermocouple feedthrough and cleaning. Seals between the emitter tube and flanges were made with steam-resistant Aflas O-rings. The outlet of the reactor diverged to a 51-mm inner diameter stainless steel tube to reduce gas velocity at the exit and allow entrained particles to disengage. The inlet of the reactor contained two K-type thermocouples at the tube centerline to monitor reacting gas temperature, and heat tape was wrapped around the stainless steel tubing to prevent the H_2O(v) from condensing before entering the fluidized bed. The reactor stand was made out of T-slotted aluminum extrusions and allowed the position of the reactor to be adjusted in the *x*-*z* plane. SolidWorks renderings of the reactor and stand are shown in Appendix A.

5.3.3 Feedstock & Bed Material Properties

The feedstock used for the HFSS experiments was untreated, laboratory-grade granular activated charcoal (Sigma-Aldrich, 20-60 mesh) derived from peat. A photo of the feedstock is shown in Figure 5.2a. BET analysis using nitrogen adsorption found the specific surface area to be 600-800 m^2/g [142]. Results from proximate and ultimate analyses are shown in Table 5.2.

Table 5.2 Proximate and ultimate analyses of activated charcoal derived from peat (values in weight % unless otherwise noted).

	Activated charcoal (granular)
Carbon	84.01
Hydrogen	0.90
Nitrogen	0.37
Oxygen (BD)	6.09
Sulfur	0.25
Ash	8.38
Moisture	3.74
Volatile matter	4.94
Fixed carbon	82.94
H/C [mol/mol]	0.128
O/C [mol/mol]	0.054
LHV [MJ/kg]	29.3

Table 5.2 shows a high carbon content, low moisture, and relatively high ash in the feedstock. Most of the carbon was fixed, indicative of the pre-pyrolysis process removing the volatiles. H, N, and S were present in very small amounts, and O was slightly higher. This led to very low H/C and O/C ratios. The LHV was calculated to be 29.3 MJ/kg based on correlations found in literature [143, 144]. The fused Al_2O_3 granules (Micron Metals, 99.9% purity, 30-50 mesh) were inert and non-cohesive, allowing them

to support any unreacted particles and partially fluidize in the bed. A photo of the Al_2O_3 granules is shown in Figure 5.2b. The low thermal conductivity of the material also allowed the reacting gases to be preheated before reaching the bed surface without transferring significant heat from the reaction zone to the stainless steel mesh.

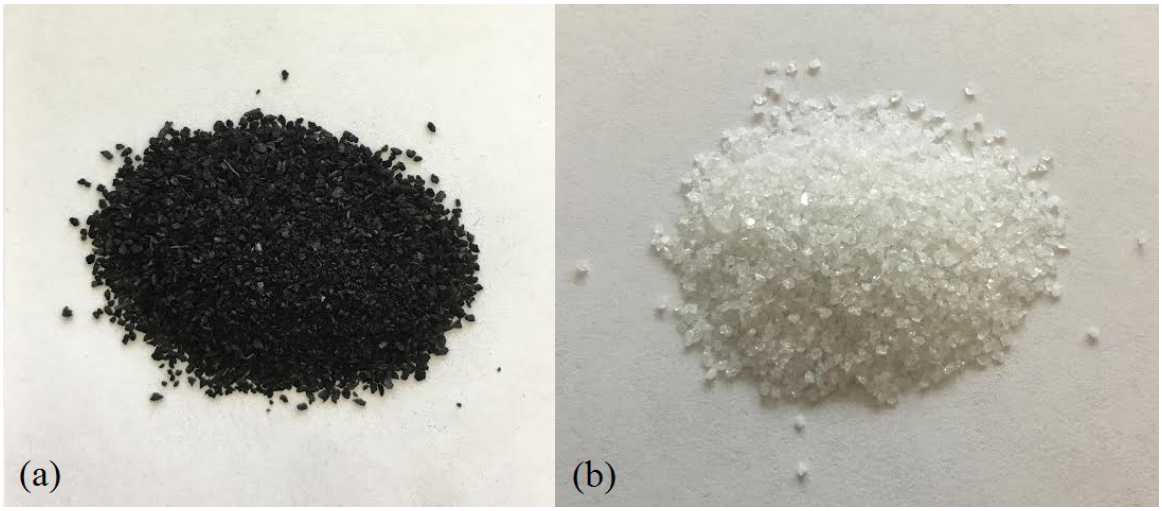

Figure 5.2 Photo of the (a) granular activated charcoal and (b) granular Al_2O_3 particles.

The fluidization properties for both the inert bed material and feedstock were estimated using various assumptions and correlations. A number of different fluidization regimes are possible including bubbling, turbulent, and fast regimes [145]. An analysis was performed in order to put bounds on the conditions that would lead to particle fluidization and entrainment. The well-known correlation by Ergun [146] was used to calculate minimum fluidization velocity, represented as:

$$u_{\mathrm{mf}} = \frac{\left(d_{\mathrm{p}}\psi\right)^2 \left(\rho_{\mathrm{s}} - \rho_{\mathrm{f}}\right) g}{150\mu_{\mathrm{f}}} \cdot \frac{\varepsilon_{\mathrm{mf}}^3}{\left(1-\varepsilon_{\mathrm{mf}}\right)} \tag{5.1}$$

where d_p is particle diameter, ψ is particle sphericity, g is the gravitational constant, μ_f is the dynamic viscosity of the fluid, ε_{mf} is the void fraction at minimum fluidization, and ρ_s and ρ_f are the densities of the solid and fluid, respectively. Solid and bulk densities were measured and calculated using water displacement or provided by the manufacturer. ψ was estimated to be 0.70 for both materials based on values reported in literature for similar materials [147, 148]. μ_f was estimated to be 62.81×10^{-6} Pa·s based on Ar at 1200 K and atmospheric pressure, provided in literature [149]. Ideal gases at 1200 K and atmospheric pressure and plug flow were assumed for the fluid phase. ε_{mf} was calculated using the correlation from Broadhurst and Becker [150]:

$$\varepsilon_{mf} = 0.586\psi^{-0.72}\left(\frac{\mu_f^2}{\rho_f g\left(\rho_s - \rho_f\right) d_p^3}\right)^{0.029}\left(\frac{\rho_f}{\rho_s}\right)^{0.021} \tag{5.2}$$

Reynolds number for particles at minimum fluidization is represented as:

$$Re_{mf} = \frac{\rho_f d_p u_{mf}}{\mu_f} \tag{5.3}$$

Knowing Re_{mf}, it is possible to apply a correlation to find terminal velocity, u_t, or the velocity at which particles are blown out of the bed. Minimum fluidization calculations showed that the Re_{mf} was less than 500 for all cases, which allowed the following correlations from Kunii and Levenspiel [151] to be applied:

$$u_t = \frac{g\left(\rho_s - \rho_f\right) d_p^2}{18\mu}, \; Re < 0.4 \tag{5.4}$$

$$u_t = d_p \left(\frac{0.0178 g^2 (\rho_s - \rho_f)^2}{\rho_f \mu} \right)^{1/3}, \; 0.4 < Re < 500 \tag{5.5}$$

From u_t and u_{mf}, corresponding volumetric flow rates for the tube geometry were calculated. The results from the fluidization calculations are shown in Table 5.3, and are presented in ranges based on the minimum and maximum particle diameter. It was observed that relatively low volumetric gas flows were necessary to begin to fluidize the charcoal particles in the tube (<5 L/min). While only very high velocities would entrain the inert bed material, 20.72 L/min of Ar flow would entrain the smallest activated charcoal particles out of the tube. The loss of these particles would be mitigated by both the larger reactor diameter and lower temperatures downstream of the emitter tube. However, as the charcoal particles react, they shrink during the reaction and are more likely to be entrained out of the tube. Therefore, an effort was made in the experimental design to keep the total gas flow towards the lower end of the 20.72-234.4 L/min range.

Table 5.3 Results from fluidization calculations.

	Granular Al_2O_3	Activated charcoal
Particle diameter (mm)	0.297-0.595	0.250-0.841
ρ_{bulk} (g/ml)	1.87	0.27
$\rho_{particle}$ (g/ml)	3.97	0.46
ε_{mf} (-)	0.50-0.55	0.56-0.62
u_{mf} (m/s)	0.068-0.177	0.009-0.064
Re_{mf} (-)	0.131-0.681	0.015-0.347
u_t (m/s)	3.034-6.058	0.249-2.820
$\dot{V}_{mf}$ (L/min)	5.66-14.71	0.75-5.31
$\dot{V}_t$ (L/min)	252.2-503.5	20.72-234.4

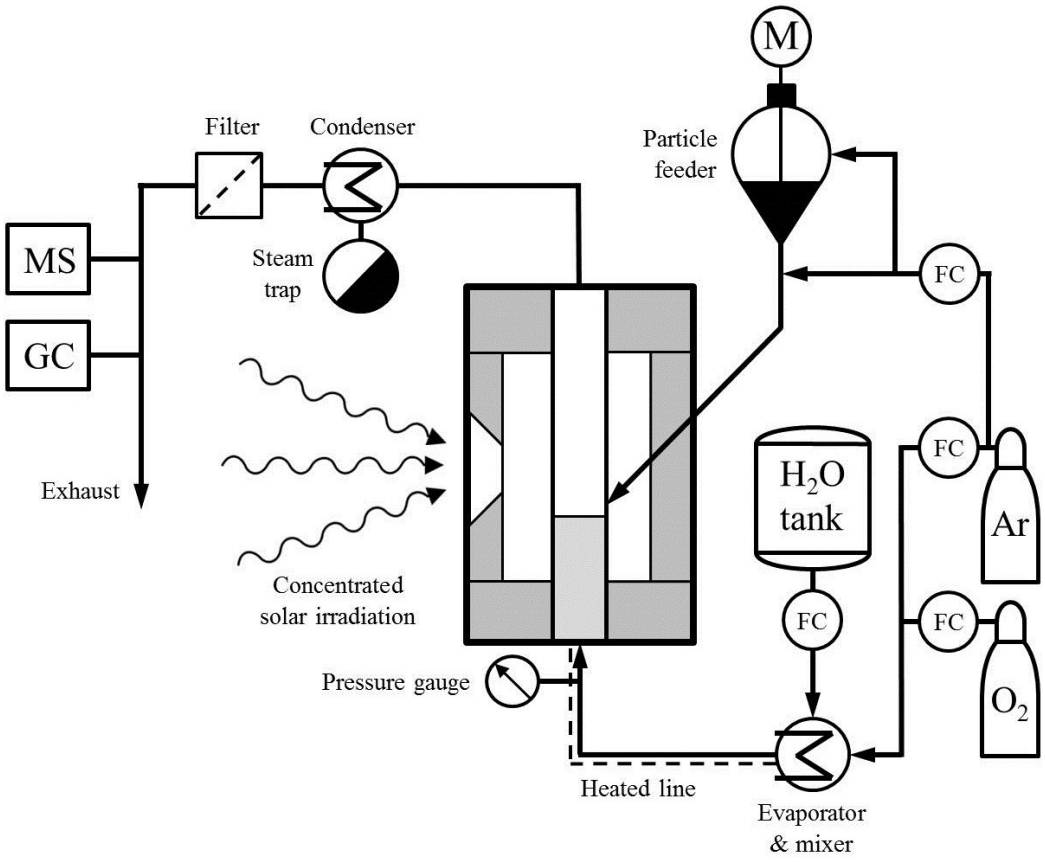

Figure 5.3 Schematic of reactor setup including instrumentation.

5.4 Instrumentation

A schematic of the reactor setup is shown in Figure 5.3. Ar and O_2 flow rates were controlled using mass flow controllers (Bronkhorst, EL-FLOW). A pressurized tank and liquid flow controller (Bronkhorst, Mini CORI-FLOW) delivered H_2O to an evaporator (Bronkhorst, CEM), where it was mixed with the reacting gas flow. The particle feeder (LAMBDA Instruments, DOSER) was purged with Ar in the feedstock vessel and just below the feeder at a constant rate of 2 L_N/min to prevent backflow of reacting gases. The

feeder was calibrated with the purge Ar to a feeding rate of 57.5 ± 2.7 g/h using three 15 min experiments. A pressure gauge below the bed was used to monitor the pressure inside of the reactor. The gas stream leaving the reactor passed through dry ice to condense out the water vapor from the flow, and a particle filter was installed to remove particles greater than 40 μm. Product gases were temporally monitored with mass spectrometry (MS, OmniStar ThermoStar GSD320 Gas Analysis System) and gas chromatography (GC, Agilent 490 Micro GC equipped with Molsieve and PoraPLOT Q columns). The GC was calibrated for H_2, CO, CO_2, CH_4, and O_2.

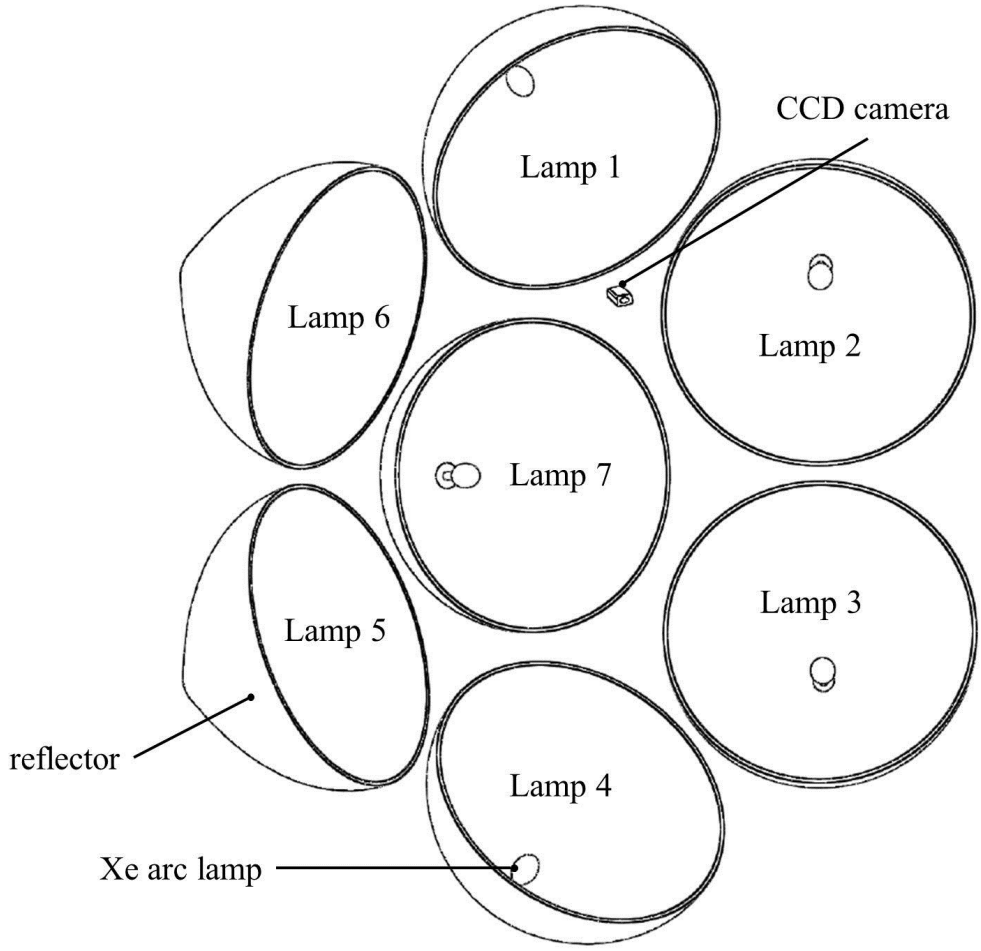

Figure 5.4 Schematic of the HFSS. The position of the CCD camera is displayed, and lamps are labeled as shown.

A schematic of the HFSS is shown in Figure 5.4. Seven xenon arc lamps close-coupled to truncated ellipsoidal reflectors comprised the HFSS, and individual lamp power were able to be adjusted between 3-5.5 kW_e. The lamps were all focused on a circular area ~40 mm in diameter. A CCD camera allowed for the calibration of the lamps through mapping of reflections on a Lambertian target. The setup and characterization of the simulator is described in detail by Gill *et al.* [132]. Using all seven lamps, the average and peak radiative heat fluxes over a 40 mm diameter were 4880 ± 223 kW/m^2 and 6834 kW/m^2, respectively. Least squares analysis found electrical power

to radiation conversion efficiency to be 0.537 ± 0.004. The aperture of the reactor was aligned at the focal plane using laser levels. Each lamp created strongly localized heat fluxes near the focus, so it was necessary to turn lamps on sequentially to prevent excessive thermal shocks to the system.

In order to calibrate the simulator, several tests were run with a Lambertian reflector aligned in the focal plane instead of the reactor aperture. Lamps were set to the same powers that they were during experiments, and images of the target were taken using a CCD camera with an ND filter. Images of the two heat-up states and the final state were captured and time averaged for 1 min. Four sets of images were taken for the final state with readjustment of lamp power to account for operator error in setting power levels. Previous calibration of the simulator used calorimetry to produce a correlation to relate electrical potential from the camera to a heat flux, correcting for image distortion. Total power entering the aperture was obtained by using image-processing software to identify the reactor aperture in an image and overlay it with the flux map, and was found to be 1371.2 ± 6.4 W. Figure 5.5 shows a representative flux map at the aperture during steady state, with heat fluxes given in kW/m^2. Peak fluxes of ~1400 kW/m^2 were observed at the center of the aperture area, with fluxes decreasing to between 600-1000 kW/m^2 at the edges of the aperture area. Higher flux concentrations were observed at the top of the aperture area, likely due to the use of the top lamp. The radiation entering the aperture would be more diffuse upon reaching the emitter tube.

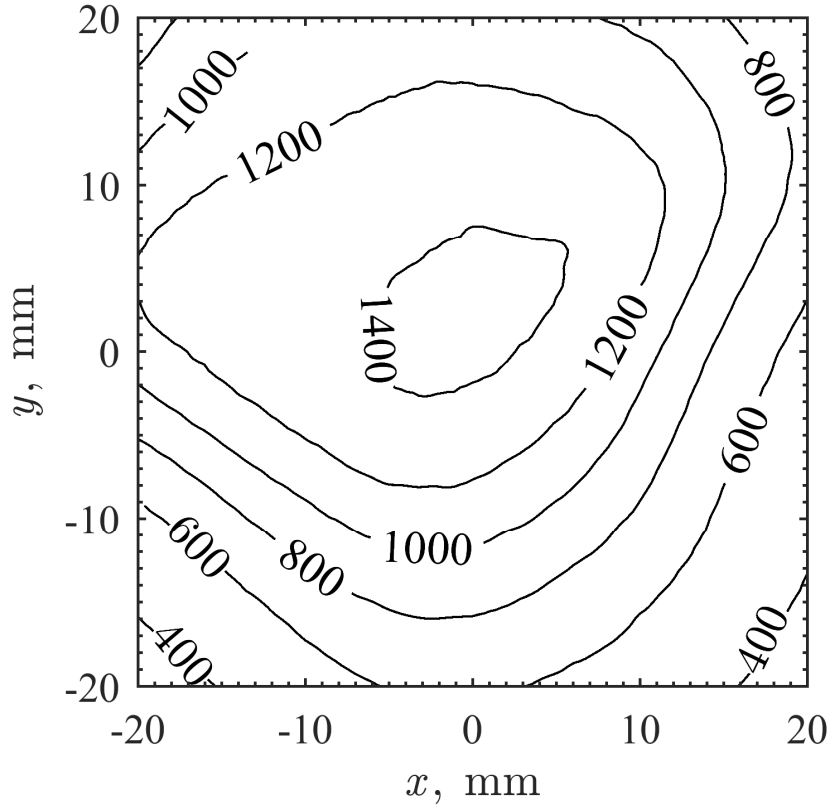

Figure 5.5 Representative flux map for the total power entering the aperture area during steady state. Heat fluxes are given in kW/m^2.

5.5 Data Acquisition

Temperatures, gas flow rates, and lamp powers and settings were monitored using a LabVIEW program (see Appendix B), which recorded data points approximately every 2 s. Feeder on/off setting, water vapor flow rate, and evaporator temperature were controlled and monitored manually. A digital readout unit (Bronkhorst, E-8000) interfaced with the evaporator and liquid flow controller. Reactor pressure was monitored and periodically recorded manually. MS and GC data were recorded using separate software programs. The GC method had a 1.5 min elution time, resulting in one measurement taken approximately every 2 min.

5.6 Summary

An indirectly-irradiated fluidized bed reactor was designed and fabricated to allow for continuous gasification of carbonaceous materials. The scale of the reactor was designed for use in a 6-kW HFSS. The body of the reactor consisted of a SiC tube with an Al_2O_3 inert bed placed within an Al_2O_3-SiO_2 cavity. O_2 and H_2O(v) could be fed into the reactor simultaneously at specified rates, in addition to feedstock particles. Ar was used as the inert balance gas to allow for the adjustment of volumetric concentrations and total flow rates. K-type thermocouples were placed in several locations of the reactor to monitor temperatures. Calculations were performed to estimate fluidization properties of the feedstock and inert bed material. HFSS radiative input was calculated at the experimental conditions using calibrated images of a Lambertian reflector target. Product gas analysis was performed using GC and MS, and LabVIEW software was used to acquire and record data.

CHAPTER 6. REACTOR TESTING & RESULTS

6.1 Introduction

After the design and fabrication of the prototype reactor, the final step was "on-sun" testing the reactor under a set of approximately steady-state conditions. This required a consistent experimental procedure to bring the reactor to temperature and gasify a constant flow of feedstock. This chapter describes the experimental procedure for testing in the HFSS and the various conditions under which the reactor was tested, including equilibrium calculations to give predicted product gas molar compositions. The results of the experimentation are presented and analyzed using two-way ANOVA. Implications of the results are discussed and compared with existing experimental solar gasification campaigns.

6.2 Experimental Procedure and Conditions

Following a setup of the instrumentation and series of shakedown tests, a consistent protocol was closely adhered to for each experiment. The experimental protocol was carried out as follows. Ar flow was initiated according to the experimental conditions. The evaporator was heated to 473 K, and the heat tape around the gas line to the reactor was turned on. Cooling water flow was introduced to the top and bottom of the emitter tube. The center lamp (Lamp 7) was then turned on at approximately three quarters of full power. After 10 min, the top lamp (Lamp 1) was turned on at close to full power. At 23 min, Lamp 7 was increased to close to full power. After the temperatures reached an approximate steady state (30 min), H_2O was introduced to the system at the desired level

depending on the experiment. After 35 min, charcoal feeding began at a rate of 57.5 g/h. For the experiments without O_2 flow, charcoal feeding proceeded for 15 min to allow the system to reach quasi-steady state conditions. For the experiments with O_2 flow, 0.5 L_N/min O_2 was added after 2 min of charcoal feeding and the system was again allowed to reach a steady state for 15 min. After the 15 min, O_2, H_2O, and charcoal feeding were stopped and the lamps were turned off. The gas temperature at the inlet of the reactor was ~410 K during steady-state operation. Ar continued to flow until the reactor reached sufficiently-cool temperatures. Measurements were taken using the GC throughout. Due to a technical issue with the MS, it was only available during the experiments with O_2. Gauge pressure in the reactor varied between 0-20 kPa depending on the stage of the experiment. Ash and residual charcoal particles were vacuumed out of the reactor between each experiment and the inert bed was adjusted to its original height.

Table 6.1 Experimental conditions for "on-sun" testing (concentrations of total gas flow including feeder purge are given in parentheses).

	Low H_2O	High H_2O
Low O_2	84.3 g/h H_2O (23.3%) 0 L_N/min O_2 (0%) 3.75 + 2 L_N/min Ar (76.7%)	168.6 g/h H_2O (46.6%) 0 L_N/min O_2 (0%) 2 + 2 L_N/min Ar (53.4%)
High O_2	84.3 g/h H_2O (23.3%) 0.5 L_N/min O_2 (6.7%) 3.25 + 2 L_N/min Ar (70.0%)	168.6 g/h H_2O (46.6%) 0.5 L_N/min O_2 (6.7%) 1.5 + 2 L_N/min Ar (46.7%)

Experimental conditions are given in Table 6.1, which shows the 2^2 experimental design. Two replicates of each experiment were run, resulting in eight total experiments. Feeder purge Ar flow for each experiment was 2 L_N/min, but reactor inlet flows of Ar changed to keep total volumetric flow rate consistent. Total Ar concentration was

maintained at ~50% or greater to keep product gases relatively dilute. Total gas flow was 7.5 L_N/min for each experiment. For bed temperatures of 1200 K, the gas experienced over a fourfold increase in volume from normal conditions, assuming ideal gases. A thermocouple placed at the tube outlet centerline during one of the experiments measured an approximate steady-state temperature of ~900 K prior to particle feeding. Recalculating u_t for the smallest charcoal particles (0.250 mm) given Ar properties at 900 K and 101325 Pa produced $\dot{V}_t$ = 25.2 L/min for the tube. Assuming ideal gas behavior at 900 K, the total volumetric flow rate would be 24.7 L/min: just below $\dot{V}_t$. This led to entrainment of some of the smaller charcoal particles, which could be observed in the outlet flange after each experiment in amounts of a few grams or less.

The H_2O levels were chosen such that the H_2O:C ratio would be greater than stoichiometric for solar-only gasification. For the low H_2O experiments (84.3 g/h), the H_2O:C ratio was 1.16, and for the high H_2O experiments (168.6 g/h), the H_2O:C ratio was 2.32. The O_2 levels were chosen such that only a small portion of the feedstock would be combusted. No O_2 was introduced for the low O_2 level (solar-only), and only 0.5 L_N/min O_2 was introduced for the high O_2 (combined solar/autothermal). This corresponded to an O_2:C ratio of 0.33, meaning that approximately one-third of the feedstock would be combusted. H_2O condensed out of the product gas stream ranged between ~10-30 ml depending on experimental conditions.

Expected product gas molar compositions based on chemical equilibrium at atmospheric pressure are shown in Figure 6.1. H_2O was assumed to be condensed out and was not included in the figure. Ar was not included in the figure, but was included in the

calculations in the form of reduced partial pressures based on inlet gas concentrations. As described in Section 2.3, the introduction of O_2 leads to an increase in CO_2 and a decrease in H_2 and CO. Higher H_2O leads to greater production of H_2 and CO_2 due to increased carbon gasification and water-gas shifting of products. Very low CH_4 is predicted above temperatures of 1000 K for all conditions. The introduction of O_2 leads to lower C predicted at lower temperatures. For all conditions, higher temperatures above 1000 K leads to a decrease in H_2:CO ratio. The greatest syngas output can be expected from the low O_2 conditions, with H_2O level affecting H_2:CO ratio.

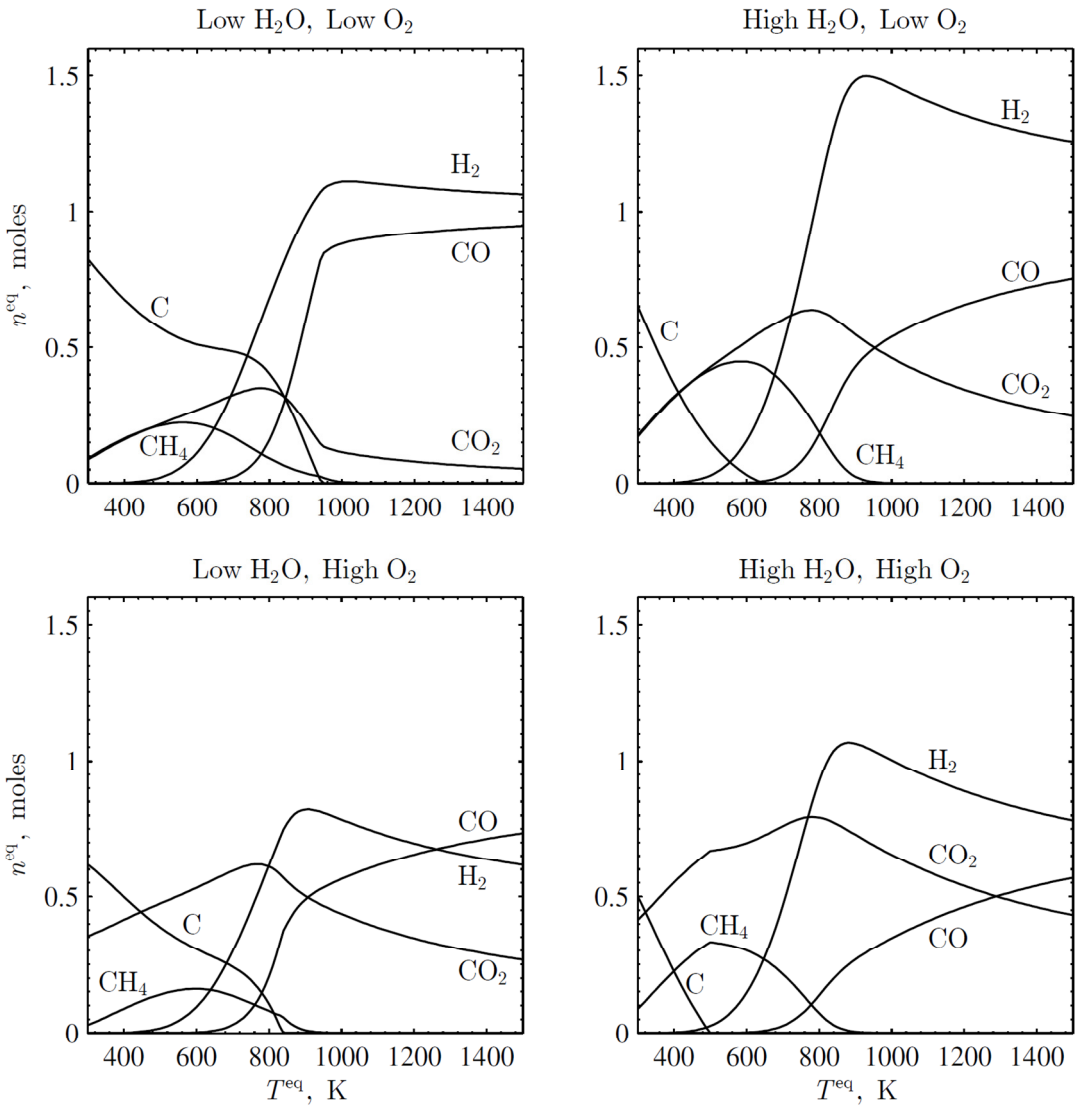

Figure 6.1 Equilibrium compositions as a function of temperature for the four conditions shown in Table 6.1, normalized to 1 mole of feedstock (activated charcoal derived from peat).

6.3 Results

Representative runs are shown in Figure 6.2 and Figure 6.3 for a low and high O_2 condition, respectively. Figure 6.2a shows temporal temperatures, concentrated solar irradiation entering the aperture, and Figure 6.2b shows product gas molar flows for a low O_2, high H_2O run. The surface of the inert bed reached ~1230 K prior to charcoal

feeding. After the charcoal feeding commenced, the temperature at the surface of the bed ($T_{bed,1}$) dropped to ~1150 K, owing to the strongly-endothermic gasification reactions taking place. The temperature ~60 mm above the surface of the bed ($T_{bed,2}$) stayed relatively constant at ~1170 K. This indicates that there were likely particles that settled on the surface of the bed that were undergoing conversion. After charcoal feeding stopped, the $T_{bed,1}$ began to rise again.

The associated product gas molar flows from GC showed a rapid rise in H_2, CO, and CO_2 after charcoal feeding began. Negligible CH_4 was observed, and no O_2 was detected during any of the runs. Small amounts of H_2 and CO were generated prior to charcoal feeding, likely due to residual charcoal particles in the bed. The gas composition began to level off ~7 min after charcoal feeding began. It was observed that while the relative amounts of H_2, CO, and CO_2 were similar to those predicted at equilibrium, the relative amount of H_2 is less than what equilibrium predicts. This observation points to a potential kinetic or mass transfer limitation.

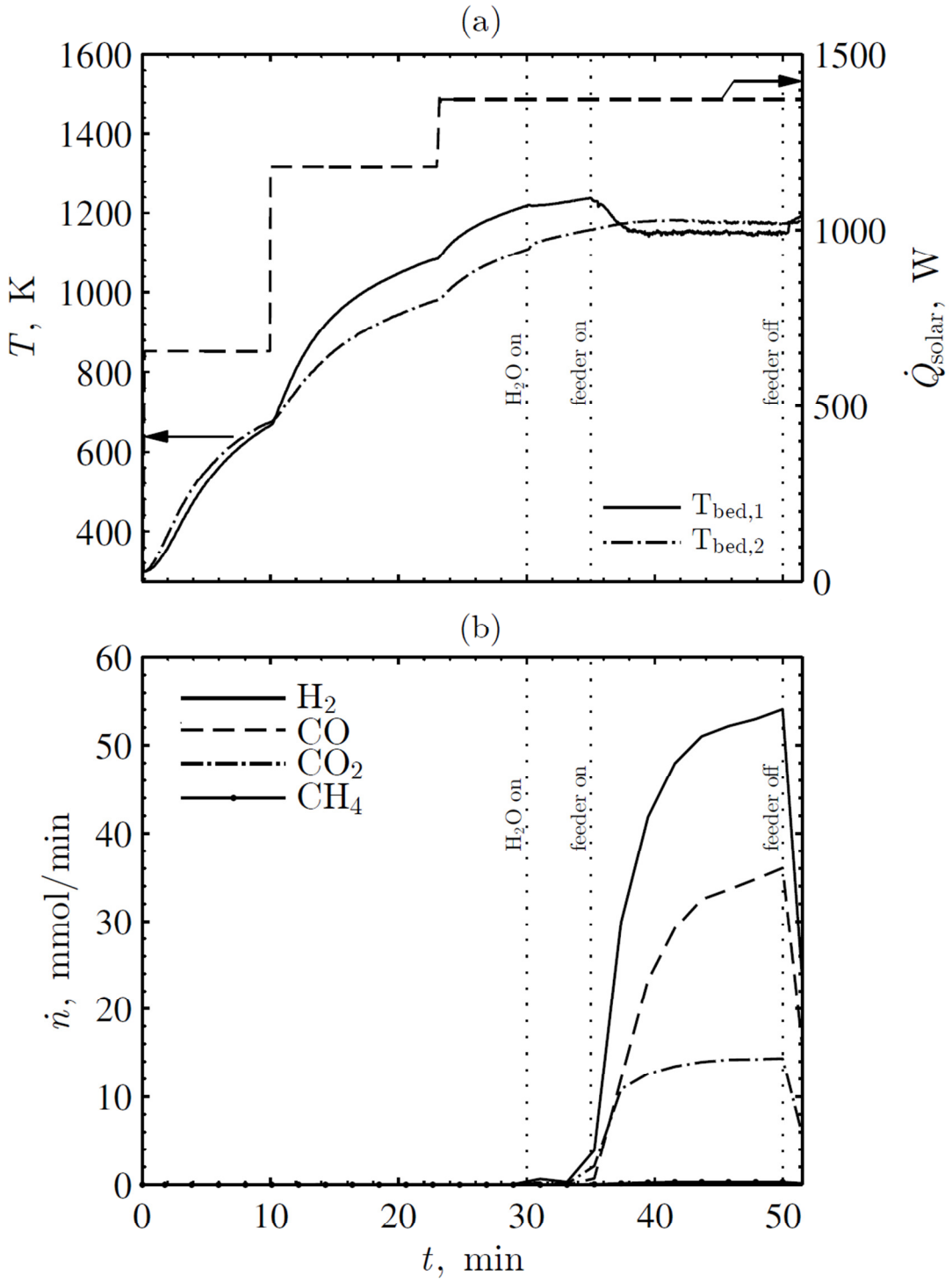

Figure 6.2 Representative run for a low O_2 (solar-only) condition. Run shown uses the high level of H_2O. (a) Temporal bed temperatures and solar energy entering aperture and (b) temporal product gas molar flows from GC.

The representative high O_2 run shown in Figure 6.3 was at the low H_2O condition. Heat up showed conditions similar to those in Figure 6.2a, including the initial temperature drop after the introduction of charcoal particles. However, once O_2 was introduced, there was a marked increase in the bed temperatures. Prior to charcoal feeding, the $T_{bed,1}$ was at ~1240 K, but it reached temperatures of ~1410 K after O_2 was introduced. $T_{bed,2}$ did not show as drastic of an increase, but a temperature rise of ~100 K was observed. As with the low O_2 run, this indicates that most of the reactions were concentrated at the surface of the bed. Unlike with the low O_2 runs, some ash melting was observed on the surface of the bed during reactor cleaning. After O_2 flow stopped, $T_{bed,1}$ began to fall.

Product gases exited the emitter tube at temperatures of up to ~925 K during a high H_2O, high O_2 run, indicating a possible area for sensible heat recovery and improved efficiencies. Based on thermophysical property data from literature [60], the enthalpy that could be captured from bringing the product gases to room temperature (excluding H_2O, whose molar amount in the products is unknown) was 62 W. This corresponded with 4.5% of the solar input entering the reactor from a first-law analysis.

The associated product gas molar flows again showed a rapid rise in H_2, CO, and CO_2 after charcoal feeding began. Negligible CH_4 was observed. After O_2 was introduced, H_2 and CO decreased, and then slowly began to rise again. The product gases reached an approximate steady state ~5 min after O_2 flow began. As expected from equilibrium compositions, a larger amount of CO_2 was observed as compared to the low O_2 runs and H_2:CO ratio was less than 1. This could be an effect of kinetically-rapid

combustion reactions or the reverse water-gas shift reaction taking place downstream of the reaction zone prior to product gas sampling at lower temperatures.

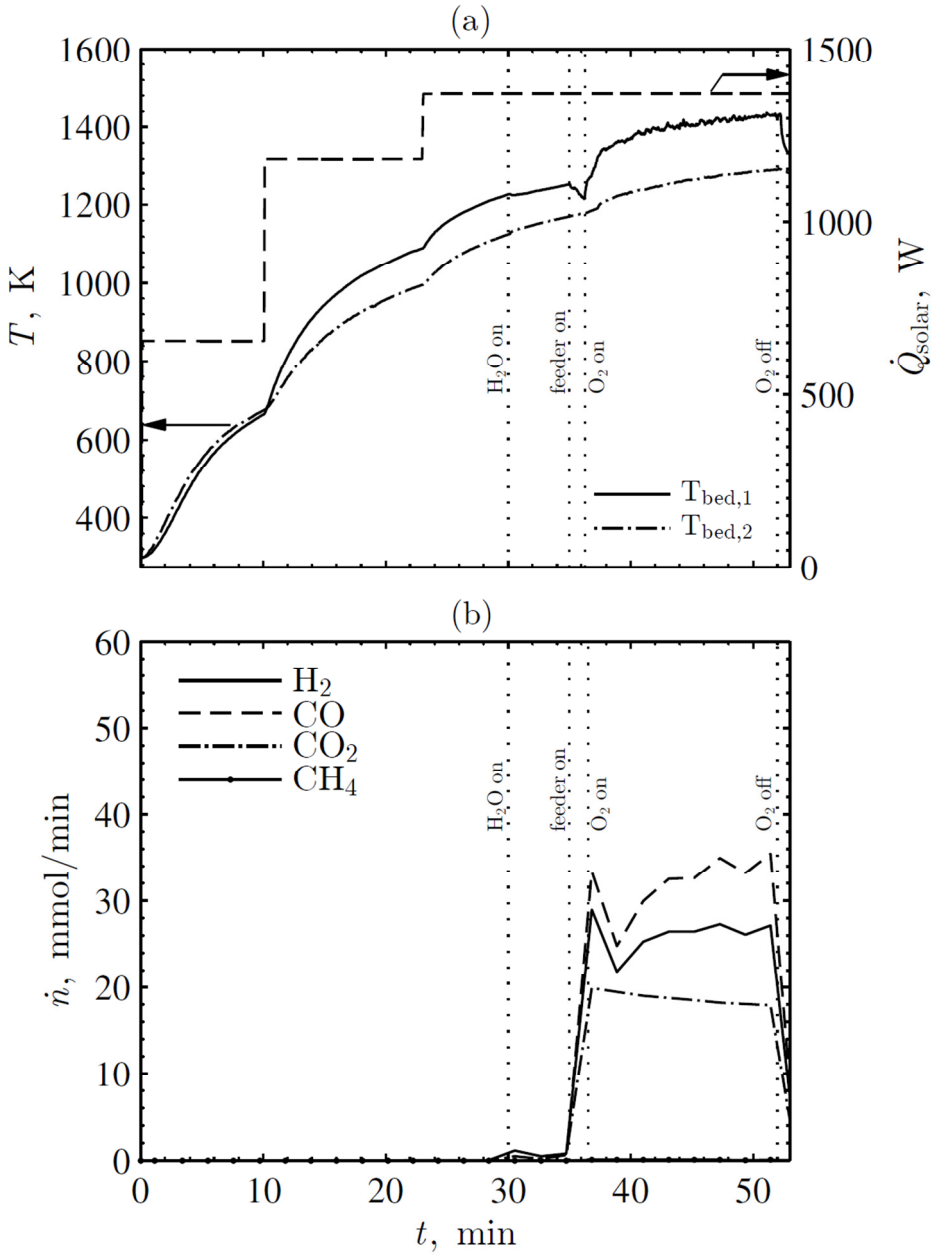

Figure 6.3 Representative run for a high O_2 (combined solar/autothermal) condition. Run shown uses the low level of H_2O. (a) Temporal bed temperatures and solar energy entering aperture and (b) temporal product gas molar flows from GC.

Steady-state results from each run are given in Table 6.2. Molar flows and temperatures were time-averaged over the period of approximate steady state. Average carbon conversion was calculated as:

$$\overline{X} = \frac{\overline{\dot{n}}_{CO} + \overline{\dot{n}}_{CO_2}}{\overline{\dot{n}}_{C}} \tag{6.1}$$

where $\overline{\dot{n}}_i$ represents the time-averaged molar flow of product *i* over the period of approximate steady state. $\overline{\dot{n}}_C$ was calculated based on the known feedstock composition and mass flow rate of the particle feeder. Average cold gas ratio, $\overline{R}$, was calculated as in Equation 2.13 using converted feedstock in the denominator. LHV of H_2 and CO were 120.0 and 10.1 MJ/kg, respectively. Average solar-to-fuel efficiency, $\overline{\eta}_{\text{solar-to-fuel}}$, was calculated as in Equation 2.14 using converted feedstock in the denominator.

Table 6.2 Results for the eight "on-sun" runs completed.

	Low H_2O Low O_2		Low H_2O High O_2		High H_2O Low O_2		High H_2O High O_2	
H_2O:C (-)	1.16	1.16	1.16	1.16	2.32	2.32	2.32	2.32
O_2:C (-)	0	0	0.33	0.33	0	0	0.33	0.33
$\overline{\dot{n}}_{H_2}$ (mmol/min)	42.8	41.8	26.9	26.7	51.9	52.6	28.5	30.3
$\overline{\dot{n}}_{CO}$ (mmol/min)	35.4	34.1	33.6	33.7	30.9	34.3	23.7	24.1
$\overline{\dot{n}}_{CO_2}$ (mmol/min)	8.0	8.0	18.9	18.3	15.1	14.2	22.8	23.4
$\overline{\dot{n}}_{CH_4}$ (mmol/min)	0.2	0.2	0.1	0.1	0.3	0.3	0.1	0.1
$\overline{H_2:CO}$ (-)	1.21	1.23	0.80	0.79	1.68	1.54	1.20	1.26
$\overline{T}_{bed,1}$ (K)	1240	1191	1365	1414	1204	1150	1387	1381
$\overline{T}_{bed,2}$ (K)	1191	1174	1243	1272	1207	1176	1274	1271
$\overline{X}$ (-)	0.65	0.63	0.78	0.78	0.69	0.72	0.69	0.71
$\overline{R}$ (-)	1.12	1.12	0.73	0.74	1.11	1.11	0.70	0.71
$\overline{\eta}_{\text{solar-to-fuel}}$ (-)	0.20	0.20	0.15	0.15	0.21	0.22	0.13	0.14

Results showed good reproducibility between replicates and clear effects of reacting gas composition on product gas composition, temperature, conversion, cold gas ratio, and solar-to-fuel efficiency. In order to more closely examine the main and interaction effects on each parameter, a series of ANOVA were performed using R statistical computing software [152] and interaction plots were created [153].

6.3.1 Effect on Bed Temperature

$\overline{T}_{bed,1}$ is a key parameter in the control of a hybrid solar/autothermal process. If temperatures are able to be controlled using O_2 in response to solar transients, continuous reactor operation will be possible regardless of solar conditions. An ANOVA was performed on the data considering the two treatments effects (H_2O:C ratio and O_2:C ratio) and their interaction on $\overline{T}_{bed,1}$. The results are given in Table 6.3. The ANOVA table provides strong evidence that O_2:C had a significant effect on $\overline{T}_{bed,1}$ ($P < 0.001$). The H_2O:C treatment and the interaction did not have significant effects on $\overline{T}_{bed,1}$. This agrees with the expectation that O_2 will tend to raise bed temperatures due to strongly-exothermic combustion reactions.

Table 6.3 ANOVA table comparing the effects and interaction of H_2O:C and O_2:C on $\overline{T}_{bed,1}$.

	df	SS	MS	F	P (>F)
H_2O:C	1	966	966	1.023	0.3691
O_2:C	1	72531	72531	76.79	0.0009
H_2O:C×O_2:C	1	543	543	0.575	0.4905
Error	4	3778	945		
Total	7	77818			

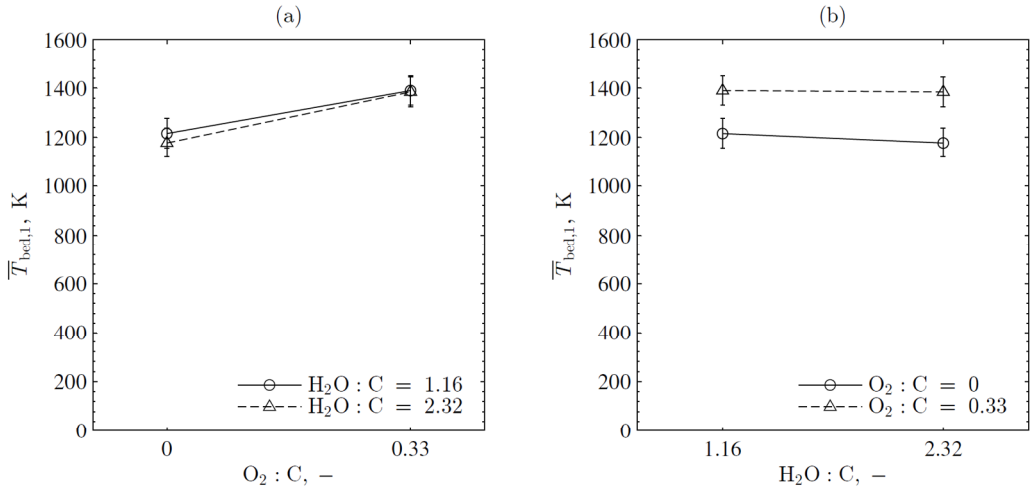

Figure 6.4 (a) H_2O:C-against-O_2:C and (b) O_2:C-against-H_2O:C interaction plots for $\overline{T}_{bed,1}$ means. Low and high levels are shown using circles and triangles, respectively, with error bars based on 95% confidence limits.

Interaction plots of $\overline{T}_{bed,1}$ means are shown in Figure 6.4a and Figure 6.4b with error bars based on 95% confidence limits [154]. There is a clear positive correlation between O_2:C and $\overline{T}_{bed,1}$ shown in Figure 6.4a for both H_2O:C conditions. No interactions were observed, and the parallel horizontal lines in Figure 6.4b indicate that H_2O:C did not have a significant effect on $\overline{T}_{bed,1}$. Variances in $T_{bed,1}$ were possibly due to highly localized temperature fluctuations resulting from endothermic or exothermic reactions, as particles and reacting gases have constantly-changing distributions in a fluidized bed.

6.3.2 Effect on H_2:CO Ratio

H_2:CO ratio is an important metric in gasification due to F-T synthesis requiring a particular H_2:CO ratio. As mentioned previously, the optimal ratio of H_2:CO can vary between 1.7-2.15 depending on the type of catalyst used. Product gases could be water-gas shifted downstream of the reactor to tune the H_2:CO ratio, which would consume CO

and produce CO_2. An ANOVA was performed on the data considering the two treatments effects and their interaction on $\overline{H_2{:}CO}$ ratio. The results are given in Table 6.4. The results provide strong evidence that both H_2O:C and O_2:C had a significant effect on $\overline{H_2{:}CO}$ ($P < 0.001$). The interaction did not have a significant effect on $\overline{H_2{:}CO}$.

Table 6.4 ANOVA table comparing the effects and interaction of H_2O:C and O_2:C on $\overline{H_2{:}CO}$.

	df	SS	MS	F	P (>F)
H_2O:C	1	0.340	0.340	114.9	0.0004
O_2:C	1	0.324	0.324	109.4	0.0005
H_2O:C×O_2:C	1	0.001	0.00101	0.342	0.5902
Error	4	0.012	0.00296		
Total	7	0.677			

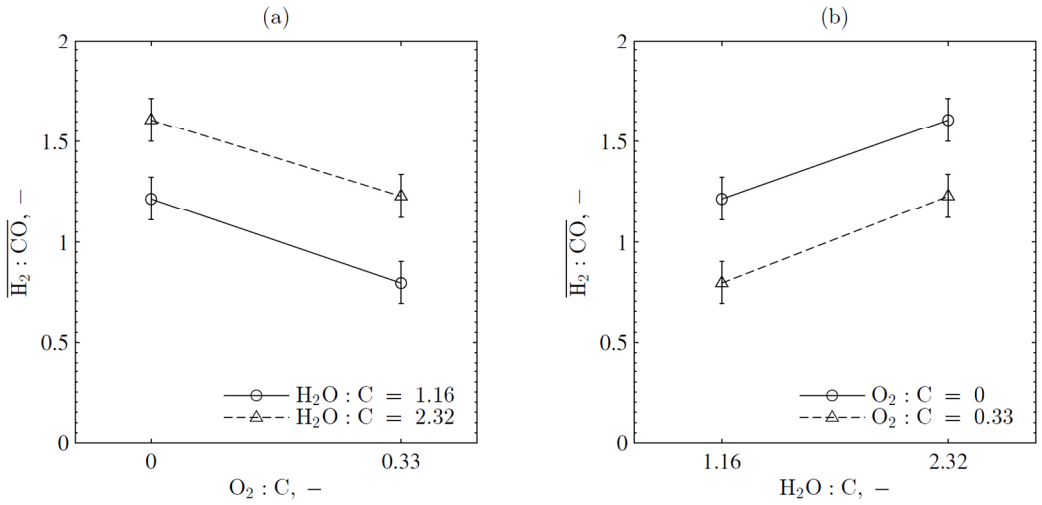

Figure 6.5 (a) H_2O:C-against-O_2:C and (b) O_2:C-against-H_2O:C interaction plots for $\overline{H_2{:}CO}$ means. Low and high levels are shown using circles and triangles, respectively, with error bars based on 95% confidence limits.

Interactions plots of $\overline{H_2:CO}$ means are shown in Figure 6.5a and Figure 6.5b with error bars based on 95% confidence limits. The negative correlation between O_2:C and $\overline{H_2:CO}$ for both H_2O:C conditions can be seen in both plots. This agrees with the equilibrium plots in Figure 6.1, which show significantly diminished H_2 production for the high O_2:C conditions. Equilibrium also predicts the $\overline{H_2:CO} < 1$ result for the high O_2:C, low H_2O:C condition. The plots also show the positive correlation between H_2O:C and $\overline{H_2:CO}$ for both O_2:C conditions. Again, this agrees with the equilibrium plots, showing that increased H_2O leads to greater H_2 production due to the water-gas shift reaction. It is clear that there was not a significant interaction effect on $\overline{H_2:CO}$.

6.3.3 Effect on Carbon Conversion

Maximizing feedstock conversion is a goal of all thermochemical conversion processes, as unconverted feedstock leads to inefficiencies in the system adds to material processing costs. An ANOVA was performed on the data considering the two treatments effects and their interaction on $\bar{X}$. The results are given in Table 6.5. There is strong evidence that O_2:C had an effect on $\bar{X}$ ($P < 0.01$), and that there were interactions between H_2O:C and O_2:C ($P < 0.01$). There is little evidence to suggest that H_2O:C had an effect on $\bar{X}$.

Table 6.5 ANOVA table comparing the effects and interaction of H_2O:C and O_2:C on $\bar{X}$.

	df	SS	MS	F	P (>F)
H_2O:C	1	0.0001	0.0001	0.529	0.5072
O_2:C	1	0.0091	0.0091	42.88	0.0028
H_2O:C×O_2:C	1	0.0105	0.0105	49.47	0.0022
Error	4	0.0009	0.0002		
Total	7	0.0206			

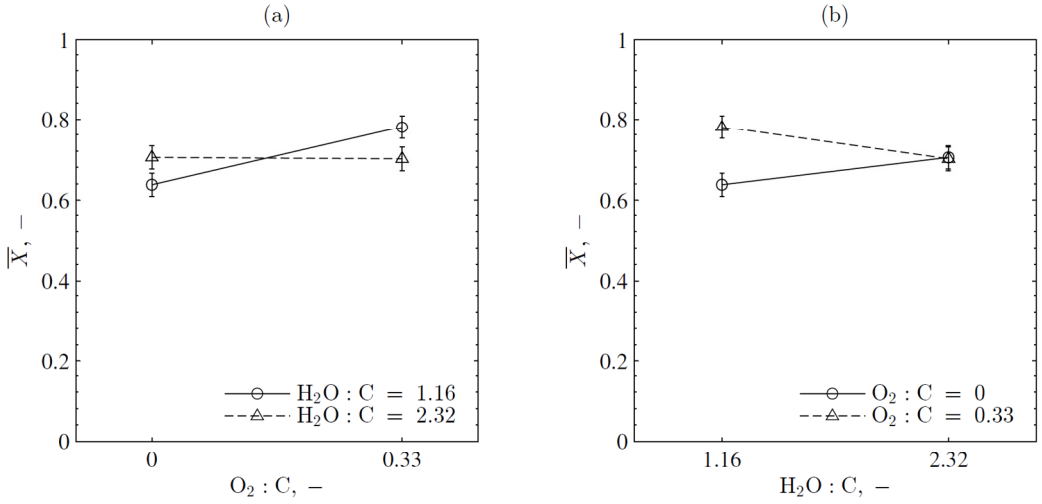

Figure 6.6 (a) H_2O:C-against-O_2:C and (b) O_2:C-against-H_2O:C interaction plots for $\overline{X}$ means. Low and high levels are shown using circles and triangles, respectively, with error bars based on 95% confidence limits.

Interaction plots of $\overline{X}$ means are shown in Figure 6.6a and Figure 6.6b with error bars based on 95% confidence limits. The plots show the interaction between the main effects. As can be seen in Figure 6.6a, O_2:C had a notable effect on $\overline{X}$ for the low H_2O:C condition, but not the high H_2O:C condition. Figure 6.6b displays the antagonistic interaction between H_2O:C and O_2:C, which shows that $\overline{X}$ increased with H_2O:C for the low O_2:C condition, but decreased with H_2O:C for the high O_2:C condition. This was a somewhat unexpected result, and could point to a complex interaction between O_2, C, and the product gases. If the O_2 reacted preferentially with fuels in the gas phase, it may have left more of the solid feedstock unconverted.

6.3.4 Effect on Cold Gas Ratio

Cold gas ratio is a metric that describes the energy content of the syngas as compared to the converted feedstock. It is therefore a critical performance metric in the operation of a

hybrid solar/autothermal system. During solar operation, the cold gas ratio should be greater than 1, indicating the storage of solar energy in the gaseous products. During autothermal operation, the cold gas ratio will drop below 1, indicating a net loss in the heating value of the fuel. However, a system with a cold gas ratio below 1 may still be useful as the produced fuel is in a more versatile and transportable form. An ANOVA was performed on the data considering the two treatments effects and their interaction on $\overline{R}$. The results are shown in Table 6.6. There is strong evidence that H_2O:C had an effect on $\overline{R}$ ($P < 0.01$) and O_2:C had an effect on $\overline{R}$ ($P < 0.0001$). There is also evidence to suggest a possible interaction between H_2O:C and O_2:C on $\overline{R}$ ($P < 0.05$).

Table 6.6 ANOVA table comparing the effects and interaction of H_2O:C and O_2:C on $\overline{R}$.

	df	SS	MS	F	P (>F)
H_2O:C	1	0.0008	0.0008	32	0.0048
O_2:C	1	0.3121	0.3121	12482	4e-08
H_2O:C×O_2:C	1	0.0002	0.0002	8	0.0474
Error	4	0.0001	0.00003		
Total	7	0.3132			

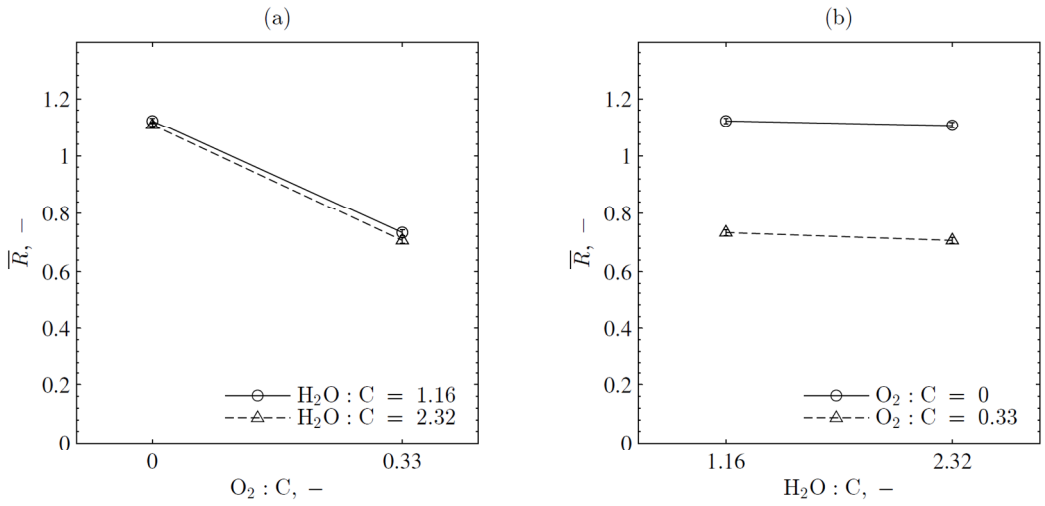

Figure 6.7 (a) H_2O:C-against-O_2:C and (b) O_2:C-against-H_2O:C interaction plots for $\overline{R}$ means. Low and high levels are shown using circles and triangles, respectively, with error bars based on 95% confidence limits.

Interactions plots of $\overline{R}$ means are shown in Figure 6.7a and Figure 6.7b with error bars based on 95% confidence limits. The plots show the significant negative effect of increased O_2:C on $\overline{R}$. While the ANOVA table shows that H_2O:C had a significant effect on $\overline{R}$, it is clear from the interaction plots that it was far less pronounced than the O_2:C effect. The decrease in $\overline{R}$ with O_2:C was expected due to the greater conversion of the feedstock to CO_2, which does not contribute to the syngas energy content at all. The slight decline in $\overline{R}$ with H_2O:C was somewhat unexpected, as more H_2 was produced with higher H_2O:C. However, there was a decrease in CO associated with higher H_2O:C, which contributes significantly to the heating value of the fuel on a molar basis.

6.3.5 Effect on Solar-to-Fuel Efficiency

Solar-to-fuel efficiency measures how effectively solar energy is converted into syngas. It is an important metric in solar thermochemical processes, and is applicable for the data

obtained due to the same level of solar energy being used in all experimental trials. As solar input decreases and approaches zero for fully autothermal operation, $\eta_{\text{solar-to-fuel}}$ increases and approaches *R*. An ANOVA was performed on the data considering the two treatments effects and their interaction on $\overline{\eta}_{\text{solar-to-fuel}}$. Results are shown in Table 6.7. There is strong evidence to suggest that O_2:C had an effect on $\overline{\eta}_{\text{solar-to-fuel}}$ ($P < 0.0001$). There also is evidence to suggest a possible interaction between H_2O:C and O_2:C on $\overline{\eta}_{\text{solar-to-fuel}}$ ($P < 0.05$).

Table 6.7 ANOVA table comparing the effects and interaction of H_2O:C and O_2:C on $\overline{\eta}_{\text{solar-to-fuel}}$.

	df	SS	MS	F	P (>F)
H_2O:C	1	0	0	0	1
O_2:C	1	0.00845	0.00845	338	5.2e-05
H_2O:C×O_2:C	1	0.00045	0.00045	18	0.0132
Error	4	0.0001	0.00003		
Total	7	0.009			

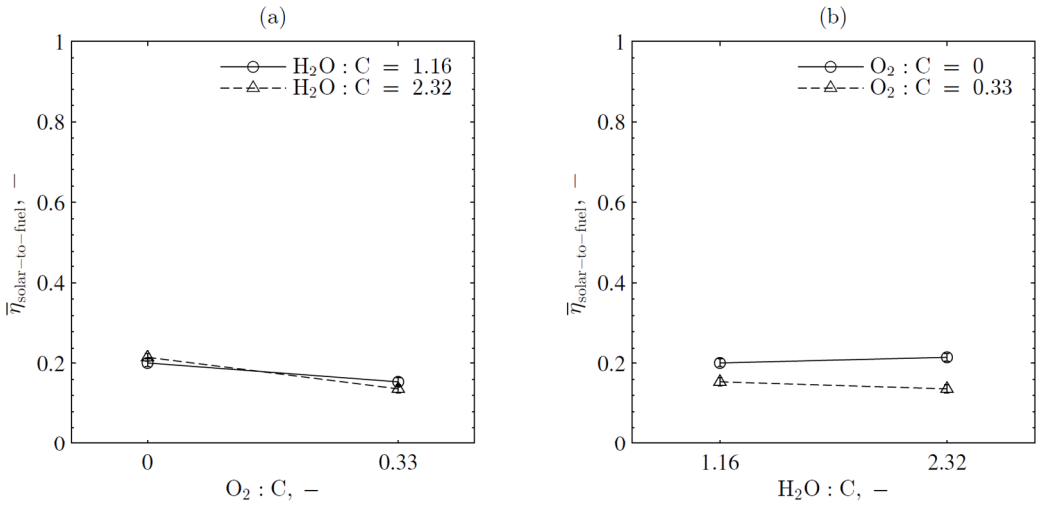

Figure 6.8 (a) H_2O:C-against-O_2:C and (b) O_2:C-against-H_2O:C interaction plots for $\overline{\eta}_{\text{solar-to-fuel}}$ means. Low and high levels are shown using circles and triangles, respectively, with error bars based on 95% confidence limits.

Interaction plots of $\overline{\eta}_{\text{solar-to-fuel}}$ means are shown in Figure 6.8a and Figure 6.8b with error bars based on 95% confidence limits. Figure 6.8a shows the negative effect of increased O_2:C on $\overline{\eta}_{\text{solar-to-fuel}}$. The lines cross, indicative of a possible interaction between H_2O:C and O_2:C. An antagonistic interaction is also shown between H_2O:C and O_2:C in Figure 6.8b. This indicates that while increasing H_2O:C led to increased $\overline{\eta}_{\text{solar-to-fuel}}$ for the low O_2:C condition, it had the opposite effect for the high O_2:C. These changes are slight, but still outside of the error bounds. This effect was expected, as combusting more of the feedstock leads to lower utilization of solar energy. In addition, the higher temperatures for the high O_2:C experiments were coupled with increased reradiative losses. It is not as clear what led to a negative correlation between H_2O:C and $\overline{\eta}_{\text{solar-to-fuel}}$ given the same O_2:C, and this is an area that may require further investigation.

6.3.6 Effect on CO_2 Production

CO_2 is an undesirable product in syngas and must be separated out prior to F-T synthesis. In addition, CO_2 production should be mitigated due to its global warming potential. Water-gas shift and combustion reactions had a clear effect on CO_2 production in the conditions tested. An ANOVA was performed on the data considering the two treatments effects and their interaction on $\bar{\dot{n}}_{CO_2}$. Results are shown in Table 6.8. There is evidence to suggest that both treatment effects and their interaction had an effect on $\bar{\dot{n}}_{CO_2}$ at varying levels of significance. H_2O:C and O_2:C were significant with $P < 0.0001$, and their interaction was less significant with $P < 0.05$.

Table 6.8 ANOVA table comparing the effects and interaction of H_2O:C and O_2:C on $\bar{\dot{n}}_{CO_2}$.

	df	SS	MS	F	P (>F)
H_2O:C	1	62.16	62.16	325.0	5.6e-05
O_2:C	1	181.5	181.5	948.8	6e-06
H_2O:C×O_2:C	1	2.311	2.311	12.09	0.0254
Error	4	0.765	0.191		
Total	7	246.7			

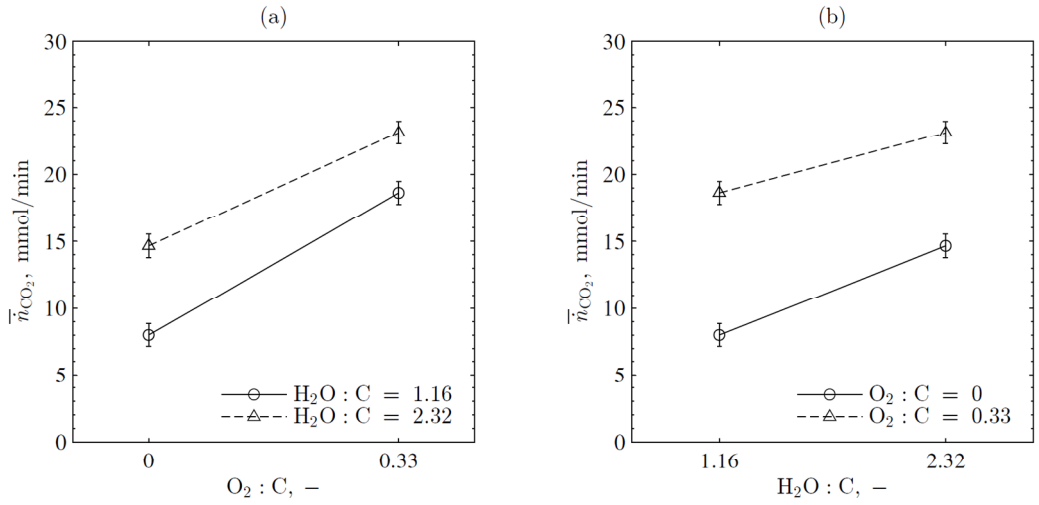

Figure 6.9 (a) H_2O:C-against-O_2:C and (b) O_2:C-against-H_2O:C interaction plots for $\bar{\dot{n}}_{CO_2}$ means. Low and high levels are shown using circles and triangles, respectively, with error bars based on 95% confidence limits.

Interaction plots of $\bar{\dot{n}}_{CO_2}$ means are shown in Figure 6.9a and Figure 6.9b with error bars based on 95% confidence limits. Both plots show a synergistic pattern between treatment effects and the response variable with $\bar{\dot{n}}_{CO_2}$ increasing as both H_2O:C and O_2:C increased. The interaction is evidenced by the observation that slopes differ between treatments. Increasing H_2O:C led to a diminished effect from O_2:C and vice versa. The positive correlation between both treatments and $\bar{\dot{n}}_{CO_2}$ was expected due to the increased prevalence of the water-gas shift reaction and combustion, and was also predicted by chemical equilibrium. In a hybrid solar/autothermal gasification operation, the production of CO_2 would need to be carefully controlled and accounted for to minimize emissions to the atmosphere and the power required to separate gases.

6.4 Discussion

The results point to a number of notable interactions between H_2O:C and O_2:C for a solar-driven gasification system. To the author's knowledge, this is the first "on-sun" demonstration of a hybrid solar/autothermal gasification process, as well as the first indirectly-irradiated fluidized bed constructed out of SiC to be tested "on-sun." The system successfully created syngas and demonstrated temperature effects from the introduction of O_2, but has room for optimization to improve performance. Carbon conversions were slightly higher than those achieved by SiC drop tube experiments described in Section 5.2 [42, 50], higher than those in the entrained flow reactor [34], and slightly lower than those achieved by the drop-tube fixed-bed reactor [53]. However, the temperatures of operation were generally lower in the solar mode than in other studies, and improved kinetics could be expected at higher temperatures. Particle entrainment may have limited carbon conversions, and one immediate solution would be to reduce the total gas flow entering the reactor. However, this would come at the expense of mass transfer and associated heat transfer due to reduced fluidization of larger charcoal particles in the bed. Cold gas (upgrade) ratios and solar-to-fuel efficiencies were very similar to those achieved by the drop-tube fixed-bed reactor. These parameters could be improved by operating at higher temperatures, reducing the formation of CO_2.

The conclusion that bed temperature was significantly affected by O_2:C was expected, but is noteworthy in its implications for a continuous hybrid solar/autothermal gasification process. The impact of O_2:C on carbon conversion was also important, as it may allow for more rapid conversion and tuning of the feedstock amount within the reactor due to fast combustion kinetics. The negative consequences of combustion were

equally significant, with O_2:C negatively impacting H_2:CO ratio, cold gas ratio, solar-to-fuel efficiency, and CO_2 production. Therefore, O_2 use in a hybrid operation should be minimized and used only when required to maintain acceptable performance parameters. The effects of changing H_2O level were less dramatic, but still important in the performance of a hybrid gasification process. The most significant effect is tied to the water-gas shift reaction, affecting both H_2:CO and CO_2 production. These effects are antagonistic; improved H_2:CO ratio for F-T synthesis will come at the expense of increased CO_2 production. A far less notable impact was seen on cold gas ratio, with slight decreases as H_2O:C increased. The significant interactions for carbon conversion, CO_2 production, cold gas ratio, and solar-to-fuel efficiency point to a complex interplay between reacting gases that may require a more in-depth analysis.

6.5 Summary

A first-of-its-kind prototype hybrid solar/autothermal gasification reactor was successfully tested for four different inlet gas conditions, and approximate steady-state results were statistically analyzed using ANOVA. The same lamp powers and feedstock mass flow rates were used for all experiments. Results were repeatable and showed significant differences in temperature, H_2:CO ratio, carbon conversion, cold gas ratio, solar-to-fuel efficiency, and CO_2 production depending on inlet gas flows. Interaction plots were created to examine treatment effects and interactions. Temperature increases were observed from oxy-combustion without runaway reactions or material failure. Use of O_2 was also associated with negative effects on H_2:CO ratio, cold gas ratio, solar-to-fuel efficiency, and CO_2 production. Carbon conversions, cold gas ratios, and solar-to-

fuel efficiencies were comparable with those from previous studies. The proof-of concept demonstrated process feasibility and that such a concept warrants further investigation.

CHAPTER 7. CONCLUSIONS AND FUTURE WORK

This thesis proposed and developed the novel concept of a continuously-operating hybrid solar/autothermal gasification process. Such a process removes one of the key hurdles to greater utilization of concentrated solar energy to drive gasification and store solar energy: intermittency. It also would add a level of controllability that is missing in most current solar gasification experimental campaigns. Conventional autothermal gasification systems are well-developed, but are inherently limited in their efficiencies and long-term sustainability due to the consumption of valuable feedstock in combustion reactions. In addition, the pure O_2 required for oxy-combustion has a high cost associated with it. Solar gasification has been demonstrated in a number of different reactor designs, but still faces challenges due to restrictions on operation time. A downstream F-T or other catalytic process would operate poorly in the face of large syngas fluctuations and long-term storage of syngas remains problematic. These issues could be addressed through hybridization. In order to comprehensively develop the concept, various modeling and experimental tasks were completed, which are highlighted in the following section.

7.1 Research Contributions

The first phase of research involved demonstrating the concept through basic reactor modeling. Chemical equilibrium compositions and their associated reaction enthalpies were calculated using Gibbs free energy minimization for allothermal (solar-driven) and autothermal conditions, and formed the basis for the hybrid concept model. Reactor concept modeling was performed at the 5-MW_{th} scale, and a transient, finite-volume heat

and mass transfer model was built to examine product flows given solar inputs based on hourly direct normal irradiance data. Chemical equilibrium was assumed at the outlet, and the zonal method was used to account for participating media. A feedforward controller was developed to dynamically adjust molar inputs of feedstock and O_2 to control reaction zone temperature. Results for four consecutive days of operation were analyzed in terms of cold gas ratio, syngas output, CO_2 production, and the associated work to separate gases. In addition, the model was run for different periods of the year to evaluate seasonal changes in performance. The model showed good temperature controllability and ability to maintain syngas output regardless of solar resource availability.

A series of kinetic analyses were performed for combustion and gasification reactions for three feedstocks: activated charcoal derived from wood, bituminous coal char, and miscanthus char. This was accomplished by running a series of thermogravimetric experiments to gasify and combust the feedstocks under various reacting gas concentrations. Non-isothermal experiments were conducted over temperature ranges of 550-960 and 1120-1270 K and concentrations of 10–40% O_2–Ar and 20–100% H_2O–CO_2 for combustion and gasification, respectively. Data were fit to Langmuir-Hinshelwood-type reaction mechanisms to obtain Arrhenius parameters, and 95% confidence bounds were found using chi-squared boundaries. A series of additional experiments were run to examine the effects of particle size, heating rate, and total gas flow rate. Scanning electron microscopy and Brunauer–Emmett–Teller analysis were also performed to characterize feedstock particles.

In tandem with the experimental efforts, robust radiation modeling was performed to examine various reactor geometries and lamp configurations. Monte Carlo ray tracing methods were used to estimate the heat fluxes absorbed at various surfaces in the reactor with the goal of maximizing the heat flux absorbed by the tube while trying to avoid extreme gradients in flux. Spectrally-dependent material properties were taken into account. Grid and ray independence studies were performed, followed by parametric studies investigating tube positions with the cavity, aperture shape, number of lamps, and position of lamps. Flux maps were plotted, and peak and average heat fluxes were reported for the focal area. Use of the center and top lamps was beneficial due to the horizontal position of the tube and radiation from the top lamp impinging lower on the tube. In the final configuration, the tube was estimated to absorb 23.3% of the total thermal power emitted by the lamps.

An indirectly-irradiated fluidized-bed reactor was designed and fabricated for use in a high-flux solar simulator. The prototype was designed to use inert, high-temperature-limit materials for solar thermochemical applications in a novel configuration and allow for continuous operation. Granular activated charcoal derived from peat was selected as the feedstock due to its high carbon content and resistance to entrainment based on fluidization calculations. An array of instrumentation was set up to control lamp power, particle feeding, and gas flows, as well as monitor temperatures, pressures, and product gas compositions. Lamp power was calibrated by taking images of a Lambertian target at the focal plane and correlating pixel levels to radiative heat fluxes.

The final stage in the research effort was to perform “on-sun” testing of the hybrid solar/autothermal gasification reactor and analyze the results. An experimental procedure

was developed to allow for repeatable testing and quasi-steady-state operation. Four experimental conditions were tested: low and high levels of H_2O (H_2O:C = 1.16 and 2.32) and O_2 (O_2:C = 0 and 0.33), while lamp power and charcoal feeding rate remained the same across all runs. Two replicates were performed for each experiment. Chemical equilibrium calculations were performed at each condition to give predicted molar compositions. Results were statistically analyzed using analysis of variance, specifically investigating the treatment effects on bed temperature, H_2:CO ratio, carbon conversion, cold gas ratio, solar-to-fuel efficiency, and CO_2 production. Interaction plots were used to illustrate the treatment effects and their interactions. O_2:C was found to have a significant effect on all of the metrics examined, while H_2O was found to have significant effects on H_2:CO ratio, CO_2 production, and cold gas ratio. There were also notable interactions between treatments for carbon conversion, CO_2 production, cold gas ratio, and solar-to-fuel efficiency.

First and foremost, the experimental campaign proved that O_2 could be fed into a solar gasification reactor reliably to increase temperatures at the kW-scale. In addition, the time response on temperature from initiation of O_2 flow was on the order of seconds – a timescale that could readily match the frequency of solar transients. Ability to vary H_2O could allow for a supplemental degree of controllability, particularly with respect to metrics like H_2:CO ratio. Besides the obvious benefit of continuous operation, hybridization of a solar gasification process could also mitigate thermal shocks that would result from intermittent cloud cover. This is a critical issue for solar gasification, particularly for opaque absorbers made out of ceramic materials. In locations were solar resources are not as abundant, a hybrid process would allow for a more viable method of

thermochemical conversion while still utilizing a renewable resource when it is available. There is significant room for improvement of the processes and further exploratory studies.

7.2 Future Work

The work described in this thesis represents a first experimental investigation of a hybrid solar/autothermal gasification process, and there are a number of possible avenues to further the research. In the near-term, several adjustments could be made to the reactor to attempt to improve its performance and gather new information:

- Lower gas flow rates could be used to avoid entrainment of smaller feedstock particles and improve conversion
- Lower lamp powers could prevent ash melting during autothermal operation, and ash removal methods could be developed for long-term operation
- The reactor could be tested with different feedstocks, such as biomass
- An ash analysis could be used to reveal potential catalytic effects in the bed

If feedstock particles are being entrained before reacting, they are absorbing sensible heat and carrying it out of the reaction zone without undergoing conversion into useful products. It is clear from the results that the increases in temperature due to combustion do not improve carbon conversion for the high H_2O:C condition, which does not indicate a kinetic limitation. Therefore, it may be possible to lower lamp power and improve efficiencies while avoiding ash melting without negatively impacting other performance metrics. For tests lasting longer than one hour, ash buildup in the bed would need to be addressed. In order to reduce carbon intensities and improve sustainability, biomass

feedstocks would need to be used. Biomass feedstocks inherently have lower fixed-carbon content, so a reduction in performance would be expected. Energy-dispersive X-ray spectroscopy could be used to determine the presence of Ca or K in the granular activated charcoal ash, which could indicate potential catalytic effects in the fluidized bed.

In the long-term:

- More detailed kinetic models could be used to more accurately capture kinetic rates
- A reactor could be developed to operate allothermally using combustion as well as solar irradiation
- Control strategies could be investigated and developed in more detail

As described in Section 3.2, more detailed mechanisms for gasification exist in literature that may be able to more accurately describe reaction rates based on more fundamental phenomena occurring at the C surface. Back reactions for gasification could be analyzed using thermogravimetry by introducing small concentrations of H_2 as a reacting gas. This could potentially help model reaction rates inside of a fluidized bed where solid particles are contacting gaseous products. Results could also be applied to a computational fluid dynamics code that tracks particles in the bed and sets reactions rates based on temperatures and gas concentrations.

There are clear trade-offs between autothermal and combustion-driven allothermal gasification. Autothermal gasification generates heat in the same location where gasification takes place, leading to efficient heat transfer and rapid temperature

response. However, the combustion products must be dealt with in the product stream. Allothermal gasification does not dilute the product stream, but does not efficiently provide heat to the gasification reactions due to conduction losses. In addition, the transport of heat to the reactants occurs on longer timescales. It would be worth investigating a continuous hybrid allothermal gasification process driven by both solar energy and combustion. Reactor design would be more challenging, as heat from concentrated solar energy and heat from combustion would likely need to be provided from two different locations in the reactor.

There is significant work to be done in the control of a hybrid solar/autothermal gasification process and control of solar gasification processes in general. The system needs to be able to respond to high-frequency solar transients, and introducing combustion reactions would add an additional level of complexity. However, the results from this thesis bode well for process repeatability, even when O_2 is present. If the responses to O_2 and H_2O could be characterized in more detail, as well as the response to varying feedstock mass flow rate, a more sophisticated control system could be developed than what is presented in this work. Ideally, a system could be developed to dynamically adjust O_2 and/or feedstock in response to adjustments of lamp power in the solar simulator, demonstrating practical operation of such a process.

APPENDIX A. SOLIDWORKS REACTOR DRAWINGS

SolidWorks render of full reactor setup. Does not include wires, ¼" tubing, or dry ice container.

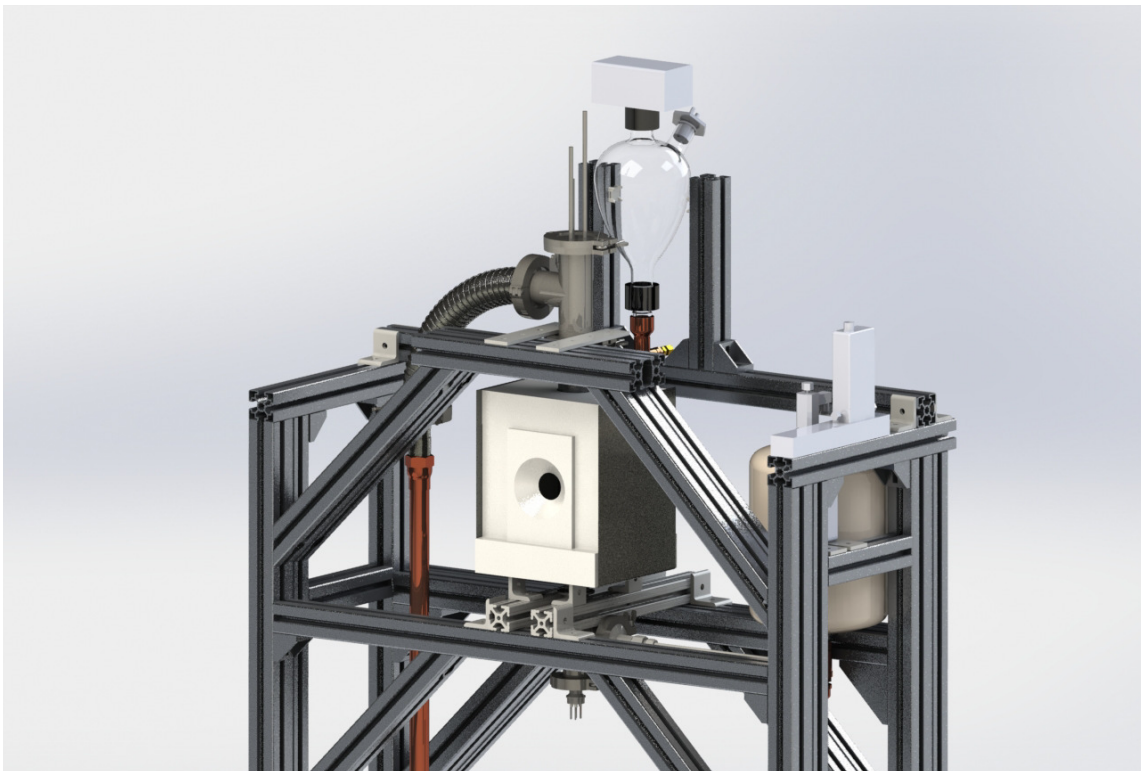

SolidWorks render of reactor setup viewed from the front

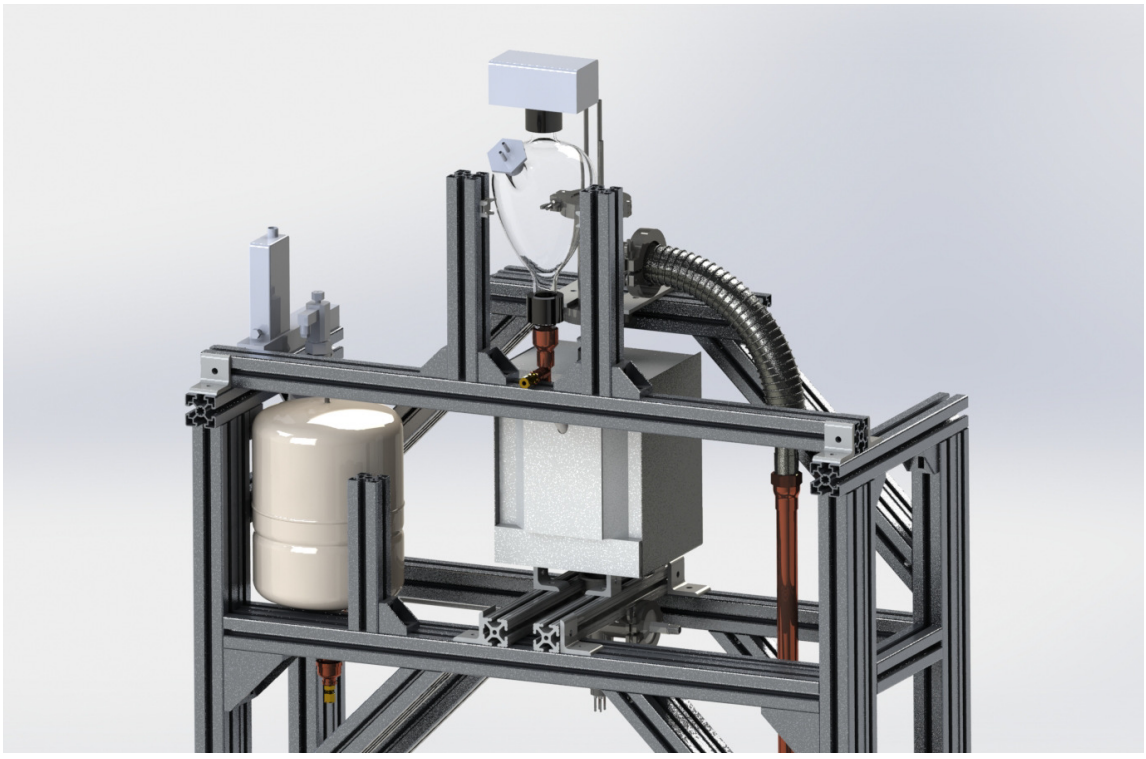

SolidWorks render of reactor setup viewed from the back

APPENDIX B. LABVIEW VI

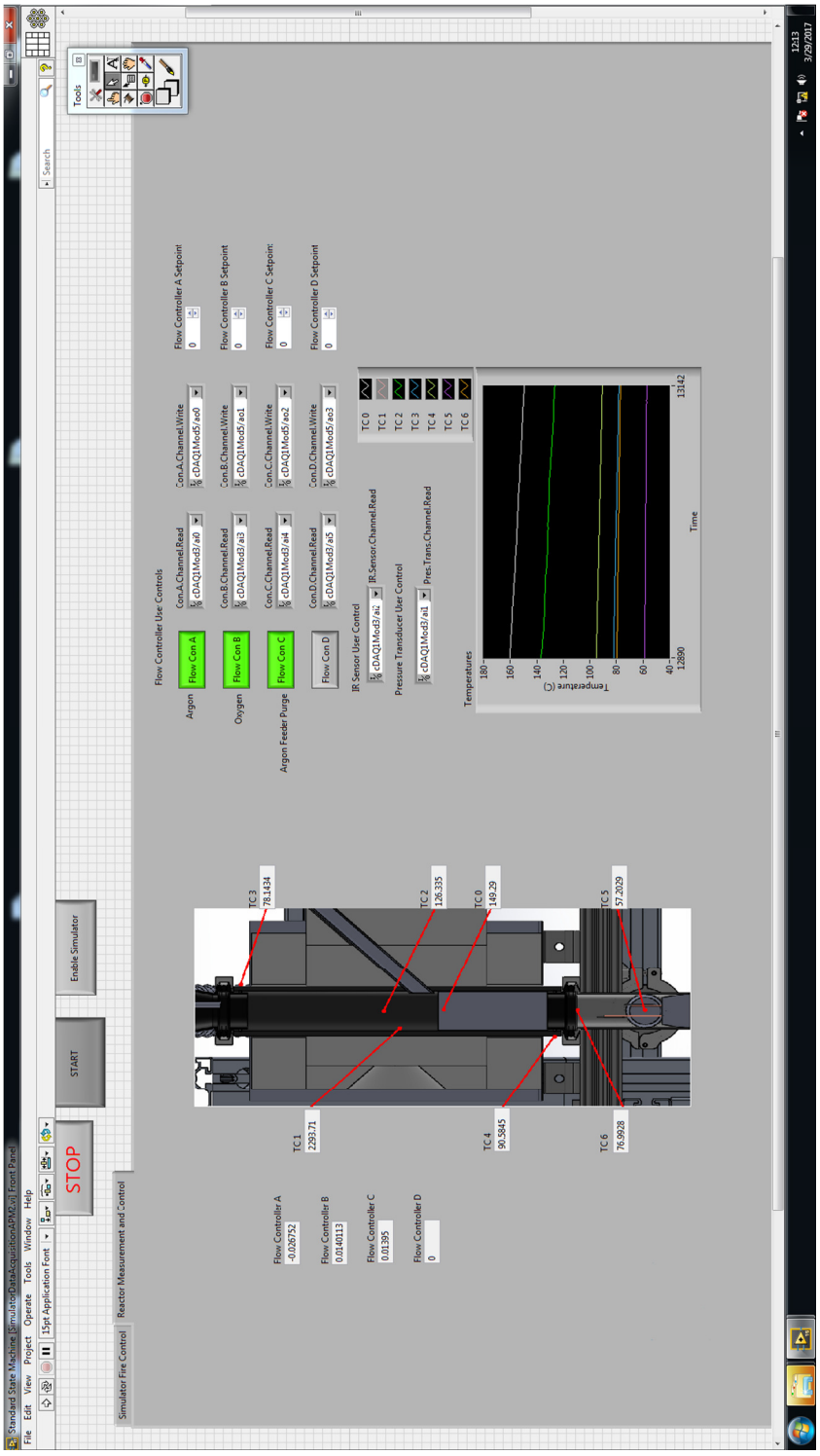

Screenshot of the LabVIEW VI: Reactor measurement and control

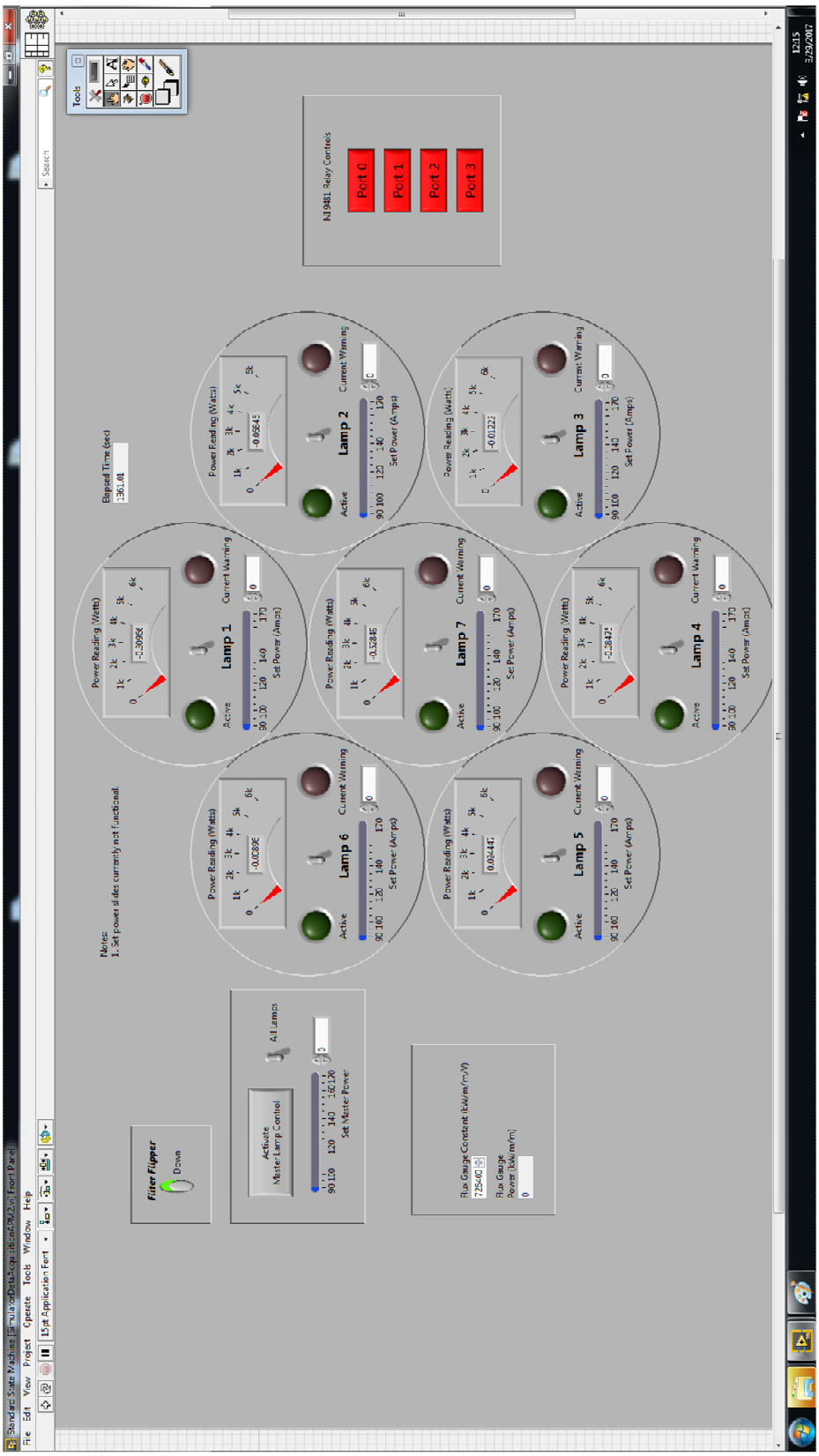

Screenshot of LabVIEW VI: Simulator fire control

APPENDIX C. EXAMPLE MS PLOTS FOR "ON-SUN" TESTING

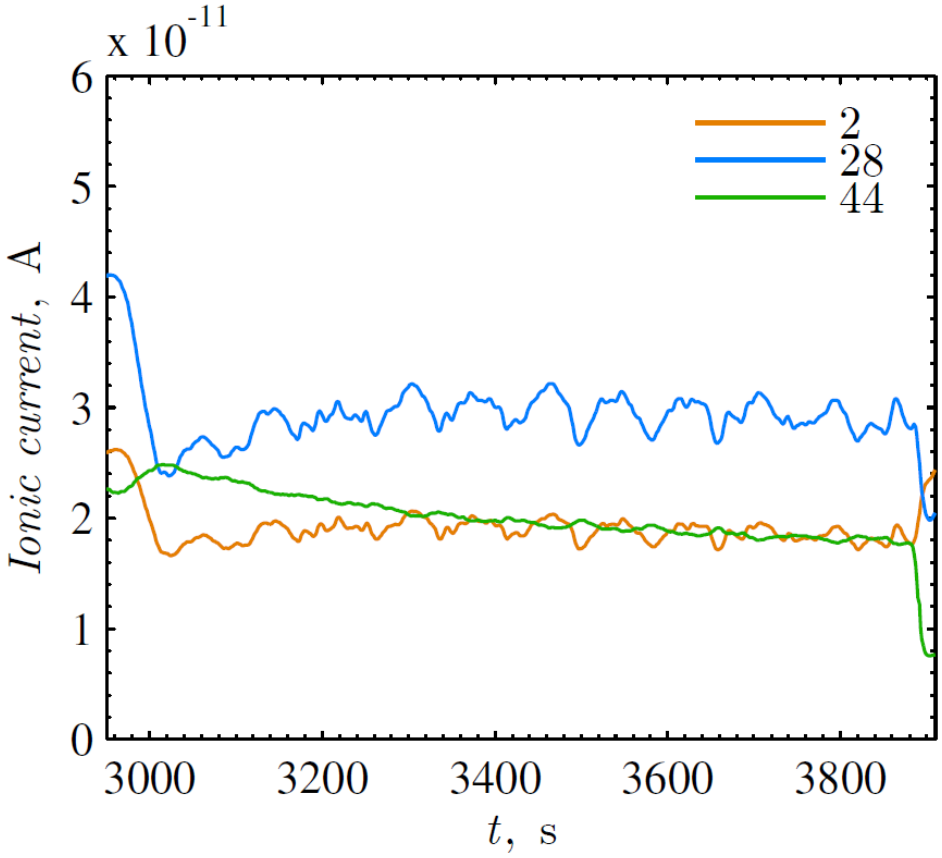

Plot of ionic current versus time for representative low H_2O, high O_2 run from MS. Times shown are for ~15 min of feedstock and O_2 feeding. Legend gives molecular weights in g/mol, corresponding to H_2, CO, and CO_2.

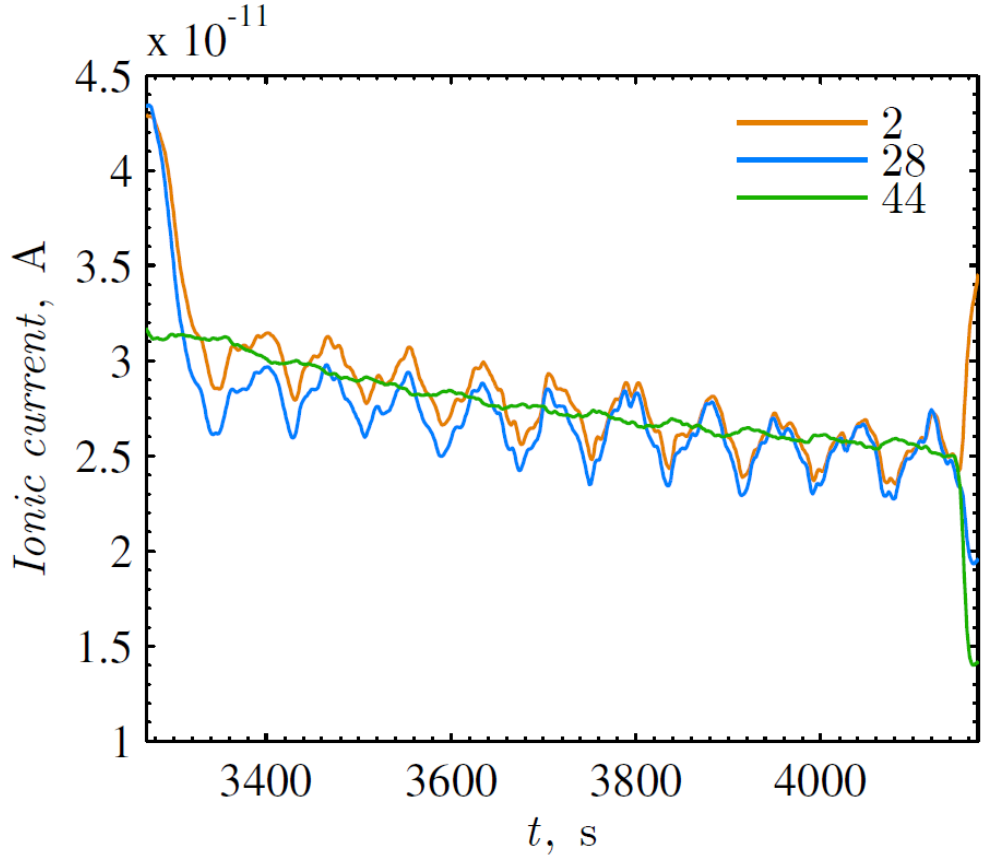

Plot of ionic current versus time for representative high H_2O, high O_2 run from MS. Times shown are for ~15 min of feedstock and O_2 feeding. Legend gives molecular weights in g/mol, corresponding to H_2, CO, and CO_2.

APPENDIX D. REACTOR PHOTOS

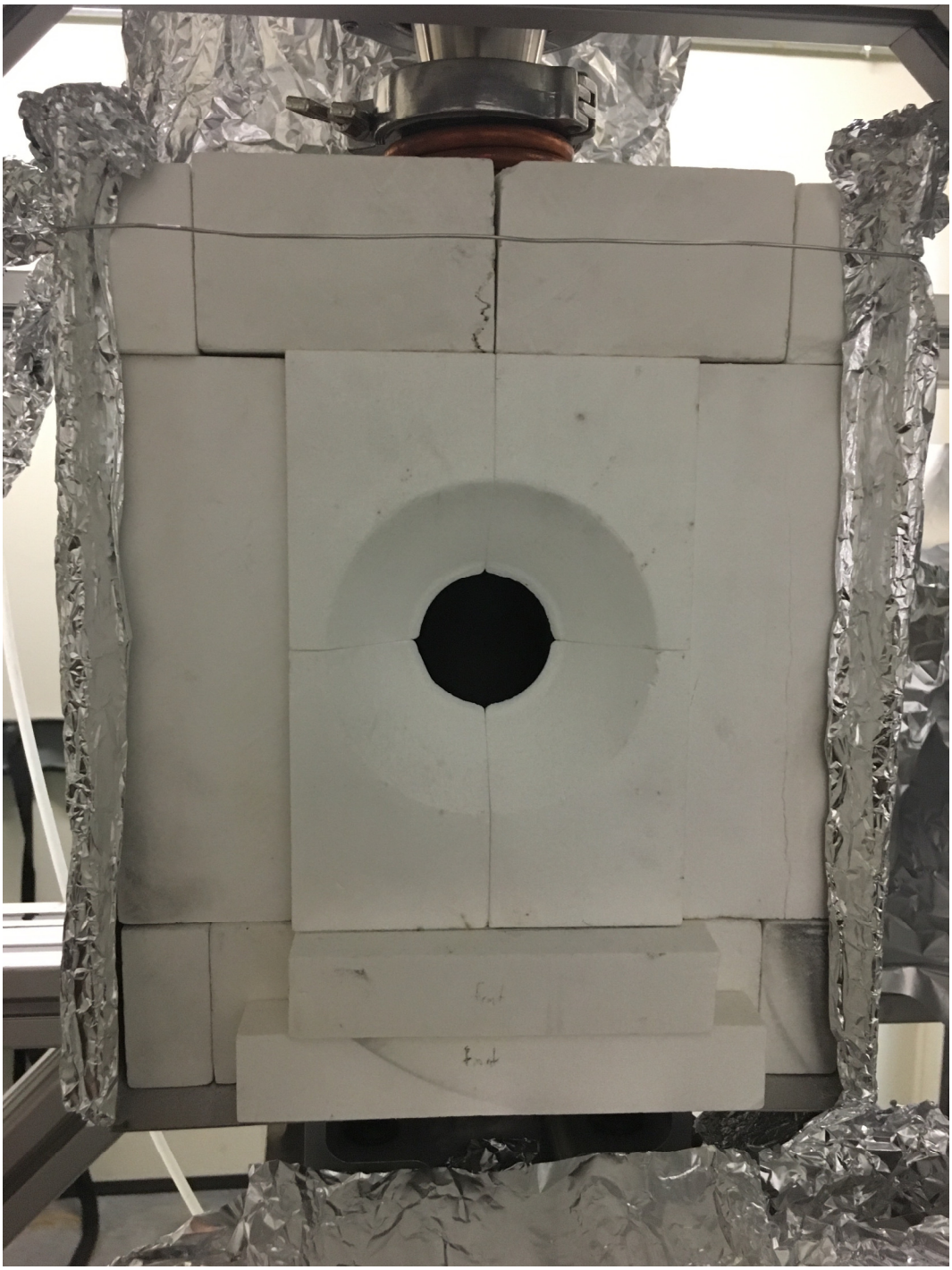

Reactor front prior to an experiment

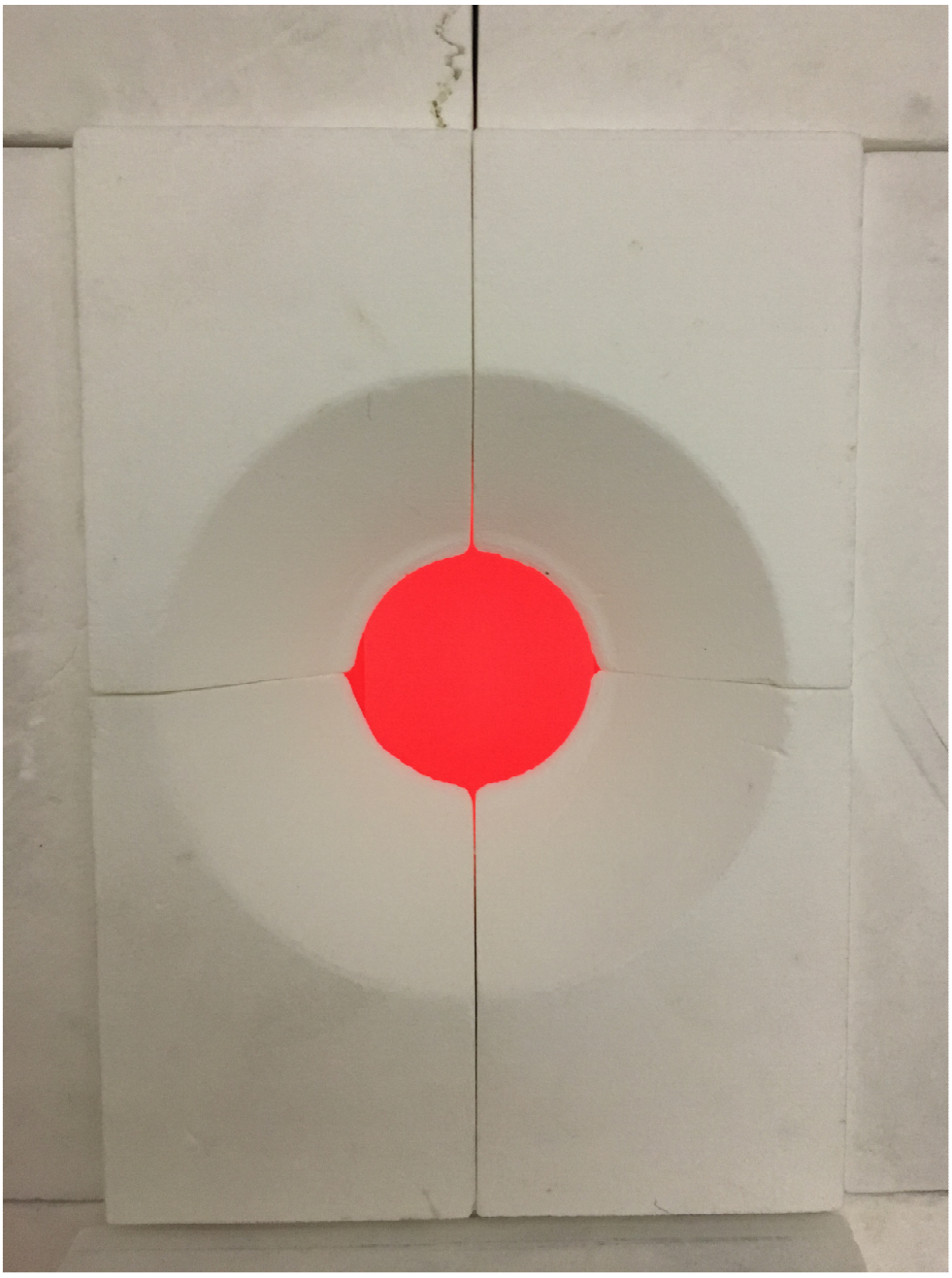

Reactor aperture after an experiment, with the hot emitter tube emitting in the visible spectrum

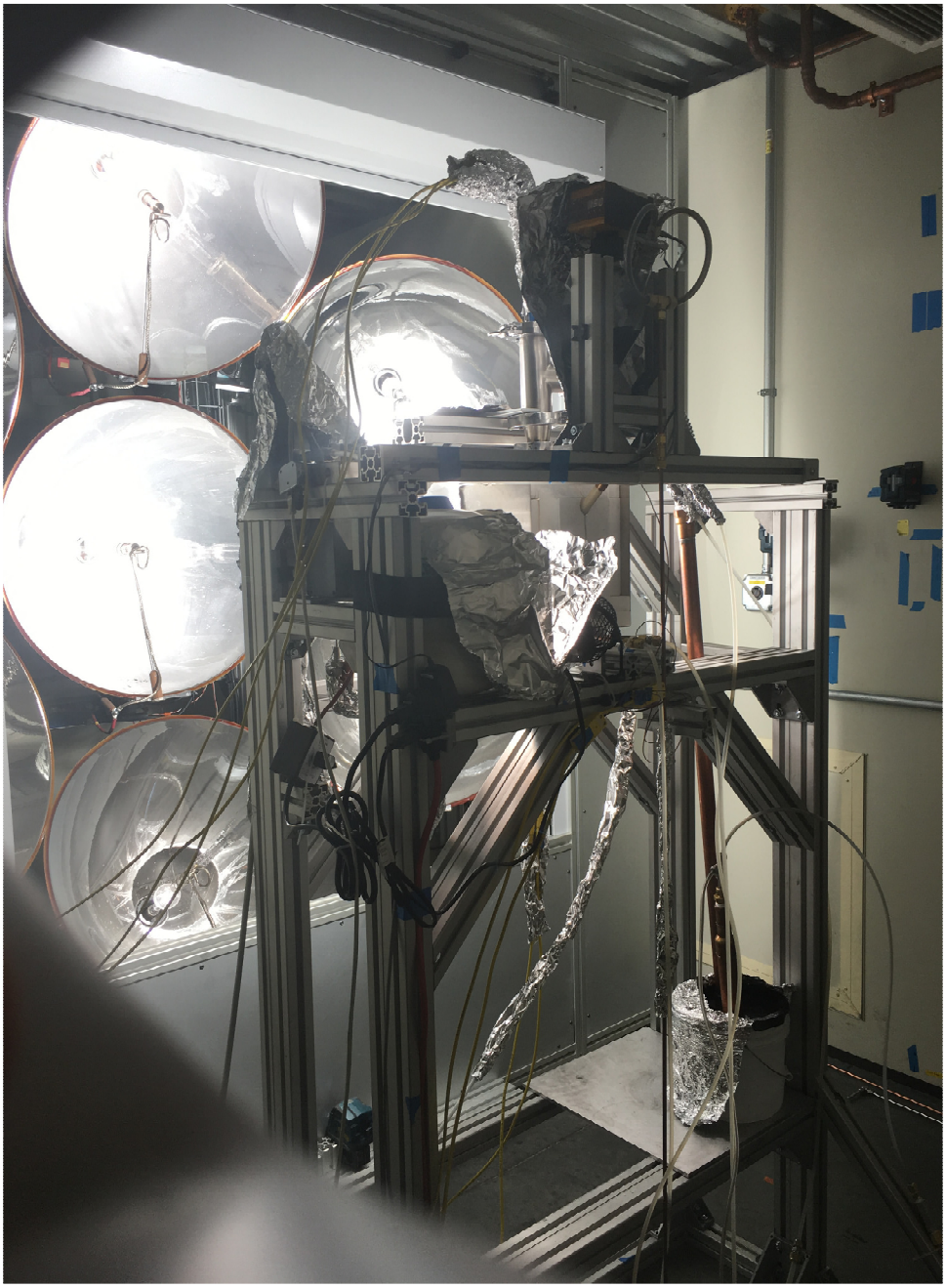

Reactor setup during an “on-sun” test

REFERENCES

[1] (EIA), U. S. E. I. A., 2016, "International Energy Outlook 2016," No. DOE/EIA-0484(2016), U.S. Department of Energy, Washington, DC.

[2] Cormos, C.-C., 2012, "Hydrogen and Power Co-Generation Based on Coal and Biomass/Solid Wastes Co-Gasification with Carbon Capture and Storage," Int. J. Hydrogen Energy, 37(7), pp. 5637-5648.

[3] Frey, H. C., and Zhu, Y., 2006, "Improved System Integration for Integrated Gasification Combined Cycle (IGCC) Systems," Environ. Sci. Technol., 40(5), pp. 1693-1699.

[4] Dry, M. E., 2002, "The Fischer–Tropsch Process: 1950–2000," Catal. Today, 71(3–4), pp. 227-241.

[5] James, O. O., Mesubi, A. M., Ako, T. C., and Maity, S., 2010, "Increasing Carbon Utilization in Fischer–Tropsch Synthesis Using H2-Deficient or CO2-Rich Syngas Feeds," Fuel Processing Technology, 91(2), pp. 136-144.

[6] Ail, S. S., and Dasappa, S., 2016, "Biomass to liquid transportation fuel via Fischer Tropsch synthesis – Technology review and current scenario," Renewable and Sustainable Energy Reviews, 58, pp. 267-286.

[7] Semelsberger, T. A., Brown, L. F., Borup, R. L., and Inbody, M. A., 2004, "Equilibrium Products from Autothermal Processes for Generating Hydrogen-Rich Fuel-Cell Feeds," Int. J. Hydrogen Energy, 29(10), pp. 1047-1064.

[8] Yoon, H. C., Cooper, T., and Steinfeld, A., 2011, "Non-Catalytic Autothermal Gasification of Woody Biomass," Int. J. Hydrogen Energy, 36, pp. 7852-7860.

[9] Dufour, J., Serrano, D. P., Gálvez, J. L., Moreno, J., and González, A., 2011, "Hydrogen Production from Fossil Fuels: Life Cycle Assessment of Technologies with Low Greenhouse Gas Emissions," Energy Fuels, 25(5), pp. 2194-2202.

[10] Iliuta, I., Leclerc, A., and Larachi, F., 2010, "Allothermal Steam Gasification of Biomass in Cyclic Multi-Compartment Bubbling Fluidized-Bed Gasifier/Combustor – New Reactor Concept," Bioresour. Technol., 101(9), pp. 3194-3208.

[11] Mayerhofer, M., Mitsakis, P., Meng, X., de Jong, W., Spliethoff, H., and Gaderer, M., 2012, "Influence of Pressure, Temperature and Steam on Tar and Gas in Allothermal Fluidized Bed Gasification," Fuel, 99(0), pp. 204-209.

[12] Maag, G., and Steinfeld, A., 2010, "Design of a 10 MW Particle-Flow Reactor for Syngas Production by Steam-Gasification of Carbonaceous Feedstock Using Concentrated Solar Energy," Energy Fuels, 24(12), pp. 6540-6547.

[13] Piatkowski, N., Weickert, C., Weimer, A. W., and Steinfeld, A., 2011, "Solar driven gasification of carbonaceous feedstock - a review," Energy Environ. Sci., 4, pp. 73-82.

[14] Taylor, R. W., Berjoan, R., and Coutures, J. P., 1983, "Solar Gasification of Carbonaceous Materials," Sol. Energy, 30(6), pp. 513-525.

[15] Lédé, J., 1999, "Solar Thermochemical Conversion of Biomass," Sol. Energy, 65(1), pp. 3-13.

[16] Apt, J., Newcomer, A., Lave, L. B., Douglas, S., and Dunn, L. M., 2008, "An Engineering-Economic Analysis of Syngas Storage," National Energy Technology Laboratory.

[17] Lu, X., Hildebrandt, D., Liu, X., and Glasser, D., 2010, "Making Sense of the Fischer–Tropsch Synthesis Reaction: Start-Up," Ind. Eng. Chem. Res., 49(20), pp. 9753-9758.

[18] Botero, C., Field, R. P., Herzog, H. J., and Ghoniem, A. F., 2013, "Impact of Finite-Rate Kinetics on Carbon Conversion in a High-Pressure, Single-Stage Entrained Flow Gasifier with Coal–CO2 Slurry Feed," Applied Energy, 104(0), pp. 408-417.

[19] Cummer, K. R., and Brown, R. C., 2002, "Ancillary Equipment for Biomass Gasification," Biomass and Bioenergy, 23(2), pp. 113-128.

[20] Kihedu, J. H., Yoshiie, R., and Naruse, I., 2016, "Performance indicators for air and air–steam auto-thermal updraft gasification of biomass in packed bed reactor," Fuel Processing Technology, 141, Part 1, pp. 93-98.

[21] Wang, L.-Q., and Chen, Z.-S., 2013, "Gas generation by co-gasification of biomass and coal in an autothermal fluidized bed gasifier," Applied Thermal Engineering, 59(1–2), pp. 278-282.

[22] Sandeep, K., and Dasappa, S., 2014, "First and second law thermodynamic analysis of air and oxy-steam biomass gasification," International Journal of Hydrogen Energy, 39(34), pp. 19474-19484.

[23] Kruesi, M., Jovanovic, Z. R., dos Santos, E. C., Yoon, H. C., and Steinfeld, A., 2013, "Solar-Driven Steam-Based Gasification of Sugarcane Bagasse in a Combined Drop-Tube and Fixed-Bed Reactor – Thermodynamic, Kinetic, and Experimental Analyses," Biomass Bioenergy, 52(0), pp. 173-183.

[24] Gregg, D. W., Aiman, W. R., Otsuki, H. H., and Thorsness, C. B., 1980, "Solar Coal Gasification," Sol. Energy, 24(3), pp. 313-321.

[25] Mathur, V. K., Breault, R. W., and Lakshmanan, S., 1983, "Coal gasification using solar energy," Solar Energy, 30(5), pp. 433-440.

[26] Ng, Y. C., and Lipiński, W., 2012, "Thermodynamic Analyses of Solar Thermal Gasification of Coal for Hybrid Solar-Fossil Power and Fuel Production," Energy, 44(1), pp. 720-731.

[27] Trommer, D., and Steinfeld, A., 2006, "Kinetic Modeling for the Combined Pyrolysis and Steam Gasification of Petroleum Coke and Experimental Determination of the Rate Constants by Dynamic Thermogravimetry in the 500-1520 K Range," Energy Fuels, 20, pp. 1250-1258.

[28] Trommer, D., Noembrini, F., Fasciana, M., Rodriguez, D., Morales, A., Romero, M., and Steinfeld, A., 2005, "Hydrogen Production by Steam-Gasification of Petroleum Coke Using Concentrated Solar Power—I. Thermodynamic and Kinetic Analyses," Int. J. Hydrogen Energy, 30(6), pp. 605-618.

[29] Z'Graggen, A., Haueter, P., Trommer, D., Romero, M., de Jesus, J. C., and Steinfeld, A., 2006, "Hydrogen Production by Steam-Gasification of Petroleum Coke Using Concentrated Solar Power—II Reactor Design, Testing, and Modeling," Int. J. Hydrogen Energy, 31(6), pp. 797-811.

[30] Z'Graggen, A., Haueter, P., Maag, G., Vidal, A., Romero, M., and Steinfeld, A., 2006, "Hydrogen Production by Steam-Gasification of Petroleum Coke Using Concentrated Solar Power—III. Reactor Experimentation with Slurry Feeding," Int. J. Hydrogen Energy, 32, pp. 992-996.

[31] von Zedtwitz, P., Lipinski, W., and Steinfeld, A., 2007, "Numerical and Experimental Study of Gas–Particle Radiative Heat Exchange in a Fluidized-Bed Reactor for Steam-Gasification of Coal," Chem. Eng. Sci., 62, pp. 599-607.

[32] Z'Graggen, A., and Steinfeld, A., 2009, "Heat and Mass Transfer Analysis of a Suspension of Reacting Particles Subjected to Concentrated Solar Radiation – Application to the Steam-Gasification of Carbonaceous Materials," Int. J. Heat Mass Transfer, 52(1–2), pp. 385-395.

[33] Maag, G., Lipiński, W., and Steinfeld, A., 2009, "Particle–Gas Reacting Flow Under Concentrated Solar Irradiation," Int. J. Heat Mass Transfer, 52(21–22), pp. 4997-5004.

[34] Melchior, T., Perkins, C., Lichty, P., Weimer, A. W., and Steinfeld, A., 2009, "Solar-Driven Biochar Gasification in a Particle-Flow Reactor," Chem. Eng. Process., 48(8), pp. 1279-1287.

[35] Piatkowski, N., Weickert, C., and Steinfeld, A., 2009, "Experimental investigation of a packed-bed solar reactor for the steam-gasification of carbonaceous feedstocks," Fuel Process. Technol., 90, pp. 360-366.

[36] Piatkowski, N., and Steinfeld, A., 2008, "Solar-driven coal gasification in a thermally irradiated packed-bed reactor," Energy Fuels, 22, pp. 2043-2052.

[37] Piatkowski, N., and Steinfeld, A., 2010, "Reaction kinetics of the combined pyrolysis and steam-gasification of carbonaceous waste materials," Fuel, 89, pp. 1133-1140.

[38] Piatkowski, N., and Steinfeld, A., 2011, "Solar gasification of carbonaceous waste feedstocks in a packed-bed reactor—dynamic modeling and experimental validation," Aiche J., 57(12), pp. 3522-3533.

[39] Gokon, N., Ono, R., Hatamachi, T., Liuyun, L., Kim, H.-J., and Kodama, T., 2012, "CO2 Gasification of Coal Cokes Using Internally Circulating Fluidized Bed Reactor by Concentrated Xe-Light Irradiation for Solar Gasification," Int. J. Hydrogen Energy, 37(17), pp. 12128-12137.

[40] Gokon, N., Izawa, T., Abe, T., and Kodama, T., 2014, "Steam gasification of coal cokes in an internally circulating fluidized bed of thermal storage material for solar thermochemical processes," International Journal of Hydrogen Energy, 39(21), pp. 11082-11093.

[41] Gokon, N., Izawa, T., and Kodama, T., 2015, "Steam gasification of coal cokes by internally circulating fluidized-bed reactor by concentrated Xe-light radiation for solar syngas production," Energy, 79, pp. 264-272.

[42] Martinek, J., Bingham, C., and Weimer, A. W., 2012, "Computational modeling of a multiple tube solar reactor with specularly reflective cavity walls. Part 2: Steam gasification of carbon," Chem. Eng. Sci., 81(0), pp. 285-297.

[43] Martinek, J., Bingham, C., and Weimer, A. W., 2012, "Computational modeling and on-sun model validation for a multiple tube solar reactor with specularly reflective cavity walls. Part 1: Heat transfer model," Chemical Engineering Science, 81(0), pp. 298-310.

[44] Martinek, J., and Weimer, A. W., 2013, "Design Considerations for a Multiple Tube Solar Reactor," Sol. Energy, 90(0), pp. 68-83.

[45] Pereira, E. G., da Silva, J. N., de Oliveira, J. L., and Machado, C. S., 2012, "Sustainable Energy: A Review of Gasification Technologies," Renewable and Sustainable Energy Reviews, 16(7), pp. 4753-4762.

[46] Stevens, D. J., 2001, "Hot Gas Conditioning: Recent Progress With Larger-Scale Biomass Gasification Systems," Subcontract Report No. NREL/SR-510-29952, National Renewable Energy Laboratory, Golden, Colorado.

[47] Bronson, B., Preto, F., and Mehrani, P., 2012, "Effect of Pretreatment on the Physical Properties of Biomass and its Relation to Fluidized Bed Gasification," Environ. Prog. Sustain. Energy, 31(3), pp. 335-339.

[48] Murray, J. P., and Fletcher, E. A., 1994, "Reaction of steam with cellulose in a fluidized bed using concentrated sunlight," Energy, 19(10), pp. 1083-1098.

[49] Perkins, C. M., Woodruff, B., Andrews, L., Lichty, P., Lancaster, B., Bingham, C., and Weimer, A. W., 2008, "Synthesis Gas Production by Rapid Solar Thermal Gasification of Corn Stover," Biennial CSP SolarPACES (Solar Power and Chemical Energy Systems) SymposiumLas Vegas, Nevada.

[50] Lichty, P., Perkins, C., Woodruff, B., Bingham, C., and Weimer, A., 2010, "Rapid High Temperature Solar Thermal Biomass Gasification in a Prototype Cavity Reactor," J. Sol. Energy Eng. Trans.-ASME, 132(1).

[51] Hertwich, E. G., and Zhang, X., 2009, "Concentrating-Solar Biomass Gasfication Process for a 3rd Generation Biofuel," Environmental Science and Technology, 43, pp. 4207-4212.

[52] Hathaway, B. J., Honda, M., Kittelson, D. B., and Davidson, J. H., 2013, "Steam gasification of plant biomass using molten carbonate salts," Energy, 49, pp. 211-217.

[53] Kruesi, M., Jovanovic, Z. R., and Steinfeld, A., 2014, "A two-zone solar-driven gasifier concept: Reactor design and experimental evaluation with bagasse particles," Fuel, 117, Part A(0), pp. 680-687.

[54] Kaniyal, A. A., van Eyk, P. J., and Nathan, G. J., 2013, "Dynamic Modeling of the Coproduction of Liquid Fuels and Electricity from a Hybrid Solar Gasifier with Various Fuel Blends," Energy Fuels, 27(6), pp. 3556-3569.

[55] Kaniyal, A. A., van Eyk, P. J., Nathan, G. J., Ashman, P. J., and Pincus, J. J., 2013, "Polygeneration of Liquid Fuels and Electricity by the Atmospheric Pressure Hybrid Solar Gasification of Coal," Energy Fuels, 27(6), pp. 3538-3555.

[56] Saw, W., Kaniyal, A., van Eyk, P., Nathan, G., and Ashman, P., 2015, "Solar Hybridized Coal-to-liquids via Gasification in Australia: Techno-economic Assessment," Energy Procedia, 69, pp. 1819-1827.

[57] Sudiro, M., and Bertucco, A., 2007, "Synthetic Fuels by a Limited CO2 Emission Process Which Uses Both Fossil and Solar Energy," Energy Fuels, 21(6), pp. 3668-3675.

[58] Petrasch, J., Osch, P., and Steinfeld, A., 2009, "Dynamics and control of solar thermochemical reactors," Chemical Engineering Journal, 145(3), pp. 362-370.

[59] Saade, E., Clough, D. E., and Weimer, A. W., 2014, "Model predictive control of a solar-thermal reactor," Solar Energy, 102(0), pp. 31-44.

[60] Roine, A., 2011, "HSC Chemistry," Outokumpu Res Oy, Finland.

[61] 2014, "MATLAB," MathWorks.

[62] Hippo, E. J., Jenkins, R. G., and Walker Jr, P. L., 1979, "Enhancement of lignite char reactivity to steam by cation addition," Fuel, 58(5), pp. 338-344.

[63] Crelling, J. C., Hagemann, H. W., Sauter, D. H., Ramani, R. V., Vogt, W., Leininger, D., Krzack, S., Meyer, B., Orywal, F., Reimert, R., Bonn, B., Bertmann, U., Klose, W., and Dach, G., 2000, "Coal," Ullmann's Encyclopedia of Industrial Chemistry, Wiley-VCH Verlag GmbH & Co. KGaA.

[64] Bell, D. A., Towler, B. F., and Fan, M., 2011, Coal Gasification and its Applications, Elsevier, Inc., Oxford, UK.

[65] Z'Graggen, A., and Steinfeld, A., 2004, "Radiative Exchange Within a Two-Cavity Configuration With a Spectrally Selective Window," J. Sol. Energy Eng. Trans.-ASME, 126, pp. 819-822.

[66] Wieckert, C., Obrist, A., Zedtwitz, P. v., Maag, G., and Steinfeld, A., 2013, "Syngas Production by Thermochemical Gasification of Carbonaceous Waste Materials in a 150 kWth Packed-Bed Solar Reactor," Energy Fuels, 27(8), pp. 4770-4776.

[67] Maag, G., Falter, C., and Steinfeld, A., 2011, "Temperature of a Quartz/Sapphire Window in a Solar Cavity-Receiver," J. Sol. Energy Eng. Trans.-ASME, 133, pp. 1-4.

[68] Buttsworth, D. R., 1997, "A Finite Difference Routine for the Solution of Transient One Dimensional Heat Conduction Problems with Curvature and Temperature-Dependent Thermal Properties," University of Oxford.

[69] Munro, R. G., 1997, "Material Properties of a Sintered α-SiC," J. Phys. Chem. Ref. Data, 26, pp. 1195-1203.

[70] Auerkari, P., 1996, "Mechanical and Physical Properties of Engineering Alumina Ceramics," Technical Research Center of Finland.

[71] Edwards, D. K., Mills, A. F., and Denny, V. E., 1979, Transfer Processes, Hemisphere/McGraw-Hill, New York.

[72] Wilcox, S., and Marion, W., 2008, "Users Manual for TMY3 Data Sets," No. TP-581-43156, National Renewable Energy Laboratory, Golden, CO.

[73] Pitz Paal, R., Botero, N., and Steinfeld, A., 2011, "Heliostat Field Layout Optimization for High-Temperature Solar Thermochemical Processing," Sol. Energy, 85, pp. 334-343.

[74] Incropera, F. P., Dewitt, D. P., Bergman, T. L., and Lavine, A. S., 2007, Fundamentals of Heat and Mass Transfer, John Wiley & Sons, Inc., New Jersey.

[75] Howell, J. R., 1982, A Catalog of Radiation Configuration Factors, McGraw-Hill, New York.

[76] Modest, M. F., 2003, Radiative Heat Transfer, Academic Press, California.

[77] Muroyama, A., Shinn, T., Fales, R., and Loutzenhiser, P. G., 2014, "Modeling of a Dynamically-Controlled Hybrid Solar/Autothermal Steam Gasification Reactor," Energy Fuels, 28(10), pp. 6520-6530.

[78] Skogestad, S., Postlethwaite, I, 2005, "Multivariable Feedback Control," John Wiley and Sons Ltd., West Sussex, England.

[79] McFarlane, D., and Glover, K., 1992, "A loop-shaping design procedure using H_infinity synthesis," IEEE Transactions on Automatic Control, 37(6), pp. 759-769.

[80] Gibson, T. L., and Kelly, N. A., 2010, "Predicting efficiency of solar powered hydrogen generation using photovoltaic-electrolysis devices," Int. J. Hydrogen Energy, 35(3), pp. 900-911.

[81] Muroyama, A. P., and Loutzenhiser, P. G., 2016, "Kinetic Analyses of Gasification and Combustion Reactions of Carbonaceous Feedstocks for a Hybrid Solar/Autothermal Gasification Process To Continuously Produce Synthesis Gas," Energy & Fuels, 30(5), pp. 4292-4299.

[82] Bryan Woodruff, R., and Weimer, A. W., 2013, "A Novel Technique for Measuring the Kinetics of High-Temperature Gasification of Biomass Char with Steam," Fuel, 103(0), pp. 749-757.

[83] Williams, A., 2011, "An Investigation of the Kinetics for the Fast Pyrolysis of Loblolly Pine Woody Biomass," PhD, Georgia Institute of Technology, Atlanta, GA.

[84] Gadsby, J., Hinshelwood, C. N., and Sykes, K. W., 1946, "The Kinetics of the Reactions of the Steam-Carbon System," Proc. Roy. Soc. A, 187(1009), pp. 129-151.

[85] Gadsby, J., Long, F. J., Sleightholm, P., and Sykes, K. W., 1948, "The Mechanism of the Carbon Dioxide-Carbon Reaction," Proc. Roy. Soc. A, 193(1034), pp. 357-376.

[86] Walker, J., Philip L. , Rusinko, J., Frank , and Austin, L. G., 1959, "Gas Reactions of Carbon," Adv. Catal., 11, pp. 133-221.

[87] Ergun, S., 1962, "Kinetics of the reactions of carbon dioxide and steam with coke," US Government Printing Office.

[88] Laurendeau, N. M., 1978, "Heterogeneous kinetics of coal char gasification and combustion," Prog. Energy Combust. Sci., 4(4), pp. 221-270.

[89] Di Blasi, C., 2009, "Combustion and gasification rates of lignocellulosic chars," Prog. Energy Combust. Sci., 35(2), pp. 121-140.

[90] Müller, R., von Zedtwitz, P., Wokaun, A., and Steinfeld, A., 2003, "Kinetic investigation on steam gasification of charcoal under direct high-flux irradiation," Chem. Eng. Sci., 58(22), pp. 5111-5119.

[91] Vyazovkin, S., 2015, Isoconversional Kinetics of Thermally Stimulated Processes, Springer International Publishing.

[92] Roberts, D. G., and Harris, D. J., 2006, "A Kinetic Analysis of Coal Char Gasification Reactions at High Pressures," Energy & Fuels, 20(6), pp. 2314-2320.

[93] Hüttinger, K. J., and Merdes, W. F., 1992, "The carbon-steam reaction at elevated pressure: Formations of product gases and hydrogen inhibitions," Carbon, 30(6), pp. 883-894.

[94] van Heek, K. H., Mühlen, H.-J., and Jüntgen, H., 1987, "Progress in the kinetics of coal and char gasification," Chem. Eng. Technol., 10(1), pp. 411-419.

[95] Mühlen, H.-J., van Heek, K. H., and Jüntgen, H., 1985, "Kinetic studies of steam gasification of char in the presence of H2, CO2 and CO," Fuel, 64(7), pp. 944-949.

[96] Blackwood, J., and Ingeme, A., 1960, "The Reaction of Carbon with Carbon Dioxide at High Pressure," Australian Journal of Chemistry, 13(2), pp. 194-209.

[97] Hurt, R. H., and Haynes, B. S., 2005, "On the origin of power-law kinetics in carbon oxidation," Proc. Combust. Inst., 30(2), pp. 2161-2168.

[98] Hecker, W. C., Madsen, P. M., Sherman, M. R., Allen, J. W., Sawaya, R. J., and Fletcher, T. H., 2003, "High-Pressure Intrinsic Oxidation Kinetics of Two Coal Chars," Energy Fuels, 17(2), pp. 427-432.

[99] Hong, J., Hecker, W. C., and Fletcher, T. H., 2000, "Modeling high-pressure char oxidation using langmuir kinetics with an effectiveness factor," Proc. Combust. Inst., 28(2), pp. 2215-2223.

[100] Murphy, J. J., and Shaddix, C. R., 2006, "Combustion kinetics of coal chars in oxygen-enriched environments," Combust. Flame, 144(4), pp. 710-729.

[101] Zhuang, Q., Kyotani, T., and Tomita, A., 1995, "Dynamics of Surface Oxygen Complexes during Carbon Gasification with Oxygen," Energy Fuels, 9(4), pp. 630-634.

[102] Hurt, R. H., and Calo, J. M., 2001, "Semi-global intrinsic kinetics for char combustion modeling," Combust. Flame, 125(3), pp. 1138-1149.

[103] Niksa, S., Liu, G.-s., and Hurt, R. H., 2003, "Coal conversion submodels for design applications at elevated pressures. Part I. devolatilization and char oxidation," Prog. Energy Combust. Sci., 29(5), pp. 425-477.

[104] Di Blasi, C., and Branca, C., 2001, "Kinetics of Primary Product Formation from Wood Pyrolysis," Ind. Eng. Chem. Res., 40(23), pp. 5547-5556.

[105] Mermoud, F., Golfier, F., Salvador, S., Van de Steene, L., and Dirion, J. L., 2006, "Experimental and numerical study of steam gasification of a single charcoal particle," Combust. Flame, 145(1–2), pp. 59-79.

[106] Yaman, S., 2004, "Pyrolysis of biomass to produce fuels and chemical feedstocks," Energy Convers. Manage, 45(5), pp. 651-671.

[107] Christian, D. G., Riche, A. B., and Yates, N. E., 2008, "Growth, yield and mineral content of Miscanthus × giganteus grown as a biofuel for 14 successive harvests," Ind. Crop. Prod., 28(3), pp. 320-327.

[108] Beale, C. V., and Long, S. P., 1997, "Seasonal dynamics of nutrient accumulation and partitioning in the perennial C4-grasses Miscanthus × giganteus and Spartina cynosuroides," Biomass Bioenergy, 12(6), pp. 419-428.

[109] Perlack, R. D., and Stokes, B. J., 2011, "U.S. Billion-Ton Update: Biomass Supply for a Bioenergy and Bioproducts Industry," U.S. Department of Energy. Oak Ridge National Laboratory.

[110] Lewandowski, I., Clifton-Brown, J. C., Scurlock, J. M. O., and Huisman, W., 2000, "Miscanthus: European experience with a novel energy crop," Biomass Bioenergy, 19(4), pp. 209-227.

[111] Chen, W., Thanapal, S. S., Annamalai, K., Ranjan, D., Lawrence, B., and Ansley, R. J., "Kinetics of Pyrolysis of Mesquite Fuel - Comparison of Different Methods," Proc. ASME Turbo Expo 2014: Turbine Technical Conference and Exposition, ASME.

[112] Eseltine, D., Thanapal, S. S., Annamalai, K., and Ranjan, D., 2013, "Torrefaction of woody biomass (Juniper and Mesquite) using inert and non-inert gases," Fuel, 113, pp. 379-388.

[113] Molina, A., and Mondragón, F., 1998, "Reactivity of coal gasification with steam and CO2," Fuel, 77(15), pp. 1831-1839.

[114] Matsumoto, K., Takeno, K., Ichinose, T., Ogi, T., and Nakanishi, M., 2009, "Gasification reaction kinetics on biomass char obtained as a by-product of gasification in an entrained-flow gasifier with steam and oxygen at 900–1000 °C," Fuel, 88(3), pp. 519-527.

[115] Yoon, H. C., Pozivil, P., and Steinfeld, A., 2012, "Thermogravimetric Pyrolysis and Gasification of Lignocellulosic Biomass and Kinetic Summative Law for Parallel Reactions with Cellulose, Xylan, and Lignin," Energy Fuels, 26, pp. 357-364.

[116] Trommer, D., 2006, "Thermodynamic and Kinetic Analyses of the Solar Thermal Gasification of Petroleum Coke," ETH Zurich.

[117] Butterman, H. C., and Castaldi, M. J., "CO2 enhanced steam gasification of biomass fuels," Proc. 16th Annual North American Waste-to-Energy Conference, American Society of Mechanical Engineers, pp. 157-172.

[118] Jayaraman, K., and Gokalp, I., 2015, "Effect of char generation method on steam, CO2 and blended mixture gasification of high ash Turkish coals," Fuel, 153, pp. 320-327.

[119] Otero, M., Gómez, X., García, A. I., and Morán, A., 2007, "Effects of sewage sludge blending on the coal combustion: A thermogravimetric assessment," Chemosphere, 69(11), pp. 1740-1750.

[120] Xiao, H.-m., Ma, X.-q., and Lai, Z.-y., 2009, "Isoconversional kinetic analysis of co-combustion of sewage sludge with straw and coal," Appl. Energy, 86(9), pp. 1741-1745.

[121] Alper, J. S., and Gelb, R. I., 1990, "Standard errors and confidence intervals in nonlinear regression: comparison of Monte Carlo and parametric statistics," J. Phys. Chem., 94(11), pp. 4747-4751.

[122] Press, W. H., Teukolsky, S. A., Vetterling, W. T., and Flannery, B. P., 1992, Numerical Recipes in C: The Art of Scientific Computing, Cambridge University Press.

[123] Spiess, A.-N., and Neumeyer, N., 2010, "An evaluation of R2 as an inadequate measure for nonlinear models in pharmacological and biochemical research: a Monte Carlo approach," BMC Pharmacology, 10(1), p. 6.

[124] Kannan, M., and Richards, G., 1990, "Gasification of biomass chars in carbon dioxide: dependence of gasification rate on the indigenous metal content," Fuel, 69(6), pp. 747-753.

[125] Mitsuoka, K., Hayashi, S., Amano, H., Kayahara, K., Sasaoaka, E., and Uddin, M. A., 2011, "Gasification of woody biomass char with CO2: The catalytic effects of K and Ca species on char gasification reactivity," Fuel Process. Technol., 92(1), pp. 26-31.

[126] Long, F. J., and Sykes, K. W., 1948, "The Mechanism of the Steam-Carbon Reaction," Proc. Roy. Soc. A, 193(1034), pp. 377-399.

[127] Matsui, I., Kunii, D., and Furusawa, T., 1987, "Study of char gasification by carbon dioxide. 1. Kinetic study by thermogravimetric analysis," Ind. Eng. Chem. Res., 26(1), pp. 91-95.

[128] Roberts, D. G., and Harris, D. J., 2000, "Char Gasification with O2, CO2, and H2O: Effects of Pressure on Intrinsic Reaction Kinetics," Energy Fuels, 14(2), pp. 483-489.

[129] Roberts, D. G., Hodge, E. M., Harris, D. J., and Stubington, J. F., 2010, "Kinetics of Char Gasification with CO2 under Regime II Conditions: Effects of Temperature, Reactant, and Total Pressure," Energy Fuels, 24(10), pp. 5300-5308.

[130] Karlström, O., Brink, A., and Hupa, M., 2015, "Desorption kinetics of CO in char oxidation and gasification in O2, CO2 and H2O," Combust. Flame, 162(3), pp. 788-796.

[131] Khawam, A., and Flanagan, D. R., 2006, "Solid-state kinetic models: basics and mathematical fundamentals," The journal of physical chemistry. B, 110(35), pp. 17315-17328.

[132] Gill, R., Bush, E., Haueter, P., and Loutzenhiser, P., 2015, "Characterization of a 6 kW high-flux solar simulator with an array of xenon arc lamps capable of concentrations of nearly 5000 suns," Review of Scientific Instruments, 86(12), p. 125107.

[133] Touloukian, Y. S., and DeWitt, D. P., 1972, Thermal radiative properties: nonmetallic solids, IFI/Plenum, New York.

[134] Neuer, G., 1995, "Spectral and total emissivity measurements of highly emitting materials," International Journal of Thermophysics, 16(1), pp. 257-265.

[135] Hathaway, B., 2013, "Solar Gasification of Biomass: Design and Characterization of a Molten Salt Gasification Reactor," PhD, University of Minnesota.

[136] Müller, F., Poživil, P., van Eyk, P. J., Villarrazo, A., Haueter, P., Wieckert, C., Nathan, G. J., and Steinfeld, A., 2017, "A pressurized high-flux solar reactor for the efficient thermochemical gasification of carbonaceous feedstock," Fuel, 193, pp. 432-443.

[137] von Zedtwitz, P., and Steinfeld, A., 2005, "Steam-Gasification of Coal in a Fluidized-Bed/Packed-Bed Reactor Exposed to Concentrated Thermal Radiation Modeling and Experimental Validation," Industrial & Engineering Chemistry Research, 44(11), pp. 3852-3861.

[138] Abe, T., Gokon, N., Izawa, T., and Kodama, T., 2015, "Internally-circulating Fluidized Bed Reactor Using Thermal Storage Material for Solar Coal Coke Gasification," Energy Procedia, 69, pp. 1722-1730.

[139] Puig-Arnavat, M., Tora, E. A., Bruno, J. C., and Coronas, A., 2013, "State of the art on reactor designs for solar gasification of carbonaceous feedstock," Solar Energy, 97, pp. 67-84.

[140] Saint-Gobain Ceramics, 2012, "Hexoloy SA Silicon Carbide - Technical Data," Technical Data Sheet, http://www.refractories.saint-gobain.com/sites/imdf.hpr.com/files/hexoloy-sa-sic-tds_0.pdf.

[141] Zircar Zirconia, Inc., 2012, "Alumina Boards and Cylinders - TYPE Buster," https://zircarzirconia.com/products/type-buster-alumina-boards-cylinders/.

[142] "Product Information - C3014," http://www.sigmaaldrich.com/content/dam/sigma-aldrich/docs/Sigma-Aldrich/Product_Information_Sheet/c3014pis.pdf.

[143] Channiwala, S. A., and Parikh, P. P., 2002, "A unified correlation for estimating HHV of solid, liquid and gaseous fuels," Fuel, 81(8), pp. 1051-1063.

[144] Eggleston, H. S., Buendia, L., Miwa, K., Ngara, T., and Tanabe, K., 2006, "Guidelines for National Greenhouse Gas Inventories," IPCC, Japan.

[145] Levenspiel, O., 1999, Chemical reaction engineering, Wiley.

[146] Ergun, S., 1952, "Fluid flow through packed columns," Chem. Eng. Prog., 48, pp. 89-94.

[147] Clements, M., and Haarhoff, J., 2004, "Practical experiences with granular activated carbon (GAC) at the Rietvlei Water Treatment Plant," Water SA, 30(1), pp. 89-96.

[148] Yang, W. C., 2003, Handbook of Fluidization and Fluid-Particle Systems, Taylor & Francis.

[149] Bich, E., Millat, J., and Vogel, E., 1990, "The viscosity and thermal conductivity of pure monatomic gases from their normal boiling point up to 5000 K in the limit of zero density and at 0.101325 MPa," Journal of Physical and Chemical Reference Data, 19(6), pp. 1289-1305.

[150] Broadhurst, T. E., and Becker, H. A., 1975, "Onset of fluidization and slugging in beds of uniform particles," Aiche J., 21(2), pp. 238-247.

[151] Kunii, D., and Levenspiel, O., 1991, Fluidization Engineering, Butterworth-Heinemann.

[152] 2014, "R: A Language and Environment for Statistical Computing," R Core Team, R Foundation for Statistical Computing, Vienna, Austria.

[153] Wu, C. F. J., and Hamada, M. S., 2011, Experiments: Planning, Analysis, and Optimization, Wiley.

[154] Vardeman, S. B., and Jobe, J. M., 2001, Basic Engineering Data Collection and Analysis, Brooks/Cole.